Department of Physics and Astronomy
University of Heidelberg

Master's Thesis in Physics
submitted by

Nick Lackmann

born in Heilbronn-Neckargartach (Germany)

2024

Velocity-Map Imaging with an XUV Frequency Comb

This Master's Thesis has been carried out by Nick Lackmann at the
Max Planck Institute for Nuclear Physics in Heidelberg
under the supervision of
apl. Prof. José R. Crespo López-Urrutia

Velocity-Map Imaging with an Extreme Ultraviolet Frequency Comb

Pushing precision spectroscopy towards shorter wavelengths not only reduces the quantum projection noise but also facilitates spectroscopy of highly charged ions or the thorium isomer ^{229m}Th, which are promising candidates for the search for new physics beyond the Standard Model. In pursuit of this objective, we present the first-ever velocity-map imaging (VMI) measurement using an extreme ultraviolet (XUV) frequency comb, measuring the angular momentum distribution of photoelectrons originating from the direct photoionization of neutral xenon. To that end, the reliability of the XUV frequency comb is improved to enable long-term operation, as demonstrated with a measurement run over five days, capable of producing harmonics with an energy of up to 42,eV. Furthermore, a dedicated VMI spectrometer is designed, numerically evaluated, and implemented into the existing XUV frequency comb beamline. An embedded Sikler lens is tested for novel operation modes to further improve the energy resolution or manipulate the photoelectron imaging process. Additionally, the experimental setup is conceptualized for a future cold atomic beam, which will facilitate the first spectroscopic measurements with our XUV frequency comb. For this purpose, we identify Rydberg states in argon and calculate their lifetimes numerically. The predicted energy resolution of 0.4 % enables the VMI spectrometer to experimentally separate photoelectrons originating from neighboring states.

Velocity-Map-Imaging mit einem extrem ultravioletten Frequenzkamm

Präzisionsspektroskopie bei kürzeren Wellenlängen reduziert nicht nur das Quantenprojektionsrauschen, sondern ermöglicht auch die Spektroskopie von hochgeladenen Ionen und dem Thorium-Isomer ^{229m}Th, die für die Suche nach neuer Physik besonders interessant sind. Zu diesem Ziel hin präsentieren wir die erste Velocity-Map-Imaging (VMI) Messung mit einem extrem-ultravioletten (XUV) Frequenzkamm, bei der die Drehimpulsverteilung von Photoelektronen gemessen wird, die von der direkten Photoionisation von neutralem Xenon stammen. Für diesen Zweck wird die Zuverlässigkeit des XUV-Frequenzkamms verbessert, um einen Langzeitbetrieb zu ermöglichen, was durch eine Messreihe über fünf Tage hinweg demonstriert wird, wobei Harmonische mit einer Energie von bis zu 42 eV erzeugt werden. Darüber hinaus wird ein spezielles VMI-Spektrometer entworfen, simuliert und in die bestehende XUV-Frequenzkamm Beamline integriert. Für die enthaltene Sikler-Linse werden Möglichkeiten untersucht, die Energieauflösung weiter zu verbessern oder die Photoelektronen-Abbildung zu manipulieren. Zudem ist der experimentelle Aufbau für einen kalten Atomstrahl konzipiert, der in Zukunft die ersten spektroskopischen Messungen mit unserem XUV-Frequenzkamm ermöglicht. Dafür werden Rydberg-Zustände in Argon identifiziert und die Lebensdauern numerisch berechnet. Experimentell wird die Trennung benachbarter Zustände durch die vorhergesagte Energieauflösung von 0.4 % des VMI-Spektrometers ermöglicht.

Contents

1. | Introduction

What time is it?

It was about 2.22 p.m. on November 23rd when the Large Hadron Collider recorded the first collision in all four detectors [1], testing of what has become an exceptionally successfully theory, the Standard model (SM) [2]. With the discovery of the Higgs boson in 2012 [3], all particles predicted by the SM have been detected, generating the impression that all is discovered. However, despite its success, the SM exists in a peculiar state where it is known to be incomplete. It only accounts for three of the four fundamental forces, failling to integrate gravity with the other interactions [4]. Additionally, it explains only $\sim$16 % of observed matter, leaving the dark sector unexplained [5], and it does not provide an explanation for the observed matter-antimatter asymmetry [6].

This raises the question of what lies beyond the Standard Model (BTSM). Insights may be gained looking at the time, exploring time and frequency measurements, which offer unparalleled precision. State-of-the-art atomic clocks now achieve a fractional uncertainty of 8×10^{-19} [7]. At this level of precision, the frequency measurements become sensitive to small perturbations, such as potential couplings of dark matter to atoms or possible variations of fundamental constants [2]. Combined with rapid advancements in the field of atomic, molecular and optical physics, the search of new physics using low-energy experiments holds significant promise.

The search of physics BTSM motivates this thesis, which aims to advance the precision frontier by establishing spectroscopy at higher frequencies in the extreme ultraviolet (XUV) region of the spectrum. This advancement enables the spectroscopy of highly charged ions (HCI), where the transitions shift towards higher energies and exhibit unique characteristics. The intricacies of going to higher frequencies as well as the implications for the search of new physics is discussed in the following sections.

1.1. Precision Physics in the Extreme Ultraviolet

Recent advancements in generating and controlling ultra-short laser pulses have significantly impacted not only metrology but also time-resolved spectroscopy [8], as evident by the recent bestowment of the 2023 Nobel price in this field [9]. Notably, the development of the frequency comb has greatly enhanced precision, enabling the absolute measurement of optical frequencies and advancing frequency measurements from the microwave to the optical regime [10, 11]. This technique can be extended into the XUV regime generating an XUV frequency comb through high harmonic generation (HHG) [12, 13, 14]. HHG, a technique prevalent in attosecond physics, generates short, phase-coherent pulses in the XUV regime in response to intense laser pulses [8, 15, 16, 17].

The benefit of transferring the comb to the XUV becomes evident when considering the quantum projection noise [18, 19] which for the interrogation of N uncorrelated two level systems in a Ramsey scheme with a free evolution time T is given by

$$\sigma_{\mathrm{y}}(\tau) = \frac{1}{2\pi\nu_0\sqrt{NT\tau}} \,. \tag{1.1}$$

This Allan deviation σ_{y} arises from the impossibility to measure conjugate physical observables. To decrease the noise, the interrogation or averaging time τ can be prolonged by reducing decoherence effects or using novel interrogation schemes like quantum nondemolition measurements [20]. Another approach is to increase the number of interrogated atoms, as seen in strontium lattice clocks, or even entangle the atoms to change the dependence from $N^{-1/2} \mapsto N^{-1}$ as for a set of fully entangled atoms [19]. Finally, noise can be reduced by using transitions with higher frequencies, which is why optical clocks have surpassed the microwave caesium clocks in recent years.

Taking this a step further into the XUV regime not only reduces the projection noise but also allows for the interrogation of HCIs. A significant advantage of HCIs is their insensitivity to external perturbation, allowing unprecedented precision due to suppressed systematic shifts [21, 22]. As the energy scales approximately with the atomic number Z^2 for hydrogen like atoms, the transitions shift to shorter wavelengths, which are typically inaccessible for laser spectroscopy. However, due to Coulomb degeneracy and configuration crossings, there are ions with transitions accessible by lasers, with many in the XUV [23, 24].

To drive transitions in HCIs, a coherent short-wavelength light source is required. One option for obtaining radiation in these regimes are free-electron lasers and synchrotrons. Both approaches require significant experimental efforts and lack coherence [25, 26]. An alternative approach is the up-conversion of light using low-order nonlinear processes such as second-harmonic generation, third-harmonic generation and four-wave-mixing. For even higher energies, HHG can be utilized. When generating high harmonics, the response of a target to a high intensity laser field is exploited to produce odd integer harmonics of the driving laser field [15]. This technique can generate photons all the way into the soft x-ray regime [27, 28, 29]. Using a frequency comb as the driving laser also imparts a comb structure to the individual harmonics, effectively generating an XUV frequency comb [14, 13]. The advantage of this technique is that it utilizes established optical systems and elements to generate the driving laser field, typically in the near-infrared (NIR) to visible regime. The resulting XUV comb has a sufficient coherence time ($> 1\,\mathrm{s}$) [30], and enables direct frequency spectroscopy in the XUV regime [12].

1.2. Physics Beyond the Standard Model with HCI

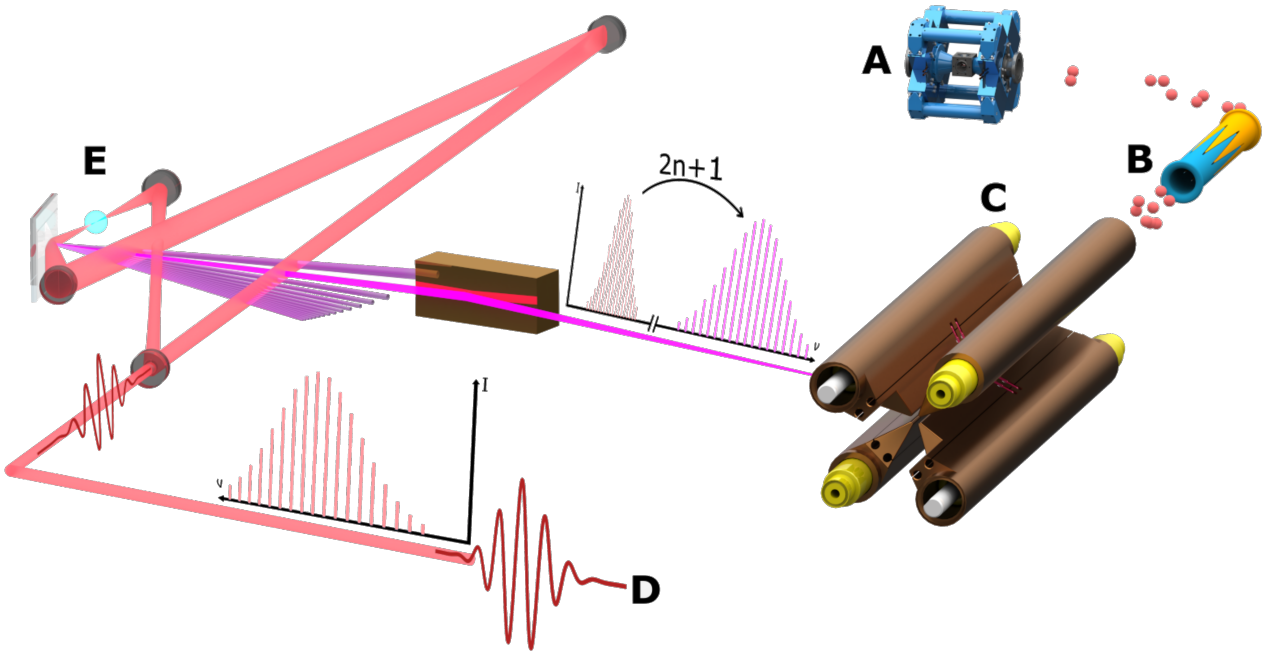

Figure 1.1.: Schematic overview of the experimental setup for spectroscopy of HCI. The HCI are produced in an EBIT **A**, afterwards they are decelerated and bunched in a pulsed drift tube **B**. They are trapped in the CryPTEx SC Paul trap **C**. A NIR frequency comb **D** is coupled into a passive enhancement cavity **E** where the frequency comb is transferred into the XUV. Subsequently the XUV frequency comb can be used for spectroscopy applications.

The experimental implementation enabling the spectroscopy of HCIs is part of the cryogenic Paul trap experiment super conducting (CryPTEx SC) at the Max Planck Institute for Nuclear Physics in Heidelberg, as shown in Figure 1.1. It consists of a compact electron beam ion trap (EBIT) producing HCIs, which are then selected by their charge-to-mass ratio and transported by a dedicated beamline. The ions are subsequently trapped in the cryogenic CryPTEx SC Paul trap. Inside the Paul trap, a Coloumb crystal of laser-cooled Be^+ ions, sympathetically cools the HCIs until they crystallize and become trapped. By reducing the Be^+ and the HCI population until only one of each remains, the ensemble can be used for quantum logic spectroscopy [31]. In order to drive the transitions, an XUV frequency comb is needed which is driven by a high-repetition NIR frequency comb. The XUV frequency comb, constructed as part of dissertations by J. Nauta and J.H. Oelmann [32, 33], has a repetition rate of 100 MHz with a central wavelength of 1039 nm. It is amplified and sent to a passive enhancement cavity, where subsequent pulses are overlapped resonantly to achieve the necessary intensities of $10^{14}\,\mathrm{W/cm^2}$ to produce the harmonics in a gas jet. A grating mirror couples the harmonics out of the enhancement cavity, spatially separating the individual harmonics for studies of new physics.

1.2.1. Variation of Fundamental Constants

In many theories BTSM fundamental constants become dynamical and vary with time. These constants are experimentally determined parameters that cannot be predicted by the theories in which they appear [34]. To mitigate the choice of measurement units, the discussion is reduced to dimensionless quantities [2], such as the proton-to-electron mass ratio $\mu = m_\mathrm{p}/m_\mathrm{e}$, the strong interaction parameter χ_q and the fine structure constant α. Given that atomic transitions dependent on these fundamental constants, atomic clocks are sensitive to such a possible variation. The tick rate of the clock may dependent on the location, time and type of clock, since the transition of different clocks depend differently on these constants [35]. By comparing such two transitions that depend differently on the fundamental constants, it is possible to investigate variations by parameterizing the transitions in terms of the these constants and examining the frequency ratio R [36]

$$\frac{1}{R}\frac{dR}{dt} = (K_1 - K_2 - 2)\frac{1}{\alpha}\frac{d\alpha}{dt} + \frac{1}{\mu}\frac{d\mu}{dt} - \kappa\frac{1}{\chi_\mathrm{q}}\frac{d\chi_\mathrm{q}}{dt} \,. \tag{1.2}$$

The sensitivity factors K_i and κ for each transition can be obtained from atomic structure calculations. To detect such variations, the difference in sensitivity parameters must be maximized. Transitions in HCIs enhance sensitivity, as the parameter scales quadratically with the charge state Q [21, 23]

$$K \propto 2\alpha^2 Z^2 (q+1)^2 \,. \tag{1.3}$$

Hence, there is an ongoing effort to probe such variations with high precision by utilizing HCIs like Cf^{16+}, improving the sensitivity of the current limits by a factor of ∼23. These current limits come from comparisons of different combinations of optical and microwave clocks where the limit for the fractional variation of α and μ are given by [37, 36]

$$\begin{aligned} \frac{\dot{\alpha}}{\alpha} &= (-2.0 \pm 2.0) \times 10^{-17}\frac{1}{yr} \\ \frac{\dot{\mu}}{\mu} &= (0.2 \pm 1.1) \times 10^{-16}\frac{1}{yr} \,. \end{aligned} \tag{1.4}$$

Furthermore, the low-energy thorium-229 isomer, now measured at 148.3821(5) nm [38], is a promising candidate with an enhanced sensitivity for a variation in α of three orders of magnitude when compared to Cf^{16+} [39]. The transition energy is accessible in the context of advancing precision spectroscopy to shorter wavelengths [39].

1.2.2. Fifth Force Searches

The precision of atomic clocks can be utilized to probe the dark sector through a minuscule non-gravitation coupling to the SM. This coupling would lead to shifts in energy levels, where the inducing field can be of transient, drifting or oscillating nature, depending on the dark matter candidate [40, 41, 42]. While an oscillating (pseudo)scalar dark matter field can induce evolution of fundamental constants, which can be investigated as previously mentioned, a potential fifth force has also been proposed as an addition to the SM [43]. This fifth force, along with conjectured new bosons with spin-independent couplings to electrons and neutrons, can be investigated using isotope shift-spectroscopy [44]. In this method, two or more transitions are compared for different isotopes, employing the generalized King-Plot method to search for non-linearities arising from new physics [44, 45]. Highly charged ions allow for many more

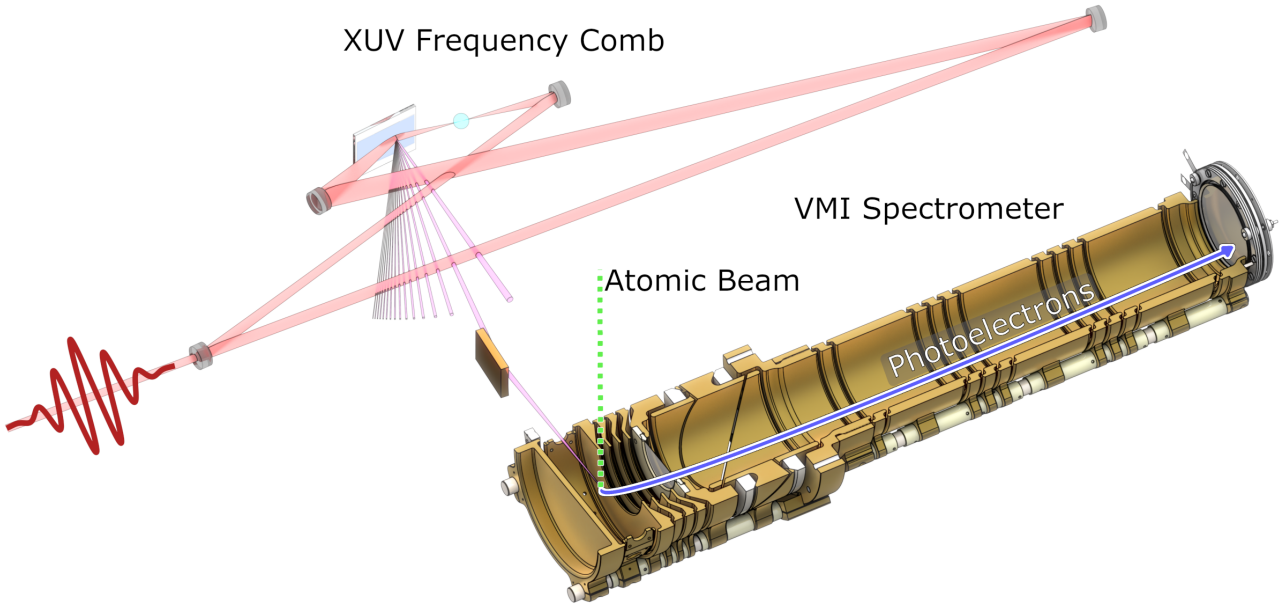

Figure 1.2.: Schematics of the VMI spectrometer setup, where the XUV frequency comb is used to do spectroscopy on an atomic beam. The excited atoms get ionized and the photoelectrons imaged onto a position sensitive detector.

transitions to be probed while benefiting from reduced systematic errors arising from external perturbations. Recently, transitions in highly charged calcium have been measured that can be used for the search for new physics by isotope shift spectroscopy [46].

1.3. Velocity-Map Imaging with an XUV Frequency Comb

To establish the XUV frequency comb as a robust tool for spectroscopy on individual HCIs, the system must be made reliable and tools have to be developed. Given the inefficient detection and low yield of XUV photons from a single ion, techniques from the attosecond community are utilized to measure and improve upon the XUV frequency comb. Figure 1.2 shows the schematics of this endeavor, where a neutral gas target, such as a cold atomic beam, enables the simultaneous interrogation of 10^5 to 10^6 atoms. Additionally, a velocity-map imaging (VMI) spectrometer allows for full 4π solid-angle detection of photoelectrons [47]. A VMI spectrometer images the transversal momentum of charged particles onto a position-sensitive detector using an electrostatic lens. This not only resolves the energy and momentum of the photoelectrons but also provides access to the temporal profile and phase of the XUV light through techniques such as attosecond streaking [48]. Measuring a photoelectron signal does circumnavigate the usually low numerical aperture of fluorescence detection setups. It also allows to use a second color laser to drive the ionization. Such a 1+1' scheme allows the use of a NIR laser for ionization, where commercially available lasers with sufficient power are available. The energy resolution of the spectrometer can then discriminate between closely spaced states that are excited simultaneously. This not only improves the detection efficiency of previous direct XUV frequency comb measurements [12] but also enables to interrogate more transitions in a single measurement run than previously observed. Ultimately, the setup allows to conduct isotope shift measurements to search for non-linearities in a cold atomic beam [49].

1.4. Thesis Outline

Advancing precision spectroscopy into the XUV regime offers significant potential. This thesis explores the initial steps towards implementing VMI measurements with an XUV frequency comb. In Chapter 2, we provide the theoretical background for generating an XUV frequency comb, introducing ultrashort laser pulses and the HHG process. Following this, we investigate the relevant light-matter interaction using a two-level system. Chapter 3 presents a brief overview of the experimental setup for generating the XUV frequency comb, including the improvements made for reliable operation. Finally, Chapter 4 introduces the VMI spectrometer, detailing the design considerations and evaluating its performance numerically. Finally, Chapter 5 describes the first VMI measurement with an XUV frequency comb and discusses the path towards the precision measurement of argon Rydberg states.

2. | Theoretical Foundations

With the advent of the laser in 1960, the science of metrology was revolutionized, allowing precise interrogation and control of quantum systems. The optical purity, coherence and optical power densities provided by lasers are orders of magnitudes higher compared to conventional radiation sources. Utilizing these high intensities to drive the response of materials into the nonlinear regime can produce harmonic components of the driving field. This can be used to interrogate atoms and molecules by exciting transitions between quantum levels, ionizing atoms and dissociating molecules.

First, we will discuss the light field of ultrashort laser pulses to understand the characteristics of frequency combs. Afterwards, we show how we transfer the comb into the XUV by the HHG process. Second, the interaction of atoms with the generated light field will be discussed.

2.1. Nonlinear Optics

This section covers the theoretical fundamentals of nonlinear optics, building upon previous work summarized in [50]. It begins with an introduction to Gaussian pulses and beams based on the work of J. Diels and W. Rudolph [51]. Subsequently, it discusses two key principles essential for understanding the XUV frequency comb: frequency comb generation and the HHG process.

2.1.1. Gaussian Beam Propagation

The behavior of electromagnetic waves is governed by Maxwell's equations, with the material response defined by a macroscopic polarization $\mathbf{P}$. The electromagnetic radiation is described by the time and space dependent complex valued electric field $\mathbf{E}$ and magnetic field $\mathbf{B}$. The

wave equation for the electric field can be derived directly from Maxwell's equations

$$\left(\Delta - \frac{1}{c^2}\frac{\partial^2}{\partial t^2}\right)\mathbf{E} = \mu_0\,\partial_t^2\,\mathbf{P}\,, \tag{2.1}$$

where μ_0 is the magnetic permeability of free space. For simplification, we set the polarization to be zero, which implies the absence of a medium, and consider a plane wave. With the electric field linearly polarized along the z-axis, Equation 2.1 simplifies to

$$\left(\frac{\partial^2}{\partial z^2} - \frac{1}{c^2}\frac{\partial^2}{\partial t^2}\right)E = 0\,. \tag{2.2}$$

The general solution for a plane wave is given by

$$E\,(\omega, z) = E\,(\omega, 0)\;e^{-ik(\omega)z}, \tag{2.3}$$

for a wave oscillating with angular frequency ω and wave number $k(\omega)$, which is governed by the linear dispersion relation

$$k^2\,(\omega) = \omega^2\epsilon(\omega)\mu_0 = \frac{\omega^2}{c^2}n^2(\omega)\,, \tag{2.4}$$

with the speed of light c, dielectric constant $\epsilon(\omega)$ and the refractive index $n\,(\omega)$.

The wave number can be expanded about the carrier frequency ω_c, so that $k(\omega) = k(\omega_\mathrm{c}) + \delta k$. Hence, Equation 2.3 can be rewritten as

$$E(\omega, z) = E(\omega + \omega_\mathrm{c}, 0)e^{-ik_\mathrm{c}z}e^{-i\delta k\,z}\,, \tag{2.5}$$

with $k_\mathrm{c} \equiv k(\omega_\mathrm{c})$. A useful way to describe pulses is to separate the wave into a carrier frequency and an envelope function. This can be justified as long as the spectral bandwidth is only a small part of the carrier frequency $\Delta\omega/\omega_\mathrm{c} \ll 1$, which means that the pulse envelope and the phase variation is small within an optical cycle [51]. Correspondingly, we can introduce an amplitude $\mathcal{E}$ which is slowly varying in the spatial coordinate

$$\mathcal{E}(\omega, t) = E(\omega + \omega_\mathrm{c}, 0)\,e^{-i\delta k\,z}\,. \tag{2.6}$$

For this approximation to be valid, the wave number spectrum must be sufficiently small $|\Delta k/k_\mathrm{c}| \ll 1$. In other words, the pulse envelope should not change significantly while traveling a distance comparable with the wavelength. Fourier transforming Equation 2.5 results in the following expression in the time domain

$$\begin{aligned} E(t, z) &= \frac{1}{2}\left\{\frac{1}{\pi}\int_{-\infty}^{\infty} d\omega\; E(\omega, 0)\,e^{-i\delta k\,z}\,e^{i(\omega-\omega_\mathrm{c})t}\right\}\,e^{i(\omega_\mathrm{c}t - k_\mathrm{c}z)} \\ &= \frac{1}{2}\mathcal{E}(t, z)\,e^{i(\omega_\mathrm{c}t - k_\mathrm{c}z)}. \end{aligned} \tag{2.7}$$

The amplitude function $\mathcal{E}$ describes the envelope in either the time or the frequency domain, linked by the Fourier transform. Common envelopes are described by a sech^2, Lorentzian or Gaussian. Assuming a Gaussian distribution centered around $z = 0$, the temporal profile is given by

$$\mathcal{E}(t, 0)\;\; = \mathcal{E}_0\,e^{-2\ln 2\left(\frac{t}{\tau_\mathrm{p}}\right)^2}\,. \tag{2.8}$$

Thus, τ_P describes the full width at half maximum (FWHM) of the intensity profile $|E(t)|^2$ in the time domain whereas $\Delta\omega_\mathrm{p} = \frac{4ln2}{\tau_\mathrm{p}}$ is the FWHM of the intensity distribution in the frequency domain. Since they are linked through the Fourier transform, the minimal time-bandwidth product can be defined:

$$\tau_\mathrm{P}\,\Delta\nu_\mathrm{P} = \frac{\tau_\mathrm{P}\,\Delta\omega_\mathrm{P}}{2\pi} = \frac{2\,ln2}{\pi} \approx 0.4413\,. \tag{2.9}$$

The factor 0.4413 is characteristic for Gaussian pulses and takes up different values for different pulse shapes. The product gives the temporal limit for a given spectral bandwidth. This limit is only valid if the pulse possesses no chirp, otherwise the value increases.

Up until now, the description is made under the plane wave approximation. As the spatial profile of lasers can not be described by an infinitely large wavefront, we reconsider the approximation. As long as changes in the spatial profile and pulse envelope occur independently or the process does not influence the spatial profile, the simplification is justified, because changes in pulse characteristics can be separated from changes in the spatial beam profile. Thus, an arbitrary transverse beam profile can be taken into account, described by a complex scalar function $u\,(x, y, z)$. The electric field now reads

$$E\,(x, y, z, t) = \frac{1}{2}u(x, y, z)\mathcal{E}(t, z)\,e^{i(\omega t - k_\mathrm{c} z)} + c.c.\,. \tag{2.10}$$

This expression can be plugged back into Equation 2.1. Assuming that the z-dependence of $u(x, y, z)$ varies slowly compared to the transverse components allows the separation of the time dependent part. Working within the paraxial approximation [52] yields

$$\left(\frac{\partial^2}{\partial x^2} + \frac{\partial^2}{\partial y^2} - 2ik_\mathrm{c}\frac{\partial}{\partial z}\right) u(x, y, z) = 0\,. \tag{2.11}$$

The paraxial approximation decribes waves where the transverse beam dimensions remaining sufficiently small as compared to the travel distance. An important solution of Equation 2.1 is the Gaussian beam

$$u(x, y, z) = \frac{u_0}{\sqrt{1 + z^2/z_\mathrm{R}^2}} e^{-i\Theta(z)}\, e^{-ik_\mathrm{c}(x^2+y^2)/2R(z)}\, e^{-(x^2+y^2)/w^2(z)}. \tag{2.12}$$

With following parameters, as illustrated in Figure 2.1:

$$R(z) = z + \frac{z_\mathrm{R}^2}{z} \tag{2.13}$$

$$w(z) = w_0\sqrt{1 + \frac{z^2}{z_\mathrm{R}^2}} \tag{2.14}$$

$$\Theta(z) = \arctan\left(\frac{z}{z_\mathrm{R}}\right) \tag{2.15}$$

$$z_\mathrm{R} = \frac{n\,\pi\,w_0^2}{\lambda} \tag{2.16}$$

$$\theta_0 = \Theta(z)\Big|_{\mathrm{z}\to\infty} = \frac{\lambda}{n\,\pi\,w_0}\,. \tag{2.17}$$

The Gaussian beam traveling in z-direction has a beam radius of $w(z)$ where the beam waist w_0 is centered around $z = 0$, so that $w_0 = w(z = 0)$. $R(z)$ denotes the radius of curvature of the

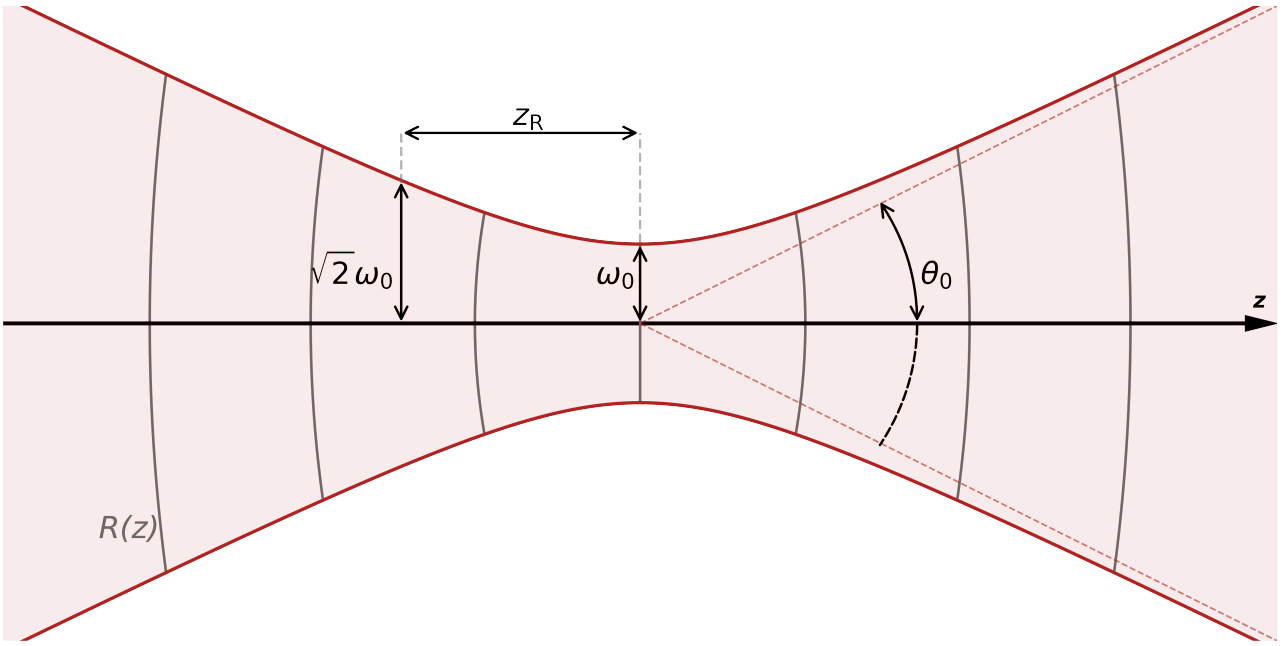

Figure 2.1.: Profile of a Gaussian beam with focus waist ω_0, Rayleigh length z_R and divergence θ_0. Over the plane with a radius of curvature $R(z)$ the phase is constant. Taken from [50]

planes of constant phase. Finally, z_R is the so-called Rayleigh length and θ_0 the divergence. A Gaussian beam is fully defined by a given amplitude u_0, the beam waist w_0 and the wavelength $\lambda = 2\pi/k_c$. For convenience, Equation 2.12 can be rewritten in terms of the complex beam parameter $q(z)$ defined by

$$\frac{1}{q(z)} = \frac{1}{R(z)} - \frac{i\,\lambda}{\pi w^2(z)} = \frac{1}{q(0)+z}\,, \tag{2.18}$$

as

$$u(x,y,z) = \frac{u_0}{\sqrt{1+z^2/z_R^2}} e^{-i\Theta(z)}\, e^{-ik_1(x^2+y^2)/2q(z)}\,. \tag{2.19}$$

Parameterizing the beam using the complex beam parameter makes it convenient to propagate the beam through free space and optical components since the ABCD matrix formalism can be used [52]. Let A, B, C and D be the elements of a 2×2 matrix, called the ray transfer matrix M

$$M = \begin{pmatrix} A & B \\ C & D \end{pmatrix}. \tag{2.20}$$

The complex beam parameter after the object of interest q_2 will evolve from an incident beam q_1 according to

$$q_2 = \frac{A\,q_1 + B}{C\,q_1 + D}. \tag{2.21}$$

This can be done successively to propagate a beam through an arbitrary optical system. Hence, the system can be described by a single total ray transfer matrix M_{tot}

$$M_{tot} = M_n\, M_{n-1} \ldots M_2\, M_1\,. \tag{2.22}$$

Optical Elements	ABCD Matrix
Free space with refractive index n_0	$\begin{pmatrix} 1 & z/n_0 \\ 0 & 1 \end{pmatrix}$
Thin lens	$\begin{pmatrix} 1 & 0 \\ -1/f & 1 \end{pmatrix}$
Curved mirror, tangential plane	$\begin{pmatrix} 1 & 0 \\ -2/R\cos(\Theta) & 1 \end{pmatrix}$
Curved mirror, sagittal plane	$\begin{pmatrix} 1 & 0 \\ -2\cos(\Theta)/R & 1 \end{pmatrix}$

Table 2.1.: ABCD matrices of common optical elements. Here, f is the focal length, which is positive for converging lenses. The focal length of curved optics with radius R is depended on the angle of incidence Θ.

The ray matrices for common optical elements are shown in Table 2.1. In the case of a single thin lens with focal length f, the lens formula for Gaussian beams can be extracted for an object distance u and a focal distance of v [53] given by

$$\frac{1}{u + z_{\mathrm{R}}^2/(u-f)} + \frac{1}{v} = \frac{1}{f}. \tag{2.23}$$

The resulting magnification M is given by

$$M = \frac{w_0'}{w_0} = \frac{1}{\sqrt{\left(1 - (u/f)\right)^2 + \left(z_{\mathrm{R}}/f\right)^2}} \tag{2.24}$$

The magnification can be used to convert the beam parameters from the incoming beam to the focused beam, simplifying the matrix calculations from Equation 2.22.

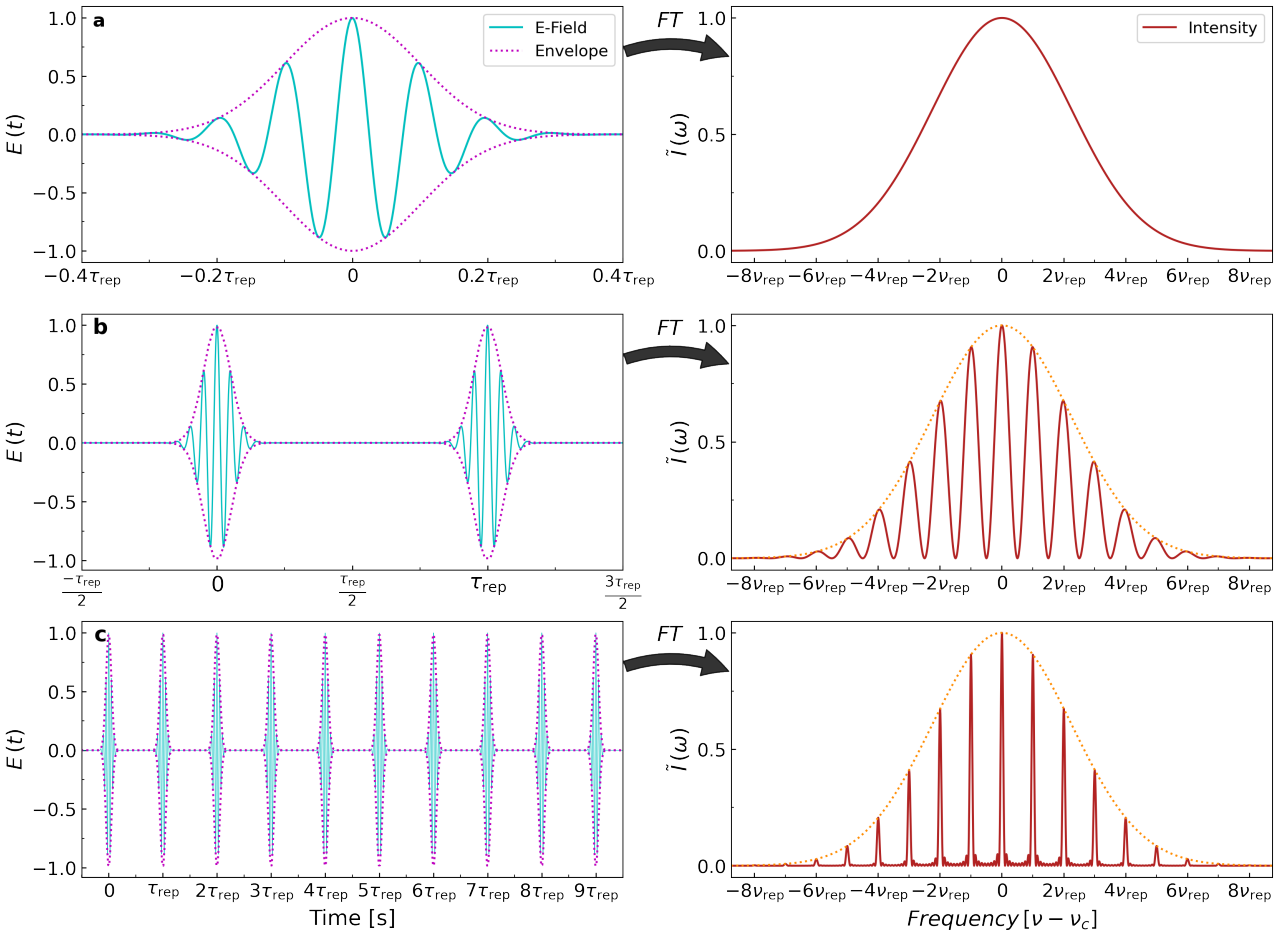

Figure 2.2.: Signals in the time domain and their Fourier transform are shown for a train of $N = 1, 2, 10$ equally delayed pulses in Figure a, b and c, respectively. Taken from [50].

2.1.2. Gaussian Pulse Train

Using the superposition principle, the electric field for a trian of N pulses, spaced τ_{rep} apart can be described by their sum [54]

$$E_N(t) = \sum_{n=0}^{N} \mathcal{E}(t - n\tau_{\mathrm{rep}}) e^{i(\omega_c t - n\omega_c \tau_{\mathrm{rep}} + n\Delta\phi_{\mathrm{CEO}} + \phi_0)} , \tag{2.25}$$

with the Fourier transformation given by

$$E_N(\omega) = e^{i\phi_0} \mathcal{E}(\omega - \omega_c) \sum_{n=0}^{N} e^{i(n\Delta\phi_{\mathrm{CEO}} - n\omega\tau_{\mathrm{rep}})} . \tag{2.26}$$

The carrier-to-envelope offset phase $\phi_{CEO} = n\Delta\phi_{\mathrm{CEO}} + \phi_0$ describes the phase difference of the envelope and the underlying carrier from pulse to pulse starting from ϕ_0. When the maxima of the envelope and the carrier coincide, the phase equals zero. Using trigonometric relations, the intensity given by Equation 2.26 can be simplified to

$$I_N(\omega) = |E_N(\omega)|^2 = I_0(\omega) \frac{\sin^2\left(\frac{N(\omega\tau_{\mathrm{rep}} + \Delta\phi_{\mathrm{CEO}})}{2}\right)}{\sin^2\left(\frac{\omega\tau_{\mathrm{rep}} + \Delta\phi_{\mathrm{CEO}}}{2}\right)} . \tag{2.27}$$

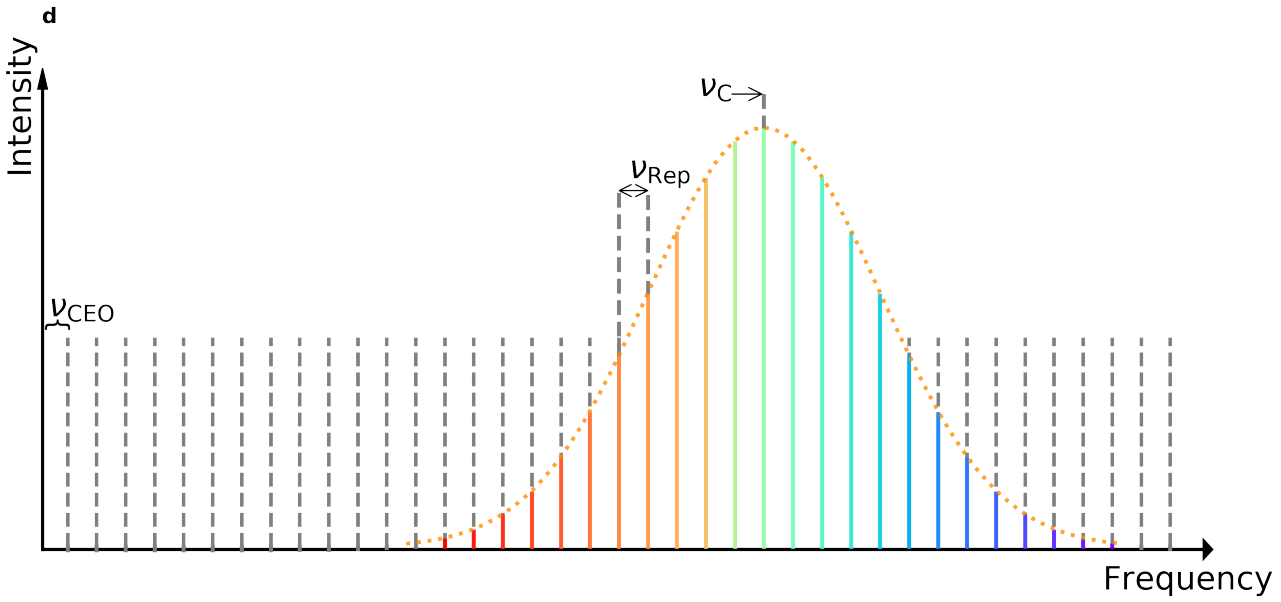

Figure 2.3.: The spectrum of a frequency comb is depicted with the carrier-to-envelope offset frequency ν_{CEO}, the carrier frequency ν_{c} and the repetition frequency ν_{Rep} being marked. Taken from [50].

Hence, the intensity spectrum of N pulses is described by the spectrum of a single pulse modulated by a periodic function. This is illustrated in Figure 2.2, where the Fourier transformation for a single, double and a decouple pulse signal is shown. The intensity becomes modulated with peaks spaced $\nu_{rep} = 1/\tau_{\mathrm{rep}}$ apart, where the width depends on the number of pulses taken into account.

As the spectral peaks become narrower with increasing number of pulses, the behavior in the limit $N \to \infty$ is of interest. In this limit, Equation 2.26 can be rewritten, using the Poisson sum formula, to

$$E_{\mathrm{N}}(\omega) = e^{i\phi_0}\, \mathcal{E}(\omega - \omega_{\mathrm{c}}) \sum_{n=0}^{\infty} \delta\left(\omega\tau_{\mathrm{rep}} + \Delta\phi_{\mathrm{CEO}} - n2\pi\right) \ , \tag{2.28}$$

where the signal now consists of infinitely sharp peaks under the envelope resulting in a comb like structure, hence the name frequency comb, with well-defined frequencies arising from a train of pulses with a fixed phase relation.

2.1.3. Frequency Combs

When generating a frequency comb by the means of stabilizing the pulse train from a mode-locked laser, the process relies on the periodic signal. As seen in Equation 2.28, the electric field is only non-zero when $\omega\tau_{\mathrm{rep}} + \Delta\phi_{CEO} = n\,2\pi$, with n being an integer. The comb-like structure can be quantified by the following two formulae, using the carrier-envelope-offset ν_{CEO} which describes the frequency with which ϕ_{CEO} changes by 2π;

$$\nu_{\mathrm{rep}} = \frac{1}{\tau_{\mathrm{rep}}} \, , \tag{2.29}$$

$$\nu_{\mathrm{CEO}} = \frac{\Delta\phi_{\mathrm{CEO}}}{2\pi\,\tau_{\mathrm{rep}}} \, . \tag{2.30}$$

Taking both of these expressions into account, the formula for the frequency comb denoting the n^{th} frequency tooth can be written as [55]

$$\nu_n = n\,\nu_{\text{rep}} + \nu_{\text{CEO}} \quad , n \in \mathbb{N}\,. \tag{2.31}$$

This summarizes the fact that the spectrum consisting of equally spaced sharp peaks ν_{rep} apart, which are offset by ν_{CEO}, as depicted in Figure 2.3. As the spectrum is independent of an optical reference frequency, knowing the repetition rate and the carrier-to-envelope offset makes it possible to measure optical frequencies absolutely.

Under real world circumstances, the width of the peaks is determined by the stability of ν_{rep} and ν_{CEO}. To resolve the repetition rate, a fast photodiode can be used, which feeds back into the system through locking electronics. Contrary, the offset frequency is not easily detectable and a self referencing method was developed [56, 57] in which an octave spanning spectrum is produced by spectral broadening in a nonlinear fiber. Frequency doubling the original comb ($2\nu_n$) and mixing it with the broadened spectrum (ν_{2n}) leads to a beat-signal from which the carrier-offset frequency can be determined by $2\nu_n - \nu_{2n} = \nu_{\text{CEO}}$ and stabilized.

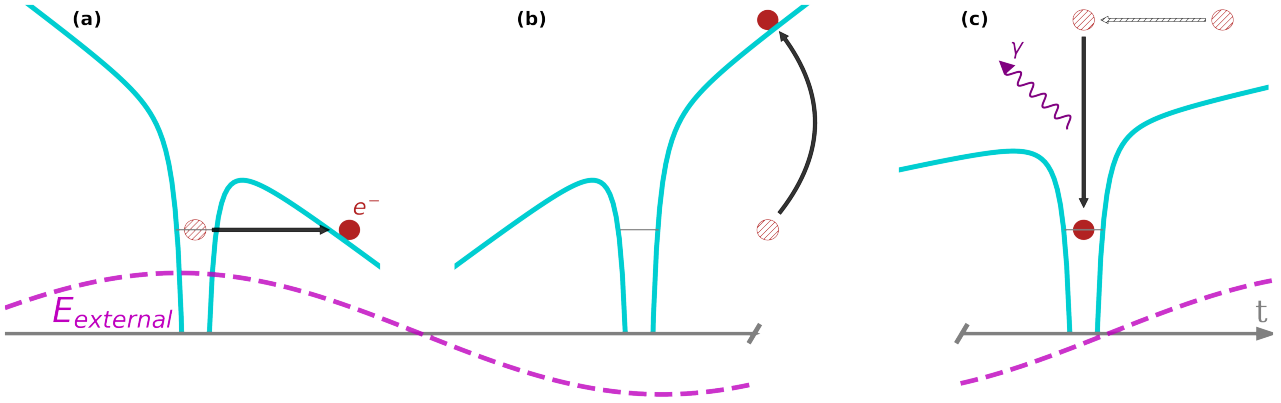

Figure 2.4.: A representation of the three step model where (a) the electron tunnels through a suppressed atomic potential (b) propagates in the external E-field while gaining kinetic energy and (c) releasing it by the emission of a high-energy photon when recombining. The process is shown in accordance to the driving laser E-field $E_{external}$. Taken from [50].

2.1.4. High Harmonic Generation

The up-conversion of light through HHG is a highly nonlinear process which was discovered in 1987 [15]. A semi-classical depiction of the HHG process is given with the three step model (TSM) discussed in Subsection 2.1.4.1, which provides an intuitive picture of the process. Subsequently, a quantum-mechanically depiction is given with the Lewenstein model in Section 2.1.4.2.

2.1.4.1. Three Step Model

The Three Step Model is a semi-classical description of HHG published by Corkum *et al.* in 1993 [16].The semi-classical description of the HHG process is illustrated in Figure 2.4. It divides the mechanism into the following three steps:

Step 1
A laser with sufficient intensity alters the Coulomb field of atoms such, that the probability of an electron tunneling through it becomes significant. Depending on the intensity of the laser, different regimes can be identified besides this tunneling regime. An important parameter in that regard, is the Keldysh parameter [58], defined as

$$\gamma = \sqrt{\frac{U_{\text{ion}}}{2\,U_{\text{pond}}}}, \tag{2.32}$$

where U_{ion} is the ionization energy and U_{pond} is the so-called ponderomotive energy. For $\gamma \gg 1$, multiphoton ionization is the dominant process. If $\gamma \approx 1$, the electric field is strong enough, such that tunneling starts to get the dominant process. This tunneling regime is of interest when generating high harmonics. With $\gamma \ll 1$, the intensities are strong enough to suppress the atomic potential such that the electron is not bound by it anymore. This regime is dubbed over-the-barrier ionization.

Step 2

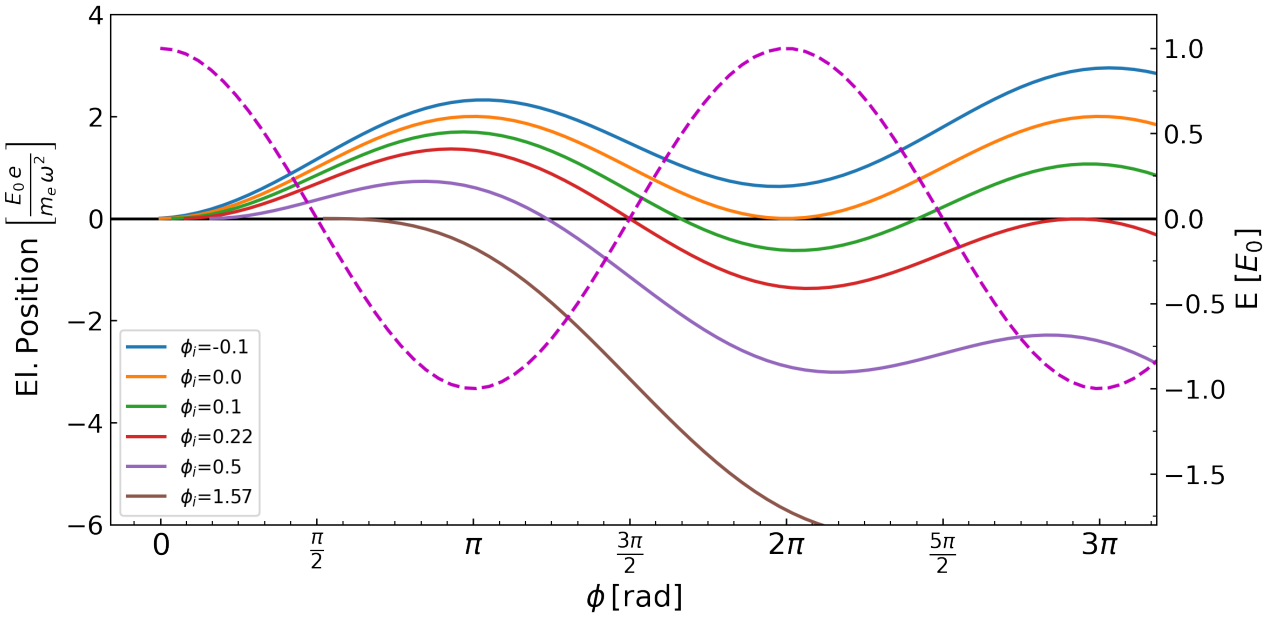

Figure 2.5.: The different trajectories the electron can take depending on the time of ionization and the according phase ϕ_i of the driving electric field shown as a dashed line. Taken from [50].

The freed electron propagates in the strong electric field after tunneling with negligible influence of the parent ion. Hence, the time-averaged energy of an electron oscillating in an oscillating electric field is given by the before mentioned ponderomotive energy

$$U_\mathrm{pond} = \frac{e^2 E_0^2}{2\, m_\mathrm{e}\, \omega_\mathrm{c}^2}. \tag{2.33}$$

Step 3
As the electric field changes sign, the electron can be driven back to the parent ion where it can recombine. During recombination, a high energy photon gets emitted with an energy equal to the kinetic energy of the electron and the ionization energy. For an isotropic target medium, this can happen twice per laser cycle, such that the resulting spectrum consists of odd integer harmonics of the fundamental light, as will be discussed.

After the tunneling, the electron can be described as a free electron and hence follows a classical trajectory. If we set the oscillating electric field of the laser to be $E(\phi) = E_0 \cos(\phi)$, with $\phi = \omega t$, we get the equation of motion for the electron starting with zero velocity;

$$x(\phi) = \frac{E_0\, e}{m_e\, \omega^2} \left[\cos(\phi_i) - \cos(\phi) - (\phi - \phi_i)\sin(\phi_i)\right] \ , \tag{2.34}$$

$$\dot{x}(\phi) = \frac{E_0\, e}{m_e\, \omega} \left[\sin(\phi) - \sin(\phi_i)\right] \ , \tag{2.35}$$

where ϕ_i is the phase of the fundamental laser field at which the electron tunnels. For values between 0 and $\frac{\pi}{2}$ the trajectory crosses the origin again, as seen in Figure 2.5, and recombination is possible. Using the ponderomotive energy and Equation 2.35, the kinetic energy for the electron is given by

$$E_\mathrm{kin}(\phi) = 2\, U_\mathrm{pond} \left(\sin(\phi) - \sin(\phi_i)\right)^2 \ . \tag{2.36}$$

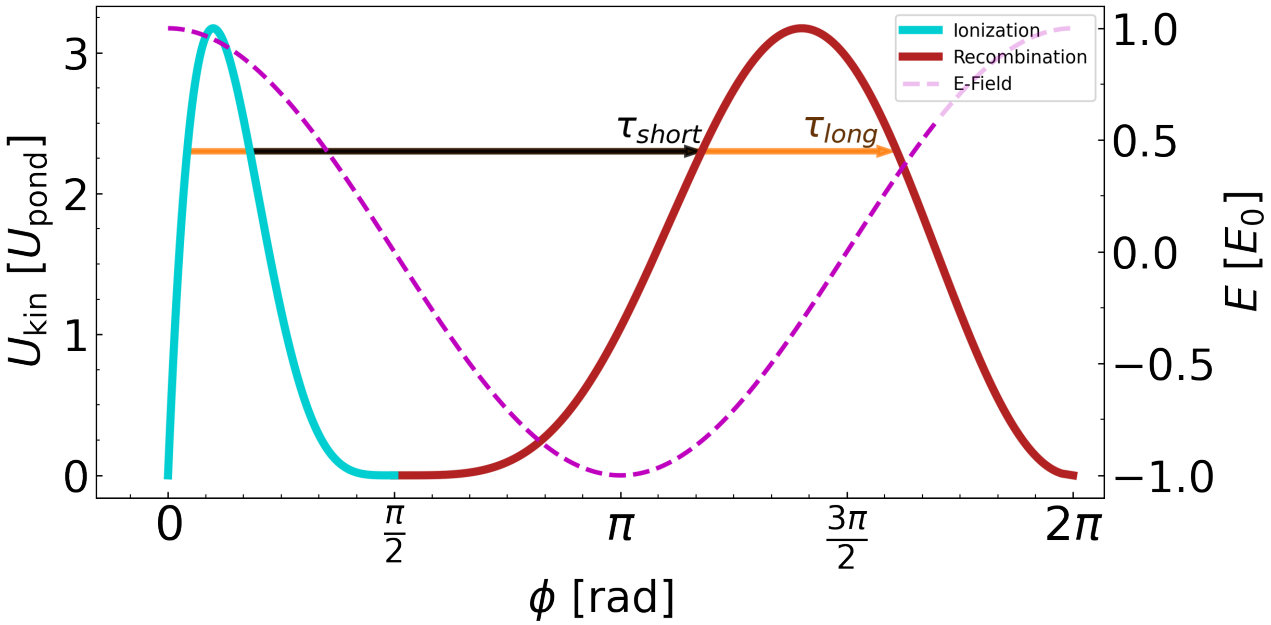

Figure 2.6.: Kinetic energy obtained by the electron propagating in the external electric field determined by the time of ionization and the phase of the driving electric field. Two trajectories that result in the same kinetic energy are marked with the orange and black arrow. The trajectory with a longer propagation time is called the long trajectory and vice versa. Taken from [50].

Together with the premise that the electrons crosses the origin

$$x\left(\phi > \phi_i\right) = 0\,. \tag{2.37}$$

The total energies that can be released as a photon are shown in Figure 2.6. The maximum excess energy of $3.17\,U_{\mathrm{pond}}$ is reached for $\phi_i = 0.31$, which gives the maximum photon energy that can be emitted, the so-called HHG cutoff energy:

$$E_{\mathrm{cut-off}} = 3.17\,U_{\mathrm{pond}} + U_{\mathrm{ion}}\,. \tag{2.38}$$

There are two trajectories of the electron that lead to the same kinetic energy, one with a longer time in the continuum until recombination. This trajectory is called the long trajectory while the other one where the tunneling occurs afterwards and the recombination before is called the short trajectory. Both have distinct characteristics as will be discussed in Section 2.1.4.2.

For every pair of solutions ϕ_i and ϕ of Equation 2.36, $\phi_i + \pi$ and $\phi + \pi$ are solutions as well, only with an opposite sign. The process repeats every half optical cycle but in the opposite direction. This leads to the spectrum consisting of odd order harmonics (i.e. odd multiples) of ω_{c} as given by the Fourier transform of the signal. For this purpose, we consider an arbitrary signal f_{s}, representing the the bursts of photons from recombination. To get the alternating behavior, we convoluted it with an alternating Dirac-comb $f_{\mathrm{comb}}\left(\phi\right) = \sum_{n=-\infty}^{\infty}\left(-1\right)^n \delta\left(\phi - n\Delta\phi\right)$ with $n \in \mathbb{N}$ and $\Delta\phi = \pi$. Since a finite pulse is driving the process, the function is multiplied with a Gaussian envelope $\mathcal{E}_{\mathrm{gauss}}(t)$, resulting in

$$g\left(t\right) = \left[f_s\left(t\right) * f_{\mathrm{comb}}\left(t\right)\right] \mathcal{E}_{\mathrm{gauss}}\left(t\right) \tag{2.39}$$

To simplify the Fourier transform, $f_{\mathrm{comb}}(t)$ can be rewritten as a Fourier series using $\phi = \omega_c\, t$;

$$f_{\mathrm{comb}}\,(t) = \sum_{k=-\infty}^{\infty} c_k\, e^{ik\omega_c t}\,, \tag{2.40}$$

with

$$c_k = \frac{\omega_c}{2\,\pi}\left[\int_0^{\frac{\pi}{\omega_c}} dt\delta\,(\omega_c\, t)\; e^{ik\omega_c t} \;-\; \int_{\frac{\pi}{\omega_c}}^{\frac{2\,\pi}{\omega_c}} dt\delta\,(\omega_c\, t - \pi)\; e^{ik\omega_c t}\, dt\right] \;= \frac{\omega_c}{2\,\pi}\left[1 - (-1)^k\right]\,. \tag{2.41}$$

The sum will go to zero for even k, hence Equation 2.40 and 2.41 can be rewritten setting $k \mapsto (2k+1)$ without loss of generality, resulting in

$$f_{comb}(t) = \frac{\omega_c}{\pi} \sum_{k=-\infty}^{\infty} e^{i(2k+1)\omega_c t}\,. \tag{2.42}$$

Using the Fourier series, the Fourier transform can be calculated to be

$$\widetilde{f}_{comb}(\omega) = \frac{\omega_c}{\pi} \int_{-\infty}^{\infty} dt \sum_{k=-\infty}^{\infty} e^{i(2k+1)\omega_c t} e^{-i\omega t} = 2\omega_c \sum_{k=-\infty}^{\infty} \delta\,(\omega - (2k+1)\,\omega_c)\,. \tag{2.43}$$

Utilizing the convolution theorem, the Fourier transform of 2.39 is

$$\widetilde{g}(\omega) = \left[2\omega_{\mathrm{c}} \sum_{k=-\infty}^{\infty} \widetilde{f}_s(\omega)\,\delta\,(\omega - (2k+1)\,\omega_c)\right] * \mathcal{E}_{gauss}(\omega). \tag{2.44}$$

This shows the occurrence of odd harmonics when using isotropic targets such as noble gases. When using a non-isotropic target, breaking the π symmetry ,it is possible to produce even harmonics [59, 60].

2.1.4.2. Quantum Theory of High Harmonic Generation

A quantum mechanical description is given by Lewenstein *et al.* [61], called the Lewenstein model. A short overview is given in this section.

The time-dependent Schrödinger equation in the length gauge for a particle in an oscillating electric field is given in natural units by

$$i\frac{\partial}{\partial t}\,|\Psi(x,t)\rangle = \left[-\frac{1}{2}\Delta^2 + V(x) - E\cos(t)x\right]|\Psi(x,t)\rangle\,, \tag{2.45}$$

with $V(x)$ being the atomic potential. The following three assumptions, which are widely used within the strong field approximation, are made to simplify further calculations:

1. Contributions of all states but the ground state $|0\rangle$ can be neglected for the evaluation of the system.

2. Depletion of the ground state can be neglected.

3. The contributions from the atomic potential $V(x)$ can be neglected. The electron is perturbing freely in the continuum according to the electric field.

With this approximation, the time-dependent wave functions can be expanded as

$$|\Psi\rangle = e^{i\,I_\mathrm{p} t}\left(a\,(t)\,|0\rangle + \int d^3\mathbf{v}\,b\,(\mathbf{v},t)\,|\mathbf{v}\rangle\right), \tag{2.46}$$

where $a \approx 1$ is the ground state amplitude and $b(v,t)$ are the corresponding amplitudes in the continuum state. The Schrödinger Equation for $b(v,t)$ reads as

$$\dot{b}(v,t) = -i\left(\frac{v^2}{2} + I_\mathrm{P}\right)b(v,t) - E\cos(t)\,\frac{\partial b(v,t)}{\partial v_x} + iE\,cos(t)\,d_x(v). \tag{2.47}$$

Here, $d(v) = \langle x|\,v\,|0\rangle$ indicates the atomic dipole matrix element for the bound-free transition and $d_x(v)$ represents the part parallel to the polarization axis. The Schrödinger Equation 2.45 can be solved for the following expression for $b(v,t)$:

$$\begin{aligned} b(v,t) = i\int_0^t dt'\,E\,\cos(t')\,d_x\left(v + A(t) - A(t')\right) \\ \times \exp -i\int_{t'}^{t'} dt''\,\left[(v + A(t) - A(t''))^2/2 + I_\mathrm{P}\right], \end{aligned} \tag{2.48}$$

with $A(t) = (-E\,\sin(t), 0, 0)$ denoting the vector potential of the driving laser field. Evaluating the x component of the time dependent dipole moment and introducing the canonical momentum

$$p = v + A(t) \tag{2.49}$$

leads to the expression

$$x(t) = i\int_0^t dt' \int d^3\mathbf{p}\;E\;\cos\left(t'\right)\,d_\mathrm{x}\left(\mathbf{p} - \mathbf{A}\left(t'\right)\right)\;d_x^*\;\left(\mathbf{p} - \mathbf{A}\left(t\right)\right)\;e^{-iS(\mathbf{p},t,t')} + c.c.\,, \tag{2.50}$$

where

$$S\left(\mathbf{p},t,t'\right) = \int_{t'}^{t} dt''\left(\frac{\left[\mathbf{p} - \mathbf{A}\left(t''\right)\right]^2}{2} + I_\mathrm{p}\right). \tag{2.51}$$

In this expression, $S(p,t',t)$ denotes the quasi-classical action and d_x^* denotes the complex conjugate of d_x. Equation 2.50 can be interpreted as probability amplitudes to following processes: The first term $E\,\cos(t')\,d_x\,(p - A(t'))$ is the probability amplitude for an electron to tunnel into the continuum at time t' with the canonical momentum p. The wave function of the electron propagates until time t acquiring a phase of $\exp\left[-i\,S(p,t,t')\right]$. Finally, at time t the electron recombines with an amplitude equal to $d_x^*(p - A(t))$.

A saddle-point analysis of Equation 2.51 shows that in the quasi-classical limit the integral reduces to a sum over relevant paths. The phase components of each constituent are the result of the acquired phase by the electron in the continuum and due to the delay of the ionization time. The phase can be written down for harmonic order q by [62]

$$\Phi_i = q\,\omega_\mathrm{l} t' - \frac{1}{\hbar}S(p,t,t'). \tag{2.52}$$

Two of these trajectories play a dominant role, one with a return time t_1' and the other with a later return time of t_2', very close to a full period of the driving laser field [61]. The two components relate to the short and long trajectory, respectively. An exception is made for a

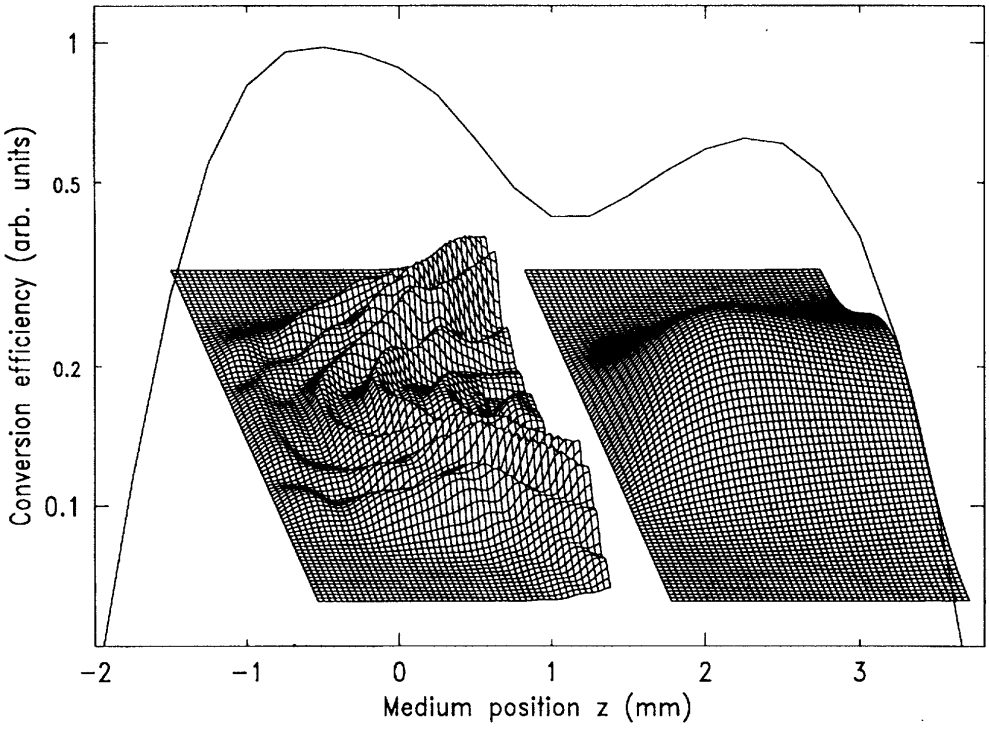

Figure 2.7.: The conversion efficiency according to the center position of the medium for the 45^{th} harmonic of a 835 nm driving laser. The 3D plots depict the magnitude of the harmonic field for the medium being at z=-1 (left) and z=3 (right) as a function of z (horizontal axis) and r (direction perpendicular to the plane of the figure). Taken from [64].

harmonic in the cut-off region where the contributions are reduced to one path. Only taking the two relevant contributions $i = 1, 2$ into account, Equation 2.52 reduces to [63]

$$\Phi_i = -\alpha_i I(r, z, t). \tag{2.53}$$

Here, $I(r, z, t)$ is the space- and time-dependent intensity of the laser field and α_i is the respective slope of the phase components. When using a pulse to generate harmonics, the variation of the intensity in time induces a change in the instantaneous frequency, i.e. a chirp, $\Delta\omega_i(t) = -\partial\Phi_i(t)/\partial t$. This leads to spectral broadening or equivalently a reduction in coherence time of the harmonics. Likewise, a variation in the radial intensity $I(r)$ induces a curvature of the phase front, which makes the beam strongly divergent for large α or $I(r)$. For the spectral broadening due to the chirp, the ratio of the spectral widths $\Delta\omega_i$ is given by

$$\frac{\Delta\omega_2}{\Delta\omega_1} = 27. \tag{2.54}$$

The contributions from the component relating to the short trajectory $i = 1$ shows a higher degree of coherence and less divergence. Since the intensity distribution of the focal volume is of great importance for the harmonic build up, the position of the focus relative to the medium influences the yield as can be seen in Figure 2.7 [64, 62]. The geometric conditions can ultimately favor either trajectory [65].

2.1.4.3. Macroscopic Response

With the generation of a single high energy photon in response to an intense driving laser field discussed, the superposition of many such responses has to be taken into account. The HHG process itself is coherent and so the total yield of the bulk medium depends on the phase-matching and re-absorption of the generated photons. For an efficient build up, the phase front of the generated field has to match that of the driving field. When using a Gaussian beam to focus into the medium to produce high harmonics, the following four contributions to the phase mismatch Δk exist

$$\Delta k = \Delta k_{\mathrm{G}} + \Delta k_{\mathrm{d}} + \Delta k_{\mathrm{n}} + \Delta k_{\mathrm{p}}. \tag{2.55}$$

The different constituents are:

1. Δk_{G} - Guoy Phase:
   Gaussian beams acquire an additional phase shift compared to plane waves when propagating through the focus. The phase is given by [66]

   $$\phi_{\mathrm{Guoy}}(r,z) = -\tan\left(\frac{z}{z_{\mathrm{R}}}\right) + \frac{k_1 r^2}{2\,R(z)}. \tag{2.56}$$

   The phase mismatch at the optical axis ($r = 0$) for the q^{th} harmonic is therefore

   $$\Delta k_{\mathrm{G}} = q\frac{\partial \phi_{\mathrm{Guoy}}(z)}{\partial z}\bigg|_{z\to 0} = -\frac{q}{z_{\mathrm{z}}}. \tag{2.57}$$

2. Δk_{d} - Dipole phase:
   The wave vector mismatch is induced by the dipole phase of the electron propagating in the continuum. Using Equation 2.53 the mismatch is

   $$\Delta k_{\mathrm{d}} = -\alpha_i(q)\frac{\partial I(r,z)}{z}. \tag{2.58}$$

3. Δk_{n} - Neutral dispersion:
   The gas pressure P dependent mismatch due to neutral gas dispersion can be written as

   $$\Delta k_{\mathrm{d}} = q\frac{\omega_{\mathrm{c}}}{c}P(1-\eta)(n_0 - n_q + n_2 I), \tag{2.59}$$

   with n_0 and n_q being the refractive indices of the medium for the driving laser and the generated harmonic beam, respectively, while n_2 denotes the intensity-dependent index of refraction. η indicates the ionization fraction.

4. Δk_{p} - Plasma dispersion:
   Since the probability of an electron to recombine in each cycle is relatively small, the freed electrons form a plasma together with their parent ions. When neglecting the dispersion from the ions due to their large mass and higher resonance frequency, the wave vector mismatch can be written as [67]

   $$\Delta k_{\mathrm{p}} = -q\frac{\omega_{\mathrm{c}}}{c}(n_{0,\mathrm{el}} - n_{q,\mathrm{el}}) \approx -q\frac{\omega_{\mathrm{c}}}{2\pi c}P\nu N_{\mathrm{a}} r_{\mathrm{e}}. \tag{2.60}$$

   Here, N_{a} denotes the atomic number density and r_{e} the classical electron radius.

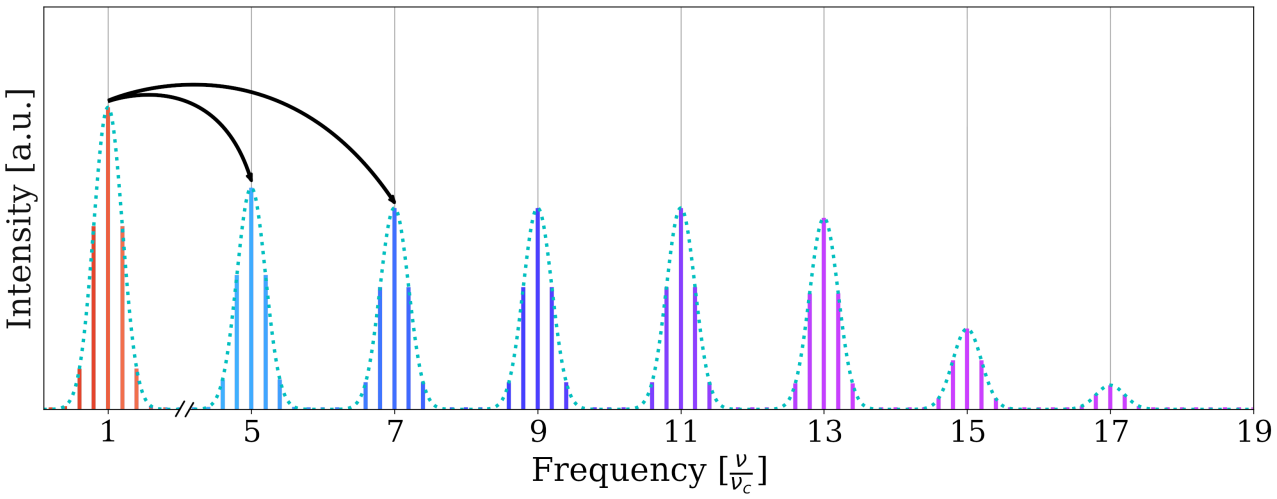

Figure 2.8.: The spectrum of high harmonics generated by a train of pulses transferring the driving comb structure to higher frequencies.

2.1.5. XUV Frequency Comb

The individual bursts of photons generated by HHG during a single pulse are shown to be phase coherent [68] while possessing a high degree of spatial coherence [69]. However, when driving the process with a train of pulses, the individual responses of subsequent pulses do not inhibit this coherence. Hence, the driving pulse train needs to be coherent by itself, such that the individual HHG responses are generated at periodic intervals leading to a convolution according to Equation 2.27. This leads to a copy of the driving comb structure to the q^{th} harmonic, i.e. centered around $q\,\omega_c$ as seen in Figure 2.8. Since the electric field oscillates q times faster, the CEO frequency increases by the same factor. This leads to a modified version of Equation 2.31 that reads

$$f_{n,q} = n\,f_{\text{rep}} + q\,f_{\text{CEO}}\ . \tag{2.61}$$

To successfully transfer the driving comb structure, the HHG process has to be driven coherently over multiple driving pulses. It was experimentally shown, that this is possible with coherence times as long as one second, corresponding to 154 million pulses [30].

2.2. Light-Matter Interaction

We aim to investigate and utilize the interaction between atoms and electromagnetic fields. In the upcoming sections, the coupling of a simple atomic two-level system to an external light field will be studied. This approximation is valid when the light field is resonant or near-resonant with the atomic transition, while other transitions remain highly detuned. The semi-classical approach we will follow is summarized from [70, 71], where the two-level system interacts with a single mode of a classical field.

Considering a single free electron, the motion is governed by the Schrödinger Equation

$$\frac{-\hbar}{2m}\nabla^2 |\Psi\rangle = i\hbar\frac{\partial}{\partial t}|\Psi\rangle \ , \tag{2.62}$$

where the probability density $P(r,t)$ of finding the electron at position r at time t is given by

$$P(r,t) = |\Psi(r,t)|^2 \ . \tag{2.63}$$

Solutions of the Schröding Equation that differ only by a constant global phase, i.e. $|\Psi\rangle$ and $e^{i\alpha}|\Psi\rangle$, represent the same physical state. This is not the case when the phase varies locally, i.e.

$$|\Psi\rangle \mapsto |\Psi\rangle\, e^{i\,\alpha(\mathbf{r},t)} \ . \tag{2.64}$$

While the probability $P(\mathbf{r},t)$ stays unaffected, the Schrödinger Equation (Eq. 2.62) is no longer satisfied. To satisfy local gauge invariance, additional terms have to be added. Introducing the vector field $\mathbf{A}(\mathbf{r},t)$ and the scalar field $U(\mathbf{r},t)$, to allow for the transformation given by Equation 2.64, modifies the Schrödinger equation to

$$\left\{-\frac{\hbar^2}{2m}\left[\nabla - i\frac{e}{\hbar}\mathbf{A}(\mathbf{r},t)\right]^2 + eU(\mathbf{r},t)\right\}|\Psi\rangle = i\hbar\frac{\partial}{\partial t}|\Psi\rangle \ , \tag{2.65}$$

with

$$\mathbf{A}(\mathbf{r},t) \mapsto \mathbf{A}(\mathbf{r},t) + \frac{\hbar}{e}\nabla\alpha(\mathbf{r},t) \ , \tag{2.66}$$

$$U(\mathbf{r},t) \mapsto U(\mathbf{r},t) - \frac{\hbar}{e}\nabla\frac{\partial}{\partial t}\alpha(\mathbf{r},t) \ . \tag{2.67}$$

$\mathbf{A}(\mathbf{r},t)$ and $U(\mathbf{r},t)$ are given by the gauge-dependent vector and scalar potentials of the electromagnetic field that are related to the electric and magnetic fields as followed:

$$\mathbf{E} = -\nabla U - \frac{\partial}{\partial t}\mathbf{A} \tag{2.68a}$$

$$\mathbf{B} = \nabla \times \mathbf{A} \tag{2.68b}$$

We will be treating the theoretical description in the radiation gauge, in which

$$U(\mathbf{r},t) = 0 \ , \tag{2.69}$$

and

$$\nabla \cdot \mathbf{A} = 0 \ . \tag{2.70}$$

Finally, as the interaction of bound electrons will be studied, a static binding potential $V(r)$ is introduced, that is given by the nucleus located at r_0. This results in the minimal-coupling Hamiltonian

$$\hat{H} = -\frac{\hbar^2}{2m}\left[\nabla - i\frac{e}{\hbar}\mathbf{A}(\mathbf{r},t)\right]^2 + V(\mathbf{r}) \; . \tag{2.71}$$

The Hamilonian can be further simplified by introducing the dipole approximation, where $\mathbf{k}\cdot\mathbf{r} \ll 1$. Albeit we intend to do spectroscopy with short wavelengths utilizing Rydberg states, the wavelength is on the order of 80 nm, while the low-n ($n < 12$) Rydberg states of interest lead to orbits of a few nanometers, justifying the approximation. Hence, the vector potential can be Taylor expanded around r_0 to

$$\begin{aligned} \mathbf{A}(\mathbf{r_0}+\mathbf{r},t) &= A(t)\,\exp(i\mathbf{k}\cdot(\mathbf{r_0}+\mathbf{r})) \\ &= \mathbf{A}(t)\,\exp(i\mathbf{k}\cdot\mathbf{r_0}(1+i\mathbf{k}\cdot\mathbf{r}+...)) \\ &\approx \mathbf{A}(t)\,\exp(i\mathbf{k}\cdot\mathbf{r_0}) \; . \end{aligned} \tag{2.72}$$

Using the minimal coupling Hamiltonian of Equation 2.71 to write down the Schrödinger Equation in the dipole approximation with $\mathbf{A}(\mathbf{r},t) \equiv \mathbf{A}(\mathbf{r_0},t)$ results in

$$\left\{-\frac{\hbar^2}{2m}\left[\nabla - i\frac{e}{\hbar}A(\mathbf{r_0},t)\right]^2 + V(\mathbf{r})\right\}|\Psi\rangle = i\hbar\frac{\partial}{\partial t}|\Psi\rangle \; . \tag{2.73}$$

Further simplification can be done by applying the gauge transformation $\alpha(\mathbf{r},t) = -e\mathbf{A}(\mathbf{r_0},t)\mathbf{r}/\hbar$ resulting in

$$\hat{H}\,|\Psi\rangle = \left[\hat{H}_0 + \hat{H}_1\right]|\Psi\rangle = i\hbar\frac{\partial}{\partial t}|\Psi\rangle \; , \tag{2.74}$$

where

$$\hat{H}_0 = \frac{\hbar}{2m}\nabla^2 + V(\mathbf{r}) \tag{2.75}$$

is the unperturbed Hamiltonian of the electron. While

$$\hat{H}_1 = -e\mathbf{r}\cdot\mathbf{E}(\mathbf{r_0},t) \tag{2.76}$$

is the perturbation given by the electric field in terms of the gauge-independent field E. This Hamiltonian will be used in the subsequent studies of atom-light interactions.

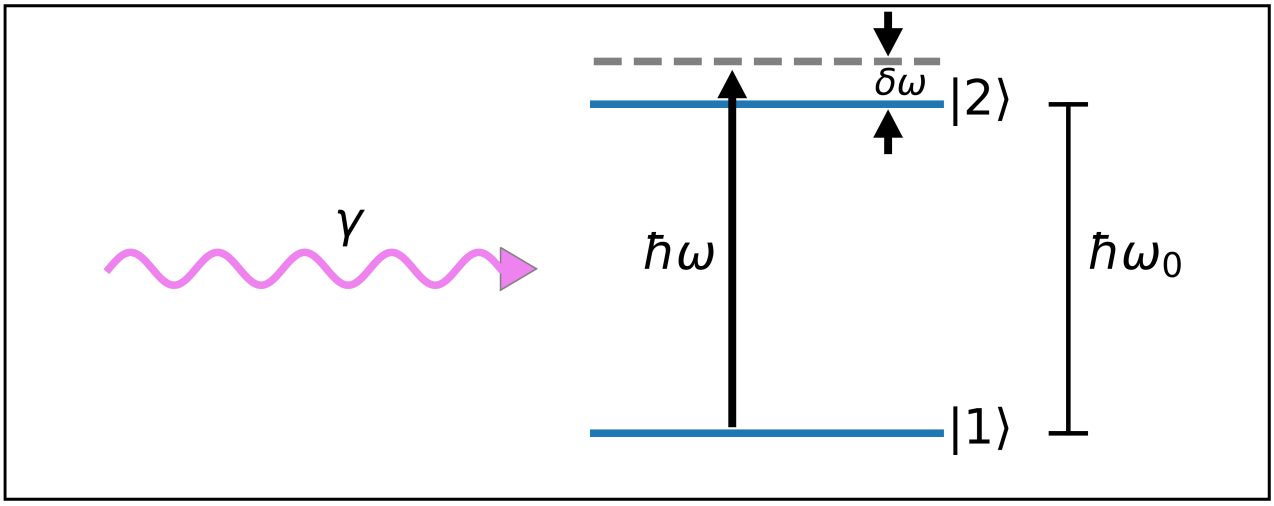

Figure 2.9.: Schematic of a two level system with energy spacing $\hbar\omega_0$ interacting with an incoming photon γ. The photon has an energy of $\hbar\omega$ and is detuned to the transition by $\delta\omega$.

2.2.1. Two Level Resonant Light-Atom Interaction

Following the perturbation approach, the unperturbed two level system has two energy levels E_1 and E_2 which are subject to a light field of angular frequency ω. This two-level approximation is justified when the driving light field is resonant only with one transition at a time while being far detuned to others. This is achieved by a sufficiently narrow bandwidth of the driving field. Hence, the angular frequency can be rewritten as

$$\omega = \omega_0 + \delta\omega \ , \tag{2.77}$$

where

$$\omega_0 = (E_2 - E_1)/\hbar \ , \tag{2.78}$$

and $\delta\omega \ll \omega_0$. We call $\delta\omega$ the detuning. Starting with the unperturbed system, the two solutions, corresponding to the two energy levels, given by

$$\hat{H}_0 \left|\Psi_i(\mathbf{r},t)\right\rangle = i\hbar\frac{\partial}{\partial t}\left|\Psi_i(\mathbf{r},t)\right\rangle \tag{2.79}$$

are

$$\left|\Psi_i(\mathbf{r},t)\right\rangle = \phi_i(\mathbf{r})\exp(-iE_it/\hbar) \ , \{i=1,2\} \ , \tag{2.80}$$

where

$$\hat{H}_0\phi_i(\mathbf{r}) = E_i\phi_i(\mathbf{r}) \ . \tag{2.81}$$

The general solution is given by the superposition of the eigenstates of the system. In the case of a two-level system this is simply given by

$$\left|\Psi_i(\mathbf{r},t)\right\rangle = c_1(t)\phi_1(\mathbf{r})e^{-iE_1t/\hbar} + c_2(t)\phi_{\mathbf{2}}(r)e^{-iE_2t/\hbar} \ . \tag{2.82}$$

Plugging it back into the Schroeding Equation, given by Equation 2.74, yields

$$\left[\hat{H}_0\hat{H}_1\right]\left(c_1(t)\phi_1(\mathbf{r})e^{-iE_1t/\hbar} + c_2(t)\phi_2(\mathbf{r})e^{-iE_2t/\hbar}\right) = i\hbar[(\dot{c}_1 - iE_1c_1/\hbar)\,\phi_1e^{-iE_1t/\hbar} + (\dot{c}_2 - iE_2c_2/\hbar)\,\phi_2e^{-iE_2t/\hbar}] \ . \tag{2.83}$$

The dependence of ϕ_i on $\mathbf{r}$ was omitted for clarity. Taking Equation 2.79 into account, several terms get canceled out, leaving

$$c_1\hat{H}_1\phi_1 e^{-iE_i t/\hbar} + c_2\hat{H}_1\phi_2 e^{-iE_2 t/\hbar} = i\hbar\dot{c}_1\phi_1 e^{-iE_1 t/\hbar} + i\hbar\dot{c}_2\phi_2 e^{-iE_2 t/\hbar}\,. \tag{2.84}$$

On multiplying by $\langle\phi_1|$ and $\langle\phi_2|$, integrating over the space and utilizing the orthonormality of the eigenfunctions, following equations are obtained for the amplitudes $c_{1,2}$:

$$\dot{c}_1(t) = -\frac{i}{\hbar}\left(c_1(t)\,\langle\phi_1|\,\hat{H}_1\,|\phi_1\rangle + c_2(t)\,\langle\phi_1|\,\hat{H}_1\,|\phi_2\rangle\,e^{-i\omega_0 t}\right)\,, \tag{2.85a}$$

$$\dot{c}_2(t) = -\frac{i}{\hbar}\left(c_1(t)\,\langle\phi_2|\,\hat{H}_1\,|\phi_1\rangle\,e^{-i\omega_0 t} + c_2(t)\,\langle\phi_1|\,\hat{H}_1\,|\phi_2\rangle\right)\,. \tag{2.85b}$$

Now, the expectation values of the perturbation Hamiltonian, given by Equation 2.76, need to be calculated. For that, an electric field is chosen that is linearly polarized along the z-axis with angular frequency ω,

$$\mathbf{E}(t) = (0, 0, E_0)\cos(\omega t)\,, \tag{2.86}$$

where E_0 is the amplitude of the light field. The pertubation simplifies to

$$\hat{H}_1 = \frac{exE_0}{2}(e^{i\omega t} + e^{-i\omega t})\,, \tag{2.87}$$

using trigonometric identities. Accordingly, the expectation value is given by:

$$\langle i|\,\hat{H}_1\,|j\rangle = \frac{eE_0}{2}(e^{i\omega t} + e^{-i\omega t})\,\langle i|\,x\,|j\rangle\,\,. \tag{2.88}$$

The dipole matrix element, given by

$$\mu_{ij} = -e\,\langle i|\,x\,|j\rangle\,\,, \tag{2.89}$$

simplifies the treatment further, together with the Rabi frequency

$$\Omega_R = |\mu_{12}E_0/\hbar|\,. \tag{2.90}$$

We obtain:

$$\dot{c}_1(t) = i\frac{E_0\mu_{12}}{2\hbar}\left(e^{i(\omega-\omega_0)t} + e^{-i(\omega+\omega_0)t}\right)c_2(t), \tag{2.91a}$$

$$\dot{c}_2(t) = i\frac{E_0\mu_{12}}{2\hbar}\left(e^{-i(\omega-\omega_0)t} + e^{i(\omega+\omega_0)t}\right)c_1(t). \tag{2.91b}$$

These are the equations we have to solve to understand the interaction of the atom with the light field. It turns out that there are two limits to address, which are the weak-field limit and the strong-field limit. Due to the nature of the high harmonic generation as well as the fact that only a single frequency comb tooth, only a small fraction of the power is resonant at a time in the order of pW. Hence we will concentrate on the weak-field limit.

2.2.2. The Weak-Field Limit

The radiation source in our setup will lead to ≈pW of available resonant power to drive the atom-light interaction. With the atom initially in the lower level and the radiation turned on at $t = 0$, the amplitudes are $c_1(0) = 1$ and $c_2(0) = 0$. Since the perturbation is weak, only a small number of transitions are expected such that $c_1(t) \gg c_2(t)$. We can put $c_1(t) = 1$ for all t, which reduces Equation 2.91a to:

$$\dot{c}_1(t) = 0 \,, \tag{2.92a}$$

$$\dot{c}_2(t) = \frac{i}{2}\Omega_{\mathrm{R}} \left(e^{-i(\omega-\omega_0)t} + e^{i(\omega+\omega_0)t}\right) \,. \tag{2.92b}$$

The solution for $c_2(t)$ wit $c_2(0) = 0$ is :

$$c_2(t) = \frac{i}{2}\Omega_{\mathrm{R}} \left[\frac{e^{-\delta\omega t} - 1}{-i\delta\omega} + \frac{e^{i(\omega+\omega_0)t} - 1}{i(\omega+\omega_0)}\right] . \tag{2.93}$$

Doing the rotating wave approximation, the fast oscillating terms can be neglected, i.e. drop the second term of equation 2.93. This is justified close to resonance where $\delta\omega \ll (\omega + \omega_0)$ and so the second terms is much smaller than the first. After simplifying we find:

$$|c_2(t)|^2 = \left(\frac{\Omega_R}{2}\right)^2 \left(\frac{\sin(\delta\omega t/2)}{\delta\omega/2}\right)^2 . \tag{2.94}$$

The finite width $\delta\omega$ of the transition has to taken into account as well as the spectrum of the radiation field. It can be characterized the spectrum of the radiation source with its spectral energy density $u(\omega)$, which satisfies:

$$\frac{1}{2}\epsilon_0 E_0 = \int u(\omega) d\omega \qquad . \tag{2.95}$$

Integrating Equation 2.94 over the spectral line leads to following expression:

$$|c_2(t)|^2 = \frac{\mu_{12}^2}{2\epsilon_0\hbar^2} \int_{\omega_0-\Delta\omega/2}^{\omega_0+\Delta\omega/2} u(\omega) \left(\frac{\sin((\omega-\omega_0)t/2)}{(\omega-\omega_0)/2}\right)^2 d\omega \,. \tag{2.96}$$

For simplification, the approximation that the spectral line is sharp compared to the spectrum of the radiation source can be made. This is the case when probing narrow transitions. Hence, $u(\omega)$ does not vary greatly within the integral and can be replaced with the constant $u(\omega_0)$. Evaluating the integral for the limit $t\Delta\omega \mapsto \infty$ equates to $u(\omega_0)2\pi t$. Hence we obtain:

$$|c_2(t)|^2 = \frac{\pi}{\epsilon_0\hbar^2}\mu_{12}^2 u(\omega_0) t \,, \tag{2.97}$$

We can relate this solution the the Einstein B coefficient which is defined as:

$$\frac{dN_2}{dt} = B_{12}^{\omega} u(\omega_0) N_1 \,, \tag{2.98}$$

where the transition probability per atom is given by $B_{12}^{\omega}u(\omega_0)$. Since the dipoles in a gas of atoms are oriented randomly, the average over the orientation angle θ between the polarization axis and the atomic dipole needs to be considered. Explicitly, the average of $\langle(\mu_{12}\cos(\theta))^2\rangle = \mu_{12}1/3$ has to be taken. With this, the transition rate W_{12} is given by

$$W_{12} \equiv B_{12}^{\omega} u(\omega_0) = \frac{|c_2(t)|^2}{t} = \frac{\pi}{3\epsilon_0\hbar^2}\mu_{12}^2 u(\omega_0) \,, \tag{2.99}$$

from where the expression for the Einstein B-coefficient

$$B_{12}^{\omega} = \frac{\pi}{3\epsilon_0 \hbar^2} \mu_{12}^2 \tag{2.100}$$

is deducted. Here, the equivalence of the weak-field limit to Einsteins analysis was shown and how explicit values for the Einstein B coefficient can be calculated from atomic wave functions.

2.2.3. Photoionization

The previous analysis of resonant light matter interaction can be tied to a transition between a state and the continuum. The description of V. T. Davis will be followed [72].

Starting from Hamiltonian and the perturbation given by the dipole interaction from Equation 2.76. In the dipole approximation, the differential cross section for a single photon bound-free transition between the initial $|i\rangle$ and final continuum state $|f\rangle$ is proportional to

$$\frac{d\sigma_{\mathrm{pd}}}{d\hat{\Omega}} \propto |\langle i|\hat{O}|f\rangle|^2 , \tag{2.101}$$

where the dipole operator $\hat{O}$ is introduced to explicitly include the angle between the polarization and the atomic dipole moment. For a linearly polarized photon, along the z-axis, it is defined as

$$\hat{O} = r\cos(\theta) = r\sqrt{\frac{4\pi}{3}}Y_{10}(r) = rC_0^{(1)}(r) . \tag{2.102}$$

The operator can be expressed in terms of normalized spherical harmonic tensor operators

$$C_q^{(k)}(r) = \sqrt{\frac{4\pi}{2k+1}}Y_{kq}(r) . \tag{2.103}$$

The initial state is given by the wave function of the bound electron. Whereas, the final state of the photoelectron is in the continuum and needs to be modeled. One way to model the final state is as a plane wave plus an incoming spherical wave:

$$|f\rangle \propto \left[e^{ikz} + \frac{f(\theta)}{r}e^{-ikr}\right] , \tag{2.104}$$

where k is the wave number of the photoelectron and $f(\theta)$ a form factor to take the effect of the atomic potential onto the photoelectron into account. The asymptotic form of the final state is

$$|f\rangle \propto_{r\mapsto\infty} \sum_{l=0}^{\infty}(2l+1)i^l e^{-i\delta_l}P_l(\cos(\theta))\left[\frac{e^{i\delta_l}\sin(kr-\frac{l\pi}{2}) + e^{-i(kr+\frac{l\pi}{2})}\sin(\delta_l)}{kr}\right] , \tag{2.105}$$

with δ_l being the phase shift of the l^{th} partial wave. Which can be rewritten in terms of spherical harmonics to

$$|f\rangle \propto 4\pi\sum_{l,m}(i)^l e^{-i\delta_l}Y_{lm}^*(k)Y_{lm}(r)G_{kl}(r) , \tag{2.106}$$

here k is the unit vector along the direction of momentum of the photoelectron and

$$G_{kl}(r) = \frac{e^{i\delta_l}\sin(kr-\frac{l\pi}{2}) + e^{-i(kr+\frac{l\pi}{2})}\sin(\delta_l)}{kr} \tag{2.107}$$

is the radial portion of the final-state wave function. Hence, the matrix element of Equation 2.101 is given by

$$\langle f|rC_0^{(1)}(r)|i\rangle = 4\pi\sum_{l,m}(i)^l e^{-i\delta_l}Y_{lm}^*(k)\langle l,m|C_0^{(1)}(r)|l',m'\rangle\int_0^{\infty} r^3 R_{nl'}(r)G_{kl}(r)dr . \tag{2.108}$$

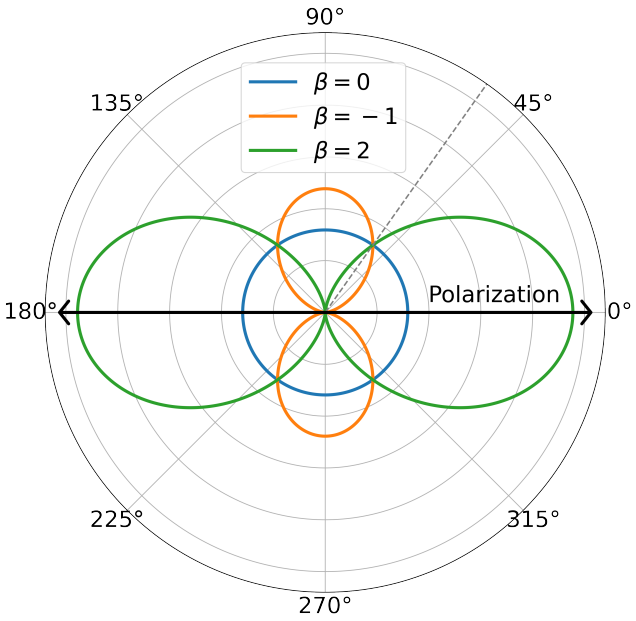

Figure 2.10.: Polar photoelectron distribution for asymmetry parameter $\beta \in [-1, 0, 2]$ relative to the polarization axis. Note that the distribution at 54.74 °is indepedent of β.

Caution, Expression 2.108 assumes LS-coupling and ignores interactions between the photoelectron and the core.

The integral is the radial dipole integral $\mathfrak{R}_l$

$$\mathfrak{R}_l \equiv \int_0^\infty r^3 R_{nl'}(r) G_{kl}(r) dr \ . \tag{2.109}$$

To solve for the matrix element, a lot of algebra is required, which can be looked up in [72]. Instead, the important solutions and quantities of a photoelectron ionized from a state with orbital momentum l_0 are given by

$$I(\theta) = \frac{d\sigma_{pd}}{d\Omega} = \frac{\sigma_{pd}}{4\pi} \left[1 + \beta P_2(\cos(\theta))\right] \tag{2.110a}$$

$$\sigma_{pd} = \frac{16\pi^2}{3(2l_0)+1} \left[l_0 \mathfrak{R}^2_{l_0-1} + (l_0+1)\mathfrak{R}^2_{l_0+1}\right] \tag{2.110b}$$

$$\beta = \frac{\left[l_0(l_0-1)\mathfrak{R}^2_{l_0-1} + (l_0+1)(l_0+2)\mathfrak{R}^2_{l_0+1} - 6l_0(l_0+1)\mathfrak{R}_{l_0-1}\mathfrak{R}_{l_0+1}\cos(\delta_{l_0+1} - \delta_{l_0-1})\right]}{(2l_0+1)\left[l_0\mathfrak{R}^2_{l_0-1} + (l_0+1)\mathfrak{R}^2_{l_0+1}\right]} \tag{2.110c}$$

$$P_2(\cos(\theta)) = \frac{1}{2}(3\cos^2(\theta) - 1) \tag{2.110d}$$

$$\mathfrak{R}_{l_0\pm1} = \int_0^\infty r^3 R_{nl_0}(r) G_{k,l_0\pm1}(r) dr \tag{2.110e}$$

The angular distribution of the photoelectrons is described by the asymmetry parameter β which has to be $-1 \geq \beta \geq 2$ so that the intensity $I(\theta)$ stays positive. The angular distributions for different asymmetry parameters are shown in Figure 2.10.

3. | Femtosecond Enhancement Cavity

This chapter introduces the experimental setup designed to generate the XUV frequency comb and outlines the preparatory work undertaken to ensure consistent operation. The efficacy of the setup was demonstrated during testing of the gas recycling system and the noise characterized.

3.1. Experimental Setup

The experimental setup, illustrated in Figure 3.1, can be divided into two primary components. Firstly, the amplification and temporal compression of the NIR frequency comb (Menlo Systems FC 1000) generates intense short laser pulses, which are subsequently coupled into the femtosecond (fs) enhancement cavity, constituting the second part of the setup. Within the enhancement cavity, these laser pulses are passively amplified to drive HHG and generate the XUV frequency comb. The setup was constructed and described in depth by J. Nauta and J.H.Oelmann [32, 73, 33].

3.1.1. Laser System

The uncompressed NIR frequency comb delivers 24 ps long pulses centered around 1039 nm with a full width at half maximum (FWHM) of 14 nm at a repetition rate of 100 MHz. The repetition rate can be stabilized to a 10 MHz reference either from the built-in GPS referenced oscillator, with a fractional uncertainty of 10^{-12}, or an external source. For enhanced stability, the system can accept an optical reference. The CEO (Carrier Envelope Offset) can be manually adjusted or locked to 20 MHz. It is crucial to evaluate whether a slow drift on the order of MHz/min justifies the free adjustment of the CEO. Since maximum cavity enhancement occurs when the CEO matches the dispersion of the cavity, we opted to let the CEO run freely and manually readjust it to achieve maximum enhancement. The pulses are subsequently amplified by a

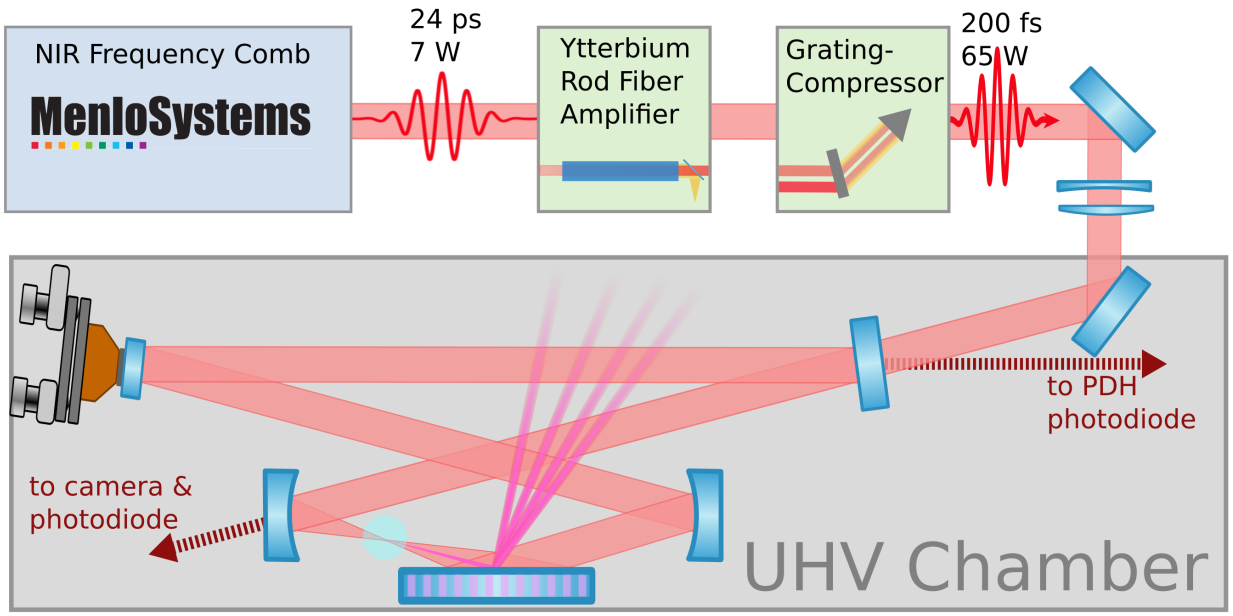

Figure 3.1.: Schematic of the XUV comb setup, where a NIR frequency comb gets amplified, compressed and coupled into an enhancement cavity inside a vacuum chamber. The cavity length is locked to the comb by the PDH technique using the reflected light. The transmitted light that is send to the camera and a photodiode is used to monitor the intracavity power and the cavity mode.

home-built amplifier [32, 33] based on a Yb-doped rod-type large-mode-area fiber (aeroGAIN rod module 2.0 PM85, NKT photonics). The fiber is pumped by a 976 nm cw pump laser with up to 250 W. To ensure proper in-coupling of the comb into the fiber, part of the exit beam can be imaged onto a camera verifying the mode and avoid damaging the amplifier by pumping it without a proper seed. The pulses are compressed back in a grating compressor setup, where a spectral path length difference is introduced by a grating and a retro-reflector. This reverses the chirp introduced by the comb that is needed to amplify the pulses without damaging the amplifier. In the end, the pulses are 200 fs long with an average power of 65 W which can be coupled into our enhancement cavity with a mode-matching telescope.

3.1.2. fs Enhancement Cavity

To amplify the laser intensities sufficiently to drive HHG ($\sim 10^{14}\,\mathrm{W\,cm^{-2}}$), the pulses are passively enhanced using a femtosecond enhancement cavity, as depicted in Figure 3.1 and 3.2. The enhancement is achieved by ensuring constructive interference of successive pulses when coupled into the cavity. Consequently, the total round trip length must be 3 m to match the 100 MHz repetition rate of our frequency comb, allowing for enhancement factors of up to 300, resulting in a circulating power on the order of 20 kW. Tight focusing is required to achieve the necessary peak intensities, leading to the use of a bow-tie configuration with a short arm for focusing and a long arm to achieve the 3 m round trip length, featuring a beam waist of 15 μm at the focus. The short arm, detailed in Figure 3.3, includes a gas nozzle enclosed in a differential pumping system to ensure a good vacuum in the main vacuum chamber. This is crucial for experiments requiring high vacuum, such as ion traps with highly charged ions, where loss occurs due to charge transfer with residual gas atoms. The differential pumping system comprises three

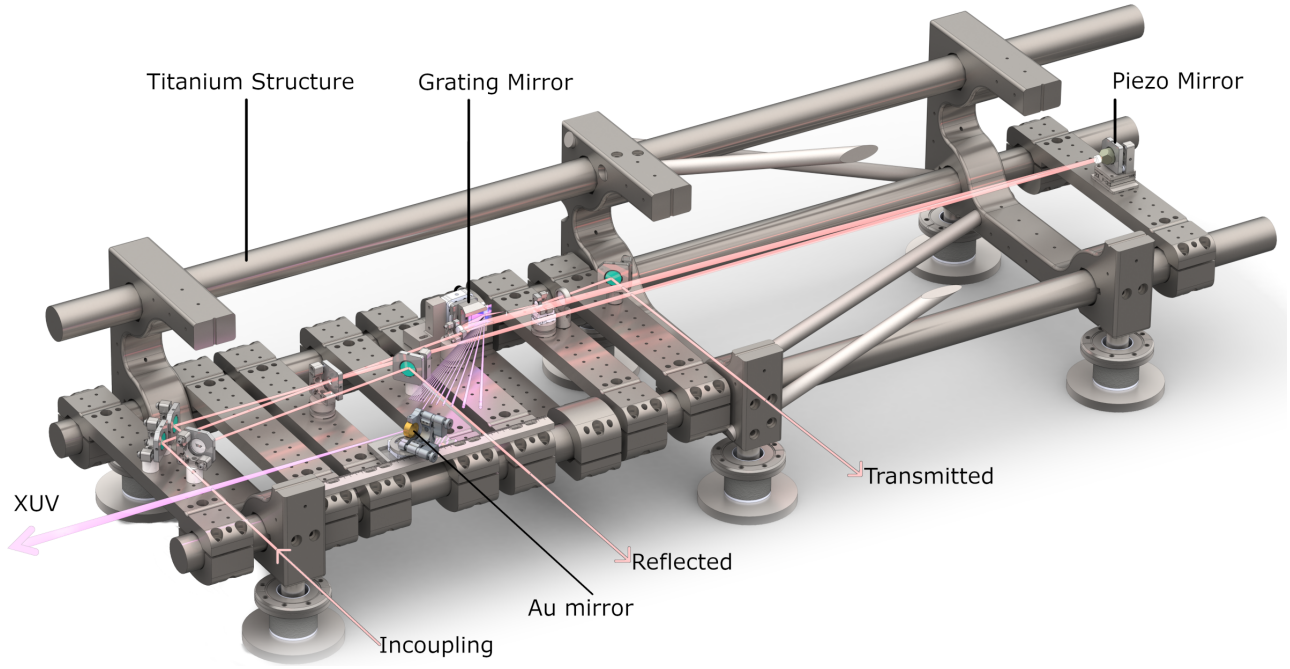

Figure 3.2.: Titanium structure that houses the passive enhancement cavity with the in- and outcoming beams marked.

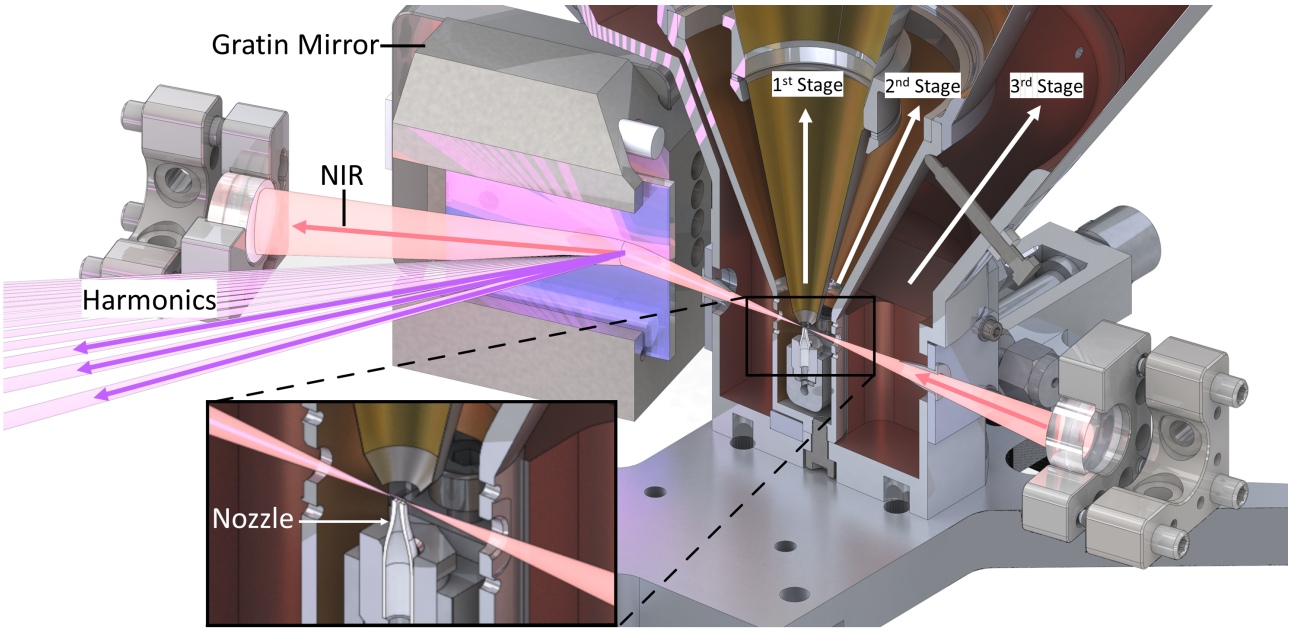

Figure 3.3.: Focus region of the fs-enhancement cavity with a close up of the gas nozzle delivering the gas for HHG nested inside the differential pumping system.

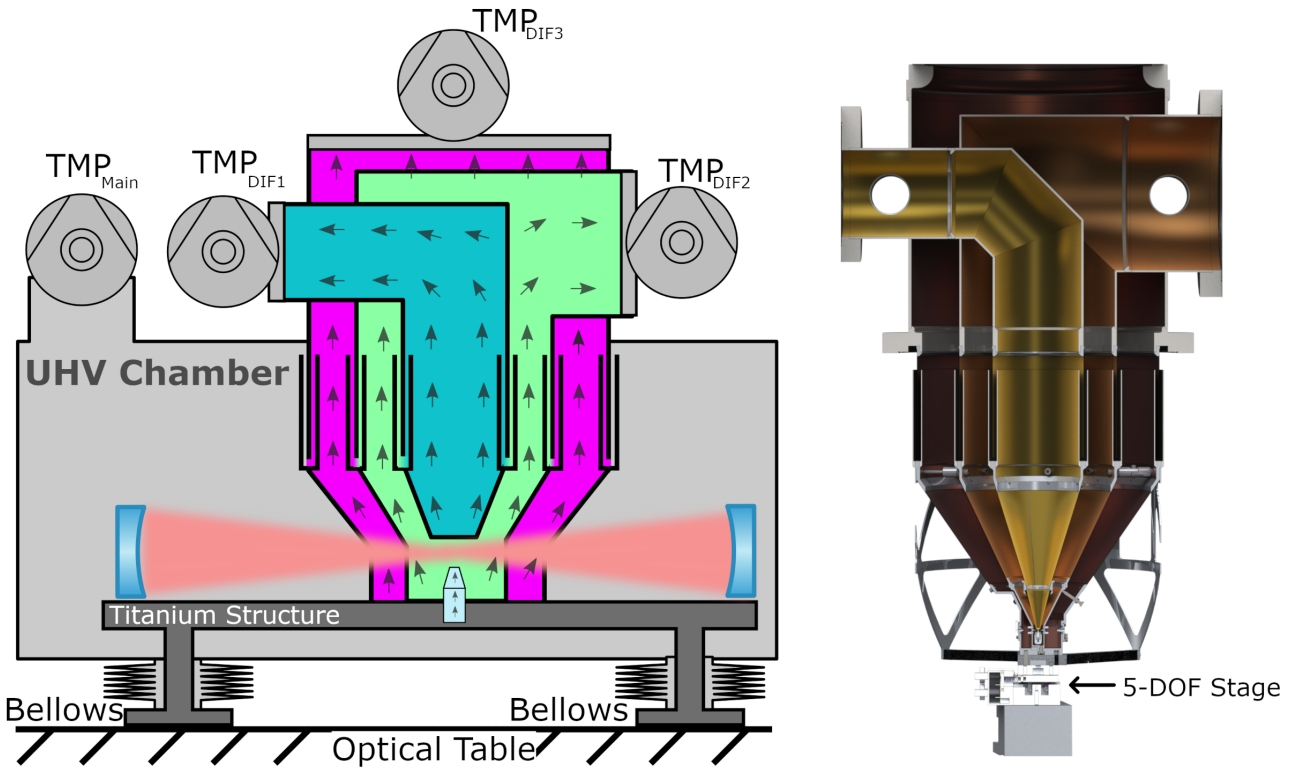

Figure 3.4.: (Left) Schematic of the vacuum system including the differential pumping system which is decoupled from the chamber by interlacing non-touching metal shields. The different Turbomolecularpumps (TMP) are shown with their nomenclature used in the text. A cross section of the final assembly is shown on the right.

stages mounted on a 5-axis stage for alignment, with further details discussed in the subsequent chapter.

High harmonics are generated in the gas jet and are coupled out of the cavity using a grating-mirror, a high reflective rectangular NIR mirror with a grating structure etched into it [73]. This mirror reflects longer-wavelength infrared light while diffracting XUV light. Small nozzles positioned in front of the grating and subsequent curved mirror emit ozone to remove surface contamination [74].

To ensure stable cavity operation, the optics are mounted on a dedicated titanium structure, as depicted in Figure 3.2. Titanium was chosen for its reduced susceptibility to thermal expansion compared to other common materials such as stainless steel or aluminum while having a high tensile strength and relatively low weight. The approximately 900 kg weight ensures a very low natural frequency and faster decline of transmissibility for higher frequencies, reducing vibrations. The titanium structure is directly mounted on an optical table, while the surrounding vacuum chamber floats on air bellows (BiAir, Bilz Vibration Technology AG) to decouple turbomolecular pump vibrations from the optical table as depicted in Figure 3.4 [75]. This posed a challenge as the differential pumping system needed to be mounted onto the titanium structure to ensure precise alignment with the cavity laser mode, while the pumps needed to be mounted onto the floating chamber structure.

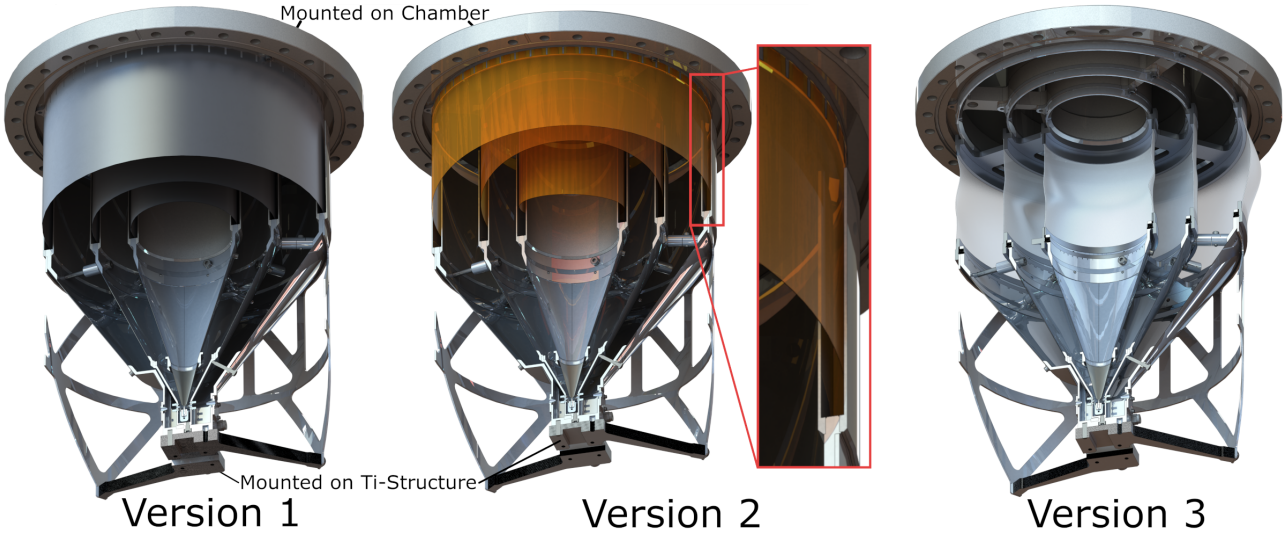

Figure 3.5.: The three versions of the differential pumping systems that are tested. With the original interlacing metal tubing based version V1 depicted on the left, a Kapton foil based version V2 and a non interlacing silicone sheet version V3. The inset on V2 shows the interlacing tubes in detail.

3.2. Differential Pumping System

The schematics of the differential pumping system are shown in Figure 3.4a, where the chamber is floating on air bellows while being decoupled from the optical table with membrane bellows. The nozzle is housed within an aluminum structure comprising of two nested chambers as illustrated in Figure 3.3. A hole is integrated into the structure to accommodate the laser and can accept skimmers to reduce gas flow from the different volumes. Typically, only the outermost skimmers between the main chamber and the outer volume of the differential system are utilized. An open cone positioned above the nozzle captures the primary gas load. Both the cone and the two chambers are evacuated by turbomolecular pumps, with the cone and inner chamber pumped by high gas load pumps (STPH-301C and STP-451, respectively).

Originally, the connection between the pumps and the nozzle housing is established using partially interlaced metal tubes, as depicted schematically in Figure 3.4a and the final construction in Figure 3.4b [32]. This setup utilized two 0.5 mm thick metal tubes separated by 2 mm to form a wall extending 100 mm upwards from the nozzle housing. A similar tube is inserted from the top into the gap and mounted onto the floating vacuum chamber. When perfectly aligned, the upper and lower parts have no contact, minimizing gas flow between them due to the long path-length and small cross-section created by the interlacing metal tubing. However, aligning these parts is challenging. If the two parts touch, the stage lacks the power to move the system, leading to difficulties in adjusting the focus area and potentially requiring venting the chamber to resolve. To address these challenges, the connection between the upper and lower part underwent two major iterations, as depicted in Figure 3.5:

Version 1: Metal Tubing
The original version utilized interlacing metal tubing as described. Detailed information can be found in [32].

Version 2: Kapton Tubing

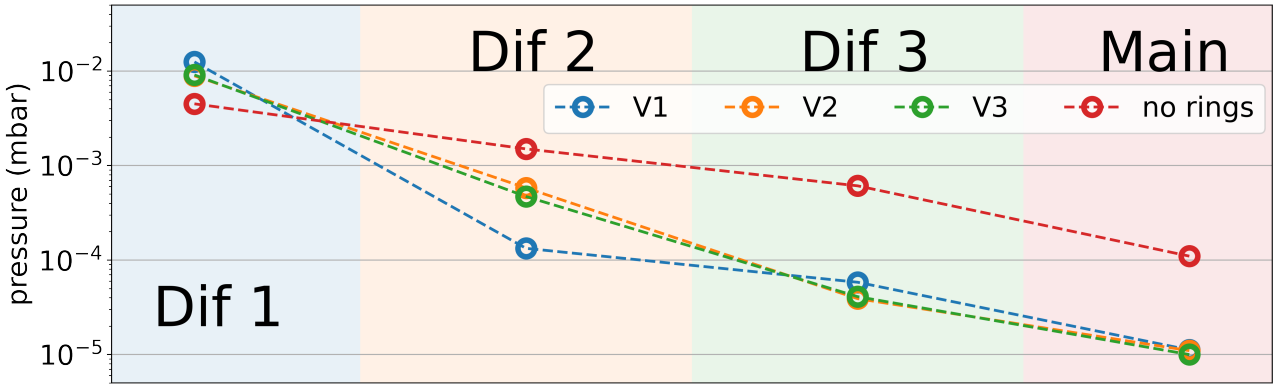

Figure 3.6.: The differential pumping performance of the different versions and a base measurement without any upper rings, leaving a 20 mm gap between the lower and upper assembly. Argon is injected with 8 bar of backing pressure through a 40 μm nozzle.

The second iteration replaces the upper aluminum rings with Kapton rings. These rings, cut at an angle for easier assembly, consists of 2 mm thick Kapton foil wrapped around the circular lip where the upper aluminum tubes of the previous designs were mounted. The higher flexibility of Kapton allows for greater misalignment tolerance before the two parts become stuck. Patches of copper tape are applied to the inside of the outermost ring to detect contact between the parts electrically. However, this version still experiences limitations in range and the potential to become stuck.

Version 3: Silicone Sleeves

The third iteration replaced the interlacing metal tubing concept with a single flexible connection. Circular adapter plates were machined to be placed into the lower and upper parts where the metal/Kapton tubing was previously mounted. These plates featured three circular rings connected by thin metal bridges to minimize pumping restrictions while allowing to mount the new structure without major disassembly of the original system. Silicone sheets were wrapped around the circular rings and joined together with small magnets. This version enabled the full range of motion of the stage, improving efficiency in aligning the gas jet with the laser.

The pumping performance of the different versions is similar and summarized in Figure 3.6, where a comparison is made with no upper rings installed at all. This results in a gap of around 20 mm between the lower and upper assembly and an order of magnitude worse pressure in the main chamber. This setup was utilized for the recycling measurements presented in the following subsection.

The third version allowed for the full range of motion of the stage, making finding the overlap of the laser with the gas jet more efficient. There are two ways to achieve this. One approach involves locking the cavity at high power and moving the nozzle around until plasma can be observed through a small window glued into the side of the nozzle housing. While this method can be performed without preparation and during system setup for an experiment, it is best suited when the overlap is known to be close. Scanning a wide range of nozzle positions becomes cumbersome due to hysteresis and the lack of referencing. The stage may eventually reach a position where a systematic scan becomes impossible, as the 5-axis do not move equally, introducing rotational and translational creep of the stage Furthermore, the lead screws are prone to become stuck when driven to the end of the range. For such cases, a second method is

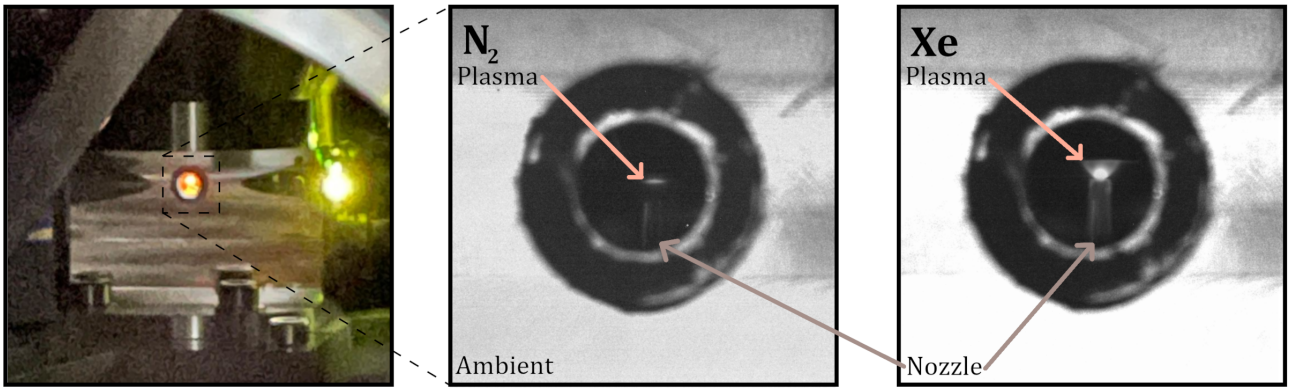

Figure 3.7.: Filling the chamber with 4 mbar of nitrogen produces a plasma at the laser focus inside the differential pumping enclosure. The middle inset shows a detailed view through the viewport of the housing, where the focus position is visible. After aligning the nozzle, a bright plasma is ignited when injecting xenon through the nozzle (right inset).

preferred, involving flooding the entire vacuum chamber with gas, igniting a plasma at the focus regardless of the nozzle position, and subsequently moving the nozzle, as depicted in Figure 3.7.

Previous attempts involved filling the entire chamber (approximately 0.5 m^3) to 10 mbar with xenon, which became rather expensive given the current xenon prices (14.00 EUR per Sl, April 2024). To reduce costs and expedite the operation, we tested molecular nitrogen for determining the focus position. Not only is nitrogen cheaper, but it is also available through in-house lines wired directly to our venting system. This saves time by eliminating the need to flood the chamber through the 100 μm diameter nozzle or rebuild the gas supply to the chamber. However, nitrogen has a higher ionization energy of 15.58 eV compared to xenon's 12.13 eV. Consequently, less ionization occurs for a given laser power. This can be compensated for by increasing the pressure inside the vacuum chamber. According to Paschen's law, the piezo used for length stabilization can be operated under any pressure with nitrogen without risking discharge that could potentially damage it, whereas with xenon the operating voltages of ~120 V start a discharge [76, 77]. We found the optimum pressure to be around 1-10 mbar, as higher pressures attenuated the beam in accordance with the Beer-Lambert law, and introduced dispersion decreasing enhancement.

3.3. HHG Generation Performance with Closed Loop Recycling of Xenon

To test the stability of the cavity and the XUV frequency comb, harmonics were generated on multiple occasions over a span of five days. This was done to assess the recycling efficiency of the gas recycling setup, where xenon used for HHG is captured, processed, recompressed, and reinjected. The entire recycling system, as well as its performance, is summarized in [78]. Here, we focus on the HHG performance under recycling conditions and long-term operation. It's important to note that the differential pumping system was under construction during this measurement and operated without the upper rings (see Figure 3.5), no ozone was injected.

A simplified schematic of the recycling system used for this measurement is shown in Figure 3.8. The exhaust of the turbomolecular pumps can be diverted to the roots pump (A100L, Pfeiffer

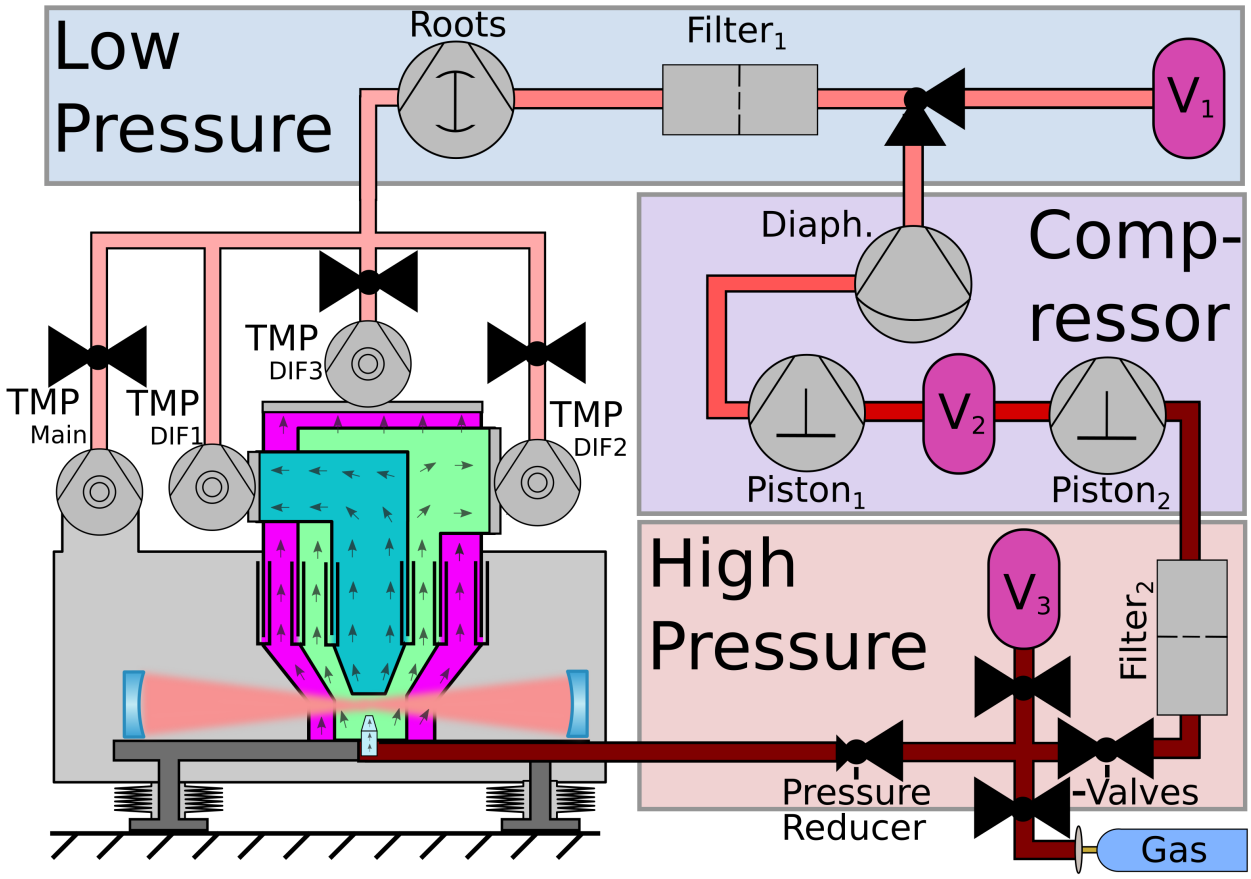

Figure 3.8.: Schematic of the gas recycling system, where the exhaust of the turbomolecular pumps (TMP) can be diverted into the recycling system where a roots pump fills the low pressure site. After filtration, the gas can be stored in a storage volume (V1) or compressed in the compressor station, where a diaphragm pump and two piston compressors can compress the gas up to 200 bar. In the following high pressure site, the gas gets filtered and can be diverted to another storage volume (V3), rebottled or send back to the nozzle.

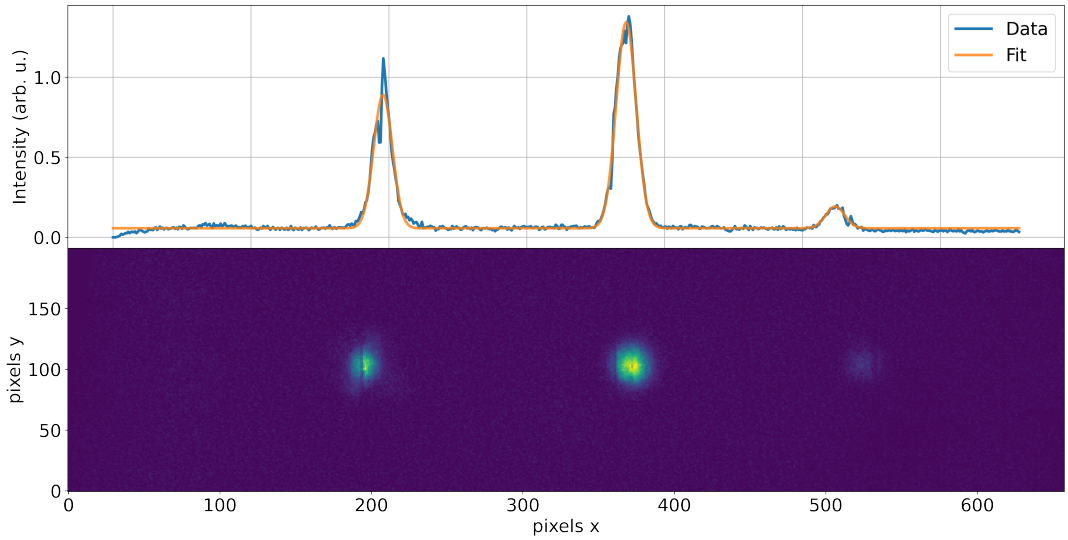

Figure 3.9.: Fluorescence signal of the 13$^{\text{th}}$, 15$^{\text{th}}$ and 17$^{\text{th}}$ harmonic on a sodium salicylate coated metal ruler, which is integrated along the y-axis. A Gaussian distribution is fitted to determine the fluorescence yield.

Vacuum Technology AG). Depending on the priority, either all turbopumps can be diverted for recycling to capture most of the gas inside the vacuum chamber, or only the innermost stage of the differential pumping system to minimize contamination with the ozone/oxygen misted onto the cavity mirrors. Since no ozone was used, the exhaust of all pumps was directed to the roots pumps. The roots pump can capture and compress gases up to 1 bar, feeding them into the low-pressure side. Here, the captured gas passes through particle and water filters. A switchable 20 liter tank can store the gas. To maximize round trips, the storage tank was disconnected for this measurement. Subsequently, the gas is sent to the compression stage. A diaphragm pump further compresses the gas further, allowing it to be fed into a two-stage compressor station. The compressor station can compress the gas up to 200 bar, enabling re-bottling of gases. For this measurement 25 bar was chosen. The pressurized gas is then diverted into the high-pressure side, where it undergoes another round of filtration and can either be stored in a tank, re-bottled, or sent back to the nozzle for closed-loop operation. Here, the gas bottle connection is used to prime the system initially, while the storage tank serves as a buffer to stabilize pressures.

To measure the intensities of the harmonics, a sodium salicylate-coated stainless steel edge was placed into the cavity, which fluoresces under ultraviolet radiation. A camera recorded images of the different harmonic orders through a viewport, as seen in Figure 3.9. The 13$^{\text{th}}$, 15$^{\text{th}}$, and 17$^{\text{th}}$ harmonics were chosen as they are of interest for future experiments (see Chapter 5). The images were background-corrected and integrated along the y-axis to retrieve intensity distributions. Gaussian fits were applied to determine the intensity of each harmonic. The steel edge features a ruler laser engraved onto it to determine the absolute positions of the harmonic orders, which coincides with the 15$^{\text{th}}$ harmonic, leading to a dip in the intensity distribution. During harmonic generation, the intracavity power was recorded by measuring the leakage with a photodiode.

The recycling system was purged with helium, which was injected into the low-pressure side

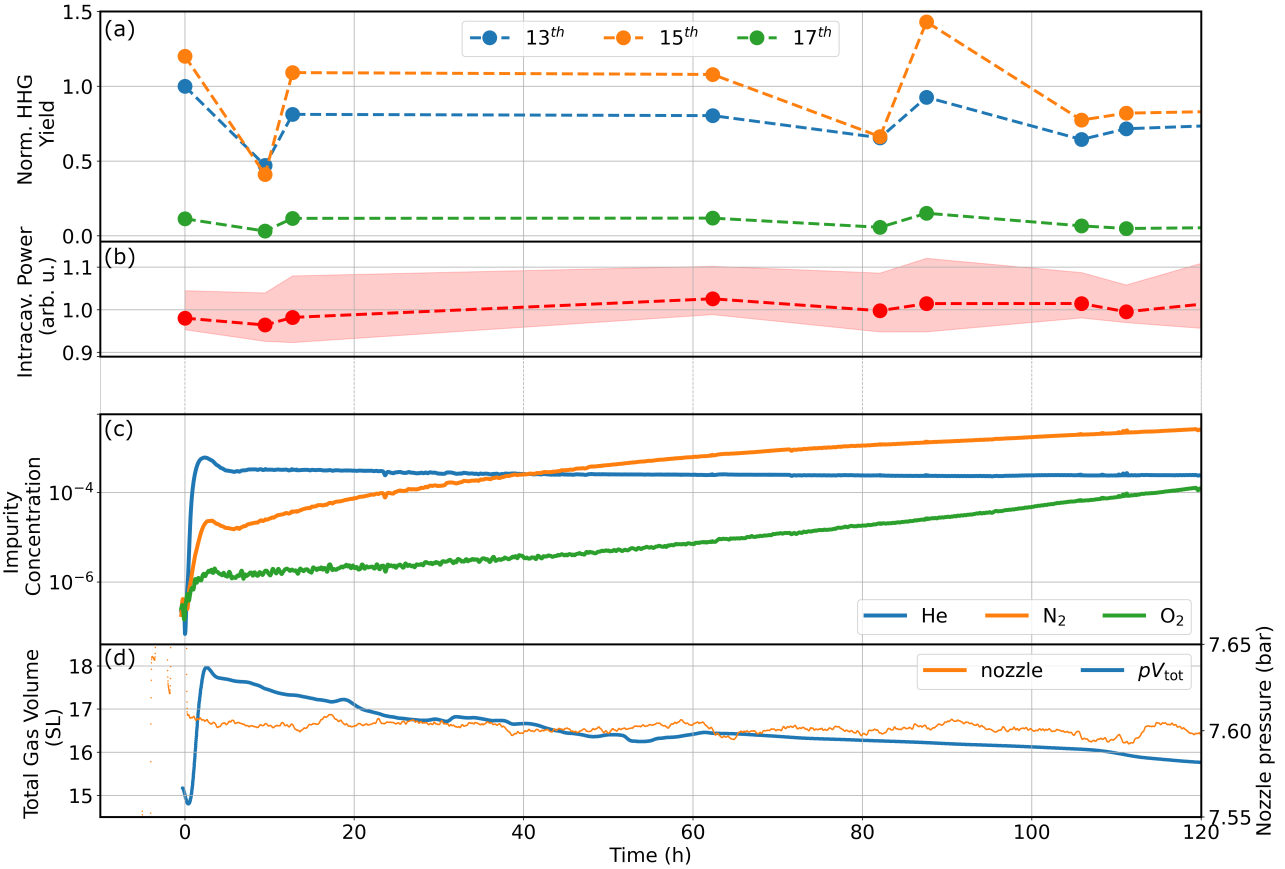

Figure 3.10.: (a) The harmonic yield normalized to the first 13$^{\text{th}}$ harmonic measurement and (b) the intracavity power during the generation with the shaded area showing the variance of the power. (c) The gas composition of the main chamber is recorded together with (d) the total gas volume in the recycling system and the nozzle pressure.

to efficiently pump any accumulated contaminations. Most of the helium is extracted after the pressure reducer before the nozzle. Small quantities of helium remain in the system, primarily in the compressor station due to installed check valves and the intermediate tank V_2. Since helium is used as a common additive to increase gas velocity for intracavity HHG, reducing plasma accumulation [79, 32], it is not hindering in the generation of high harmonics. Although the concentration is not significant, being under 40 ppm during operation.

At the start of the measurement, the system was filled with xenon 4.9 from a gas bottle attached to the low-pressure side. Xenon was accumulated in the low-pressure side until a total volume of around 19 SL was reached. Subsequently, the bottle was closed off, and the system was operated in a closed-cycle mode. With a nozzle backing pressure of 7.6 bar, the gas consumption was 1.45 SL/h, resulting in 10 round trips of xenon over a 120-hour measurement period. The gas composition was monitored with a residual gas analyzer (MKS) mounted into the main vacuum chamber.

The results are summarized in Figure 3.10, where the fluorescence yield of the 13$^{\text{th}}$, 15$^{\text{th}}$, and 17$^{\text{th}}$ harmonics is plotted against time normalized to the first measurement of the 13$^{\text{th}}$ harmonic. The power fluctuates over the measurement period, but there is no obvious trend indicating a correlation with xenon recycling. Since HHG is a highly nonlinear process, the yield strongly depends on intracavity power. When comparing it to the HHG yield, both seem

to follow a similar trend, especially the 17^{th} harmonic. To investigate this influence, Spearman's correlations were calculated and are summarized in Table 3.1. Due to the small sample size of our measurement, these values must be interpreted cautiously.

	13^{th}	15^{th}	17^{th}
Mean yield	0.753	0.923	0.085
Standard Deviation	0.16	0.3	0.04
RSD	0.21	0.33	0.48
Spearman's Correlations			
13^{th}	1.00	0.967	0.767
15^{th}	0.967	1.00	0.850
17^{th}	0.767	0.850	1.00
Laser Intensity	0.04	0.133	0.417
Intensity Variance	-0.1	0.033	0.15
Max Intensity	0.117	0.217	0.417
Gas impurities	-0.25	-0.133	-0.133
Linear dataset	-0.25	-0.133	-0.133

Table 3.1.: Correlations of the high harmonic yield with experimental parameters and to each other.

The results show a strong correlation between the 13th and 15th harmonics, while the 17th harmonic exhibits a significantly lower correlation with the other orders. This indicates that the 17th harmonic is influenced by different factors that lower the yield during our measurement. This is further supported by the moderate correlation of the 17th harmonic with laser intensity compared to the 13th and 15th harmonics. While gas impurities correlate with the 13th harmonic, a correlation with an artificial linear dataset demonstrates that a correlation of 25% is not conclusive. The non-linear nature of Spearman's correlation accounts for higher/lower orders, suggesting no clear polynomial behavior of the yield.

Hence, the recycling system allows to reduce the xenon consumption from 1.45 SL/h to 33,8 mSL/h while maintaining contamination to a non interfering level. For all following measurements utilizing HHG, the recycling system was used to keep operating costs down.

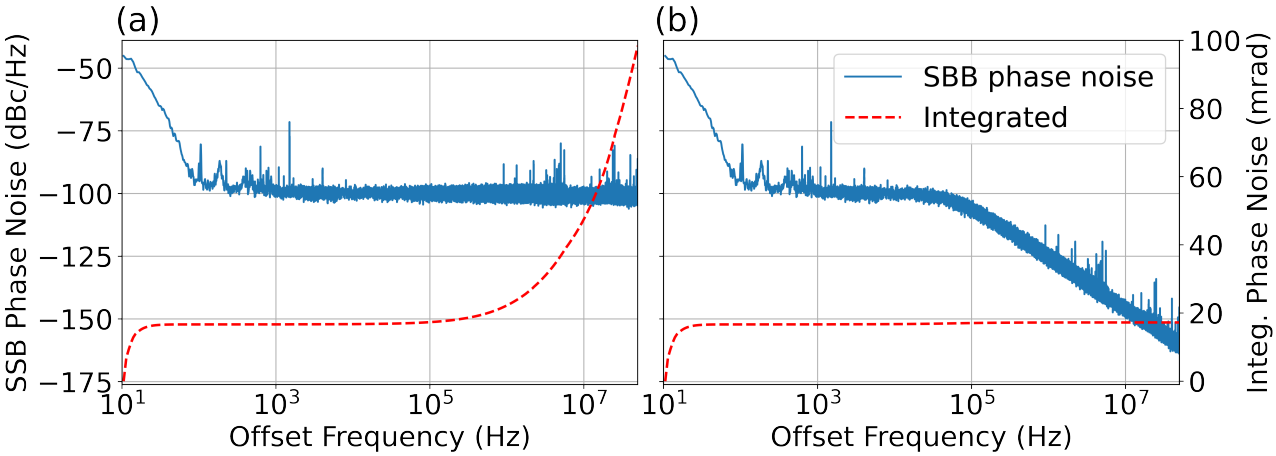

Figure 3.11.: Power spectrum of the frequency comb and the integrated phase noise of the NIR frequency comb (a) and after applying the transfer function of our enhancemet cavity (b).

3.3.1. Intensity and Phase Noise

To assess the short-term stability of the XUV frequency comb and the purity of the carrier frequencies, we estimated the phase noise. A straightforward method for estimating the noise involves recording the power spectrum of the frequency comb [80, 81]. To accomplish this, we measured the laser intensity before amplification using a 2 GHz bandwidth photodiode (Thorlabs Inc. DET025A) and recorded the spectrum with an oscilloscope (R&S MXO44). The noise spectrum exhibited distinct peaks (Figure 3.11a, blue line), which can be attributed to vibrations and electrical feedback noise for lower and higher frequencies, respectively. Integrating over the frequencies from 10 Hz to 50 MHz (Figure 3.11a, red dashed line) yields an integrated phase noise $\Delta\Phi_{\text{rad}}$ of 135 mrad for the NIR comb. According to $\exp(-\Delta\Phi_{\text{rad}}^2 q^2)$ [82], the comb tooth contains 98.2% of the power fraction in the fundamental harmonic ($q = 1$). Due to the quadratic behavior of the carrier power fraction with the harmonic order q, transferring the comb into the XUV can lead to a carrier collapse, leaving only 4.5% of the power in the carrier for the 13^{th} harmonic.

Since the harmonics are generated in an enhancement cavity, frequencies above the cavity's linewidth are attenuated [83], as depicted in Figure 3.11b.

To determine the linewidth, we recorded the ringdown of the cavity, as shown in Figure 3.12. The resonator was slowly scanned to bring it into resonance while an EOM shifted the laser frequency to drive the laser off resonance momentarily. Exponential fits were applied to the transmitted and reflected light to determine the decay times of $\tau_{\text{refl}} = (1.280 \pm 0.005)\,\mu s$ and $\tau_{\text{trans}} = (1.462 \pm 0.015)\,\mu s$, respectively. Two sets of measurements revealed a systematic shift in the decay time between the transmitted and reflected light. A weighted average was computed to determine the finesse $\mathcal{F}$ according to

$$\mathcal{F} = \frac{\Delta_{FSR}}{\Delta\lambda} \tag{3.1a}$$

$$\Delta_{FSR} = \frac{c}{L} \tag{3.1b}$$

$$\mathcal{F} = 2\pi\tau_{\text{cav}}\Delta_{FSR}\,, \tag{3.1c}$$

where the definition of the finesse relates the free spectral range Δ_{FSR} of a cavity to the

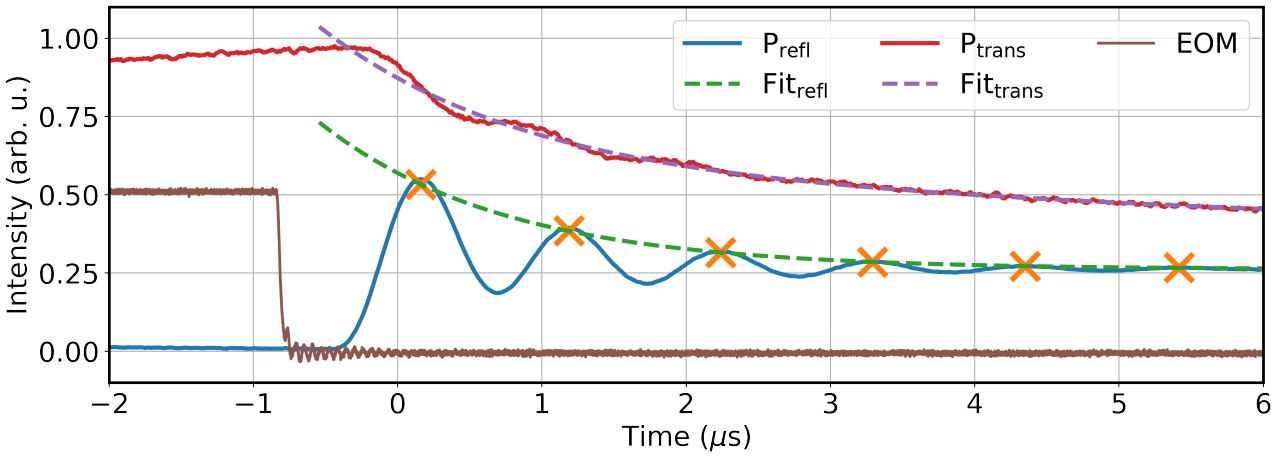

Figure 3.12.: Ring down measurement of the cavity with the EOM voltage shown that momentarily shifts the laser of resonance with the cavity and the decay of the transmitted and reflected light of the cavity.

spectral bandwidth $\Delta\lambda$. The resulting finesse of the enhancement cavity is $\mathcal{F} = 884 \pm 50$, corresponding to a bandwidth of 113 ± 6 kHz. Accounting for this, the noise spectrum is filtered, resulting in a reduced integrated phase noise of 17.2 mrad, with the carrier containing 95% of the power at the 13^{th} harmonic. This measurement allows to compare the theoretical predicted noise to the noise of the light transmitted through the cavity. Influences of the locking feedback can be identified and improved upon. Furthermore, using a fast XUV photodiode can be used to directly measure the power spectral density of the harmonics. Comparison to the predicted noise spectrum allows to identify noise sources. Due to the shorter wavelength of the harmonics, they are more sensitive to path length variations that can originate from mechanical vibrations. Hence, it is important to verify the mechanical stability of the optics and beamline for the XUV frequency comb.

4. | Velocity-Map Imaging Spectrometer

This chapter introduces the new VMI spectrometer designed for studies with the XUV frequency comb. The requirements of the spectrometer are given by the planned experiments. One one hand, low energy electrons originating from neighboring Rydberg states have to be resolved. When ionized by an infrared laser, an energy resolution of 0.02 eV is required for electrons with a kinetic energy of up to 1 eV. On the other hand, as the XUV comb produces harmonics up to the 35^{rd} order, corresponding to a photon energy of 41.77 eV, high energy electrons have to be measurable as well. This requires the spectrometer to handle high voltages. Given the wide range of energies to be probed and the energy resolution required, the concepts to achieve these goals will be presented, including a numerical evaluation based on electron trajectory simulations. Afterwards, the design of the atomic beamline is presented, delivering a cold gas target for spectroscopy.

4.1. Spectrometer Design Considerations

The first realization of a VMI spectrometer by Eppink and Parker [47] was achieved using an electric field formed by extractor and repeller ring electrodes, imaging charged particles onto a position-sensitive sensor. Alongside a grounded exit electrode, this electric field forms an electrostatic lens as illustrated in Figure 4.1a. This lens focuses charged particles with the same transversal velocity vector from within a finite ionization region onto the same position on the detector. Subsequent VMI spectrometer designs have been introduced to achieve ever higher resolutions, to image higher energy particles, or to integrate the setup seamlessly into the given experimental scheme. The concepts we focus on include a carefully shaped electrostatic lens, incorporating a Sikler lens, while also shielding against stray fields and maintaining compactness to fit within the experimental vacuum chamber.

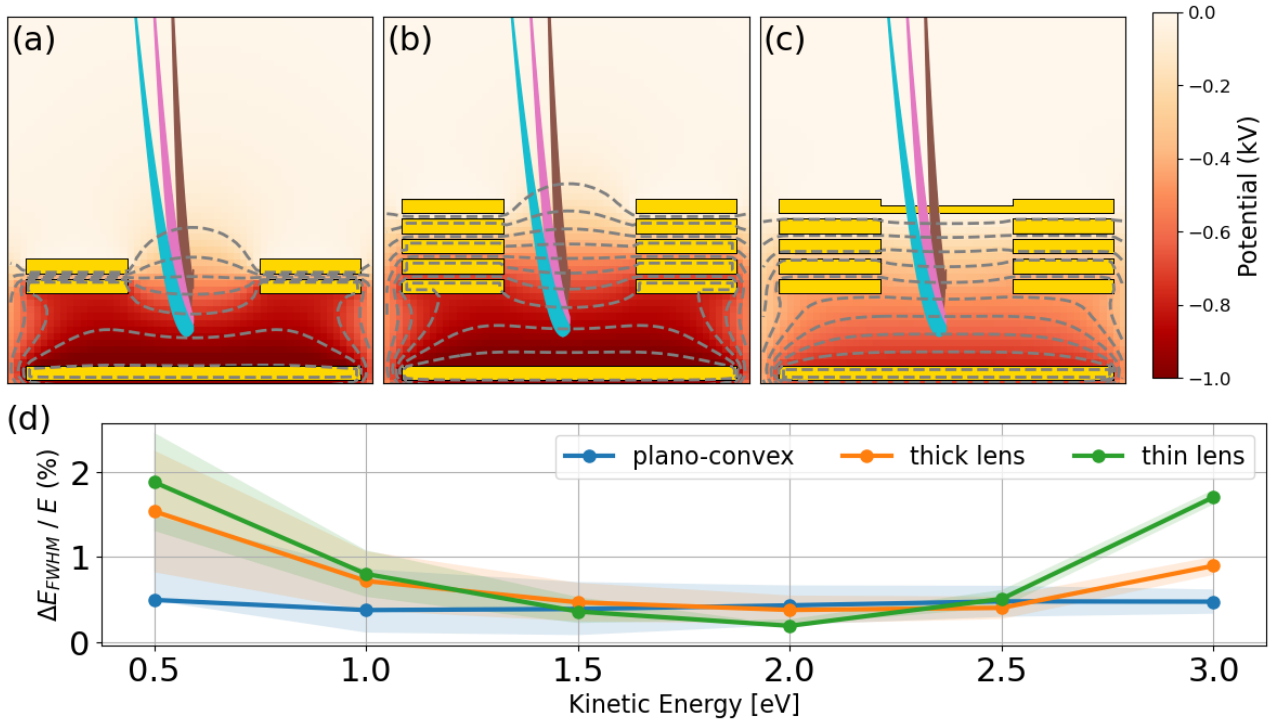

Figure 4.1.: Comparison of three lens designs: (a) a thin lens, (b) a thick lens and (c) a thick plano-convex lens. With exemplary electron trajectories for different transversal momenta depicted in turqois, pink and brown. (d) The energy resolutions are determined for the three designs. The bands show the change of the energy resolution for a 1 % voltage change.

4.1.1. Electron Optics

Numerous approaches have been developed to minimize aberrations when imaging the charged particles onto the detector. Some of these include using an additional einzel lens [84, 85], employing an opposite polarity lens between the repeller and the ground electrode to act as an achromatic lens [86], utilizing thick lenses [87, 88], plano-convex lenses [89], and shaping the extraction field according to analytical calculations [90], among others.

To evaluate the performance of a thin bi-convex, a thick bi-convex and a thick plano-convex lens, electrons are numerically propagated through three electrode configurations using SIMION (Version 8.1), as depicted in Figure 4.1a-c. An ionization volume in the shape of an ellipsoid with a full width at half maximum (FWHM) of 1 mm and 40 μm in the transversal and axial directions, respectively, is chosen. This is in accordance to the expected ionization volume given by the laser impeding an atomic beam. Each electron is randomly assigned a momentum vector, with the transversal component having a fixed value while the axial component is chosen such that the total momentum vector magnitude $|\mathbf{p}_{\text{tot}}|$ does not exceed 3 eV. This is done for transversal energies from 0.5 eV to 3 eV in steps of 0.5 eV. The spatial distribution of the electrons is recorded and evaluated at the detection plane and the resulting FWHM is used to determine the energy resolutions, enabling a comparison of the performance of the three lenses.

The voltages are optimized for a transverse kinetic energy of 2 eV and varied by 1 % to visualize the sensitivity of the energy resolution to electrode voltage deviations. Since the plano-convex lens has a different focal length than an equivalent bi-convex lens, all voltages are scaled accordingly. The resulting energy resolution is depicted in Figure 4.1d, showing the

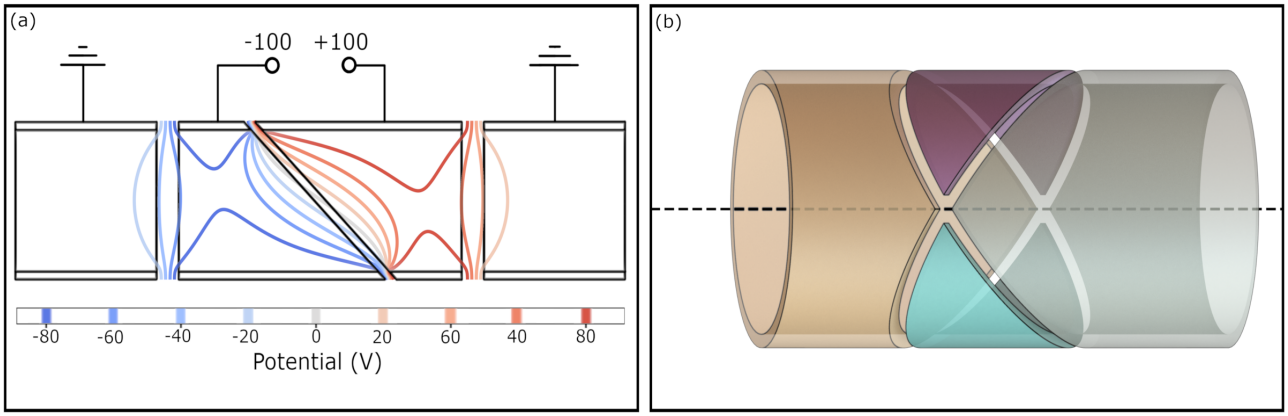

Figure 4.2.: (a) A cross section of a Sikler lens with one diagonal cut of the middle einzellens electrode and the resulting potential that allows to steer and focus charged particles. (b) The resulting electrode geometry of the middle electrode when segmenting twice with a 90° offset (Note the optical illusion of a 180° offset).

curvature of the energy resolution flattens when using a thick lens compared to the thin lens, and it can be further flattened using a plano-convex lens. Given the relatively constant energy resolution, the thick plano-convex lens is the most suitable configuration for us given the wide energy range of our experiment. However, this comes at the cost of the maximal achievable resolution [89]. **Sikler lens:**

A Sikler lens serves the purpose of tuning the dispersion and steering the electrons [91]. This capability proves useful for disrupting the rotational symmetry of the spectrometer system or gating the photoelectrons. By doing so, it becomes possible to image a specific region of interest across the entire detector or to sample the ionization mechanism as will be investigated in Section 5.1.1.

The Sikler lens is formed by cutting the middle lens of a classical three electrode einzellens diagonally as illustrated in Figure 4.2a. This allows to apply a steering potential given by the voltage difference across the now divided electrodes. Additionally, the focusing capabilities are retained and defined by the average potential of the split electrodes to the adjacent electrodes. Adding another segmentation offset by 90° allows to steer the electrons in the other spatial coordinate and introduce astigmatic focusing as depicted in Figure 4.2b. This geometry combines steering and focusing in a compact size, rendering it ideal for implementation into the VMI spectrometer.

Shielding:

Ensuring proper shielding against stray electric and magnetic fields is crucial to avoid imaging deformations, particularly when studying low-energy electrons. It is essential to suppress any magnetic fields, which is possible by enclosing the entire spectrometer in μ-metal shielding [92, 88]. Additionally, ferromagnetic materials have to be avoided for the construction of electrodes and parts that are inside the shielding. Furthermore, designing the electrodes in a way that prevents surface charges from accumulating on insulators helps avoiding the build up of stray electric fields. The most straight-forward way is the obstruction of any line-of-sight from inside the spectrometer to any insulating material.

4.2. The Velocity-Map Imaging Spectrometer

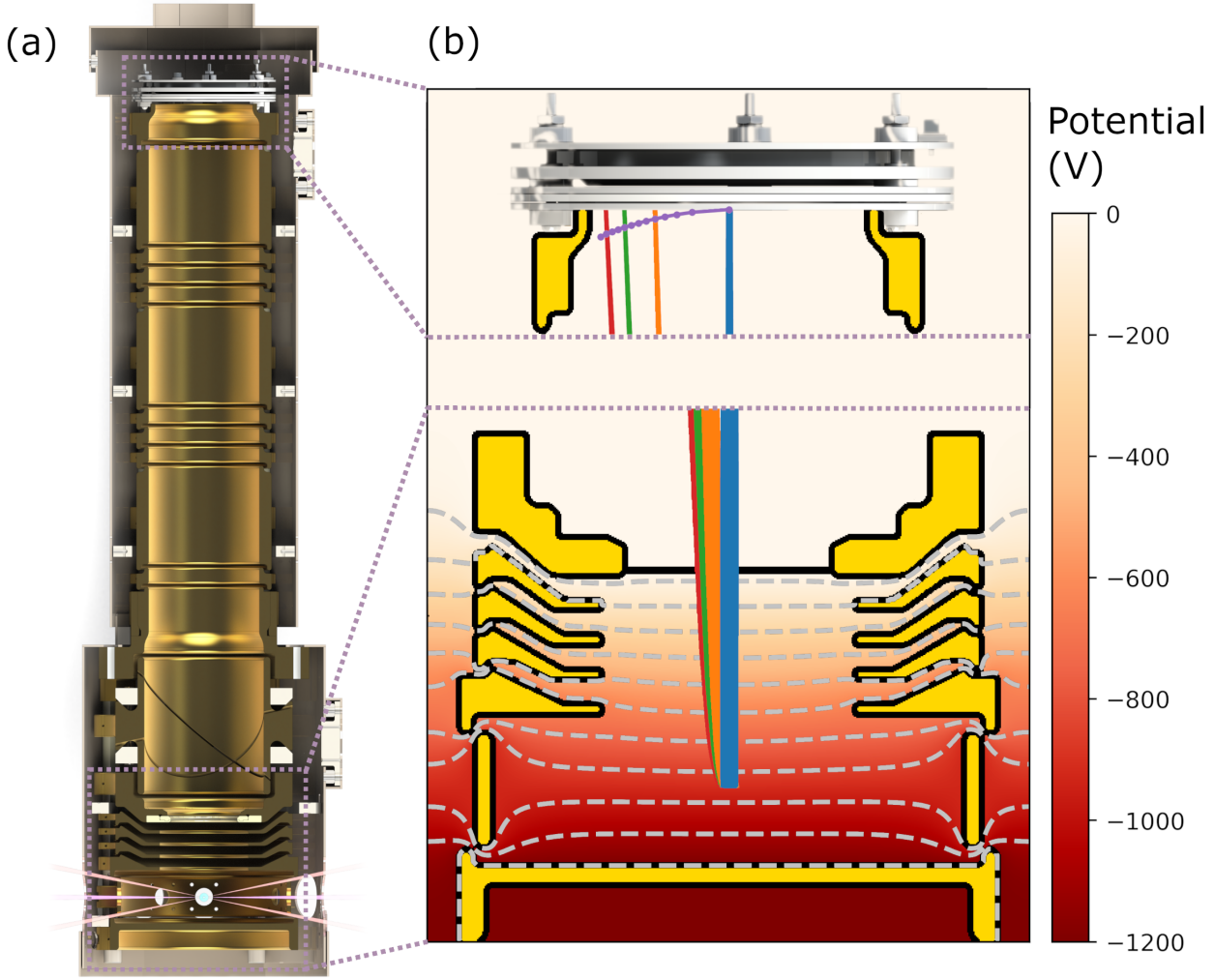

Figure 4.3.: (a) Final design of the VMI spectrometer with a cross-section view and (b) the potential formed by the thick plano-convex extractor lens as used to simulated the electron trajectories. Trajectories for electrons with 0 eV (blue), 1 eV (orange), 2 eV (green) and 2.5 eV (red) initial transversal kinetic energy are shown together with the location of the foci (purple line). The ionization volume is given by an ellipsoid with a major axis of 1 mm and minor axis diameter of 0.1 mm, centered in the lower section.

Given the aforementioned design considerations, the spectrometer is constructed to fit within the spatial constraints of the already existing vacuum chamber, where it is mounted on a CF100 flange. The spectrometer is oriented horizontally in order to align the detector parallel to the s-polarization of the XUV light. This enables the use of the Abel inversion to reconstruct the photo-electron momentum distributions from their 2D projections onto the detector. From an engineering perspective, this orientation necessitates constructing the VMI setup to withstand the bending moments inherent in such amounting geometry. For that, the electrodes are fabricated out of aluminum to minimize weight ($\sim$ 2.5 kg total weight) while remaining machinable to stringent tolerances. The weight distribution ensures that the mounting occurs close to the center of mass. However, aluminum surfaces oxidize, creating an heterogeneous non-conductive

layer. To mitigate this issue, the electrodes are tolerated to be electroplated with a copper layer on which a subsequent silver and gold layer are added to improve surface conductivity. Prior to electroplating, the spectrometer is tested using the bare aluminum electrodes coated with graphite (refer to Figure 4.4).

To accommodate the mounting of the electrodes into the experimental chamber, the spectrometer had to be divided into two parts. The lower part comprises the repeller, extractor, and the Sikler lens, which have a diameter larger than the CF100 flange. The upper part consists of the flight tube, consisting of seven thin and three thick ring electrodes to produce additional electrostatic lenses if needed, and the round MCP (P/n 40906, PHOTONIS Scientific, Inc.) with an active area diameter of 40 mm. These two parts are joined by a thread machined onto an electrode, as depicted in Figure 4.4c.

In both sections, the electrodes are mounted on four alumina rods, with a diameter of 8 mm for the lower part and 6 mm for the upper part, serving as a frame onto which the electrodes are mounted, thereby electrically insulating them from each other. This setup allows for safe operation of the electrodes up to 10 kV. The distance between adjacent electrodes is fixed by cylindrical MACOR spacers placed over the alumina rods. The first and last electrode of each stack are clamped to the alumina rods, securing the entire electrode stack in place. For the lower part, the ring electrode between the repeller and extractor is equipped with a clamping mechanism as well, allowing the repeller to be changed without disassembling the stack. This also allows to change to repeller to electrodes with integrated capillaries, holes for an axial atomic beam, etc. depending on the experimental needs.

To minimize charge buildup at the alumina rods, the electrodes are machined with a rim, obstructing any line of sight from inside the spectrometer to any insulator, captured in Fig. 4.4b. Additionally, the ring electrode between repeller and extractor allows for the mounting of targets into the spectrometer (e.g., capillaries, solid-state targets). PEEK brackets organize the wiring and reduce the risk of short circuits, particularly after enclosure with the μ-metal shielding.

The extractor setup is designed as a plano-convex thick lens with five ring electrodes, with the last one featuring a copper mesh, forming the imaging lens with an aperture diameter of 40 mm, consistent with the MCP's active area diameter. The thickness of the lens is chosen to be as large as possible while still allowing sufficient space for the Sikler lens. This configuration results in a 350 mm long time-of-flight (ToF) section from the mesh to the MCP.

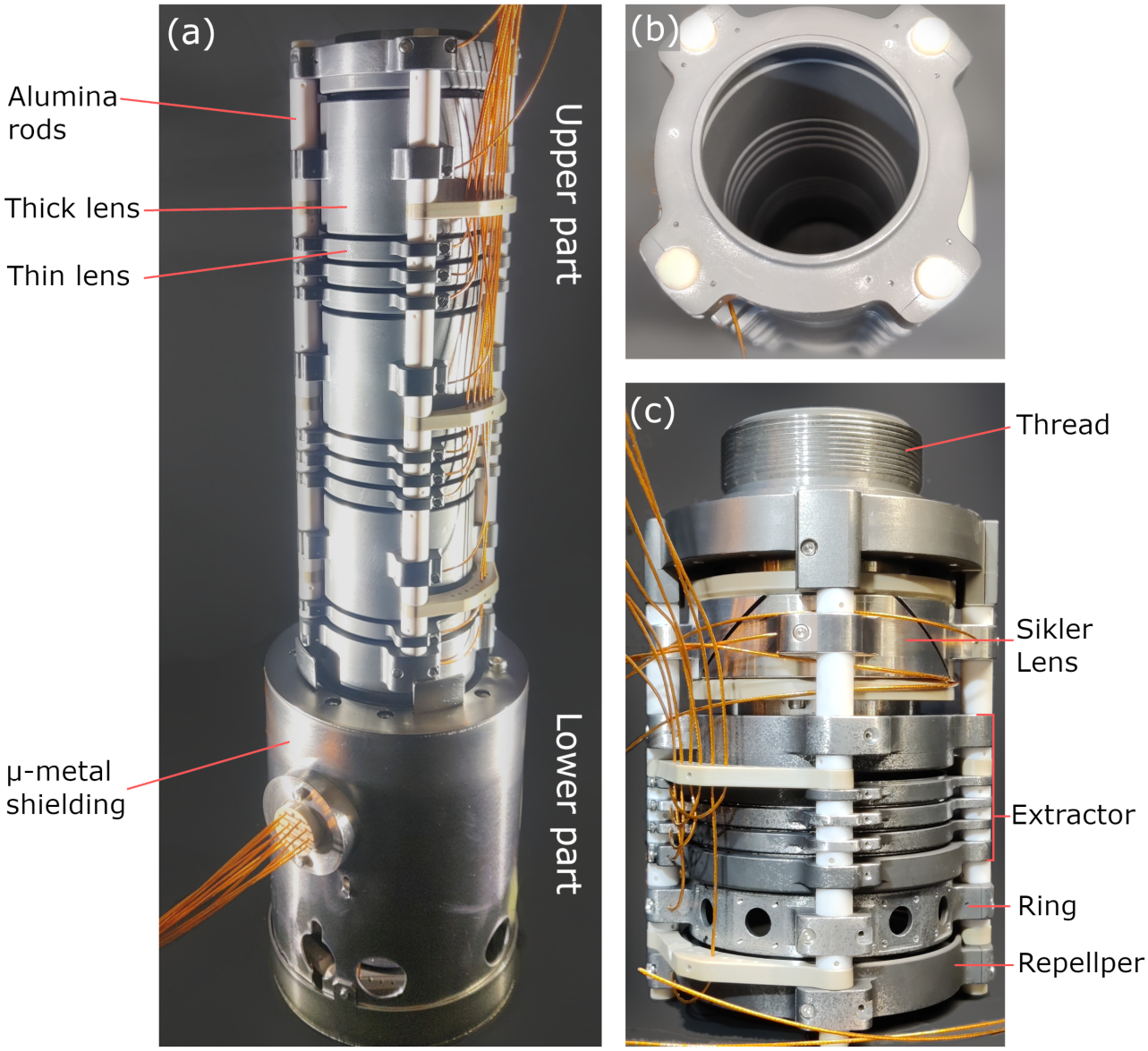

Figure 4.4.: Pictures of the assembled VMI spectrometer (a) before final enclosure in the μ-metal shielding of the upper part. And detail views of the upper and lower part in (b) and (c), respectively.

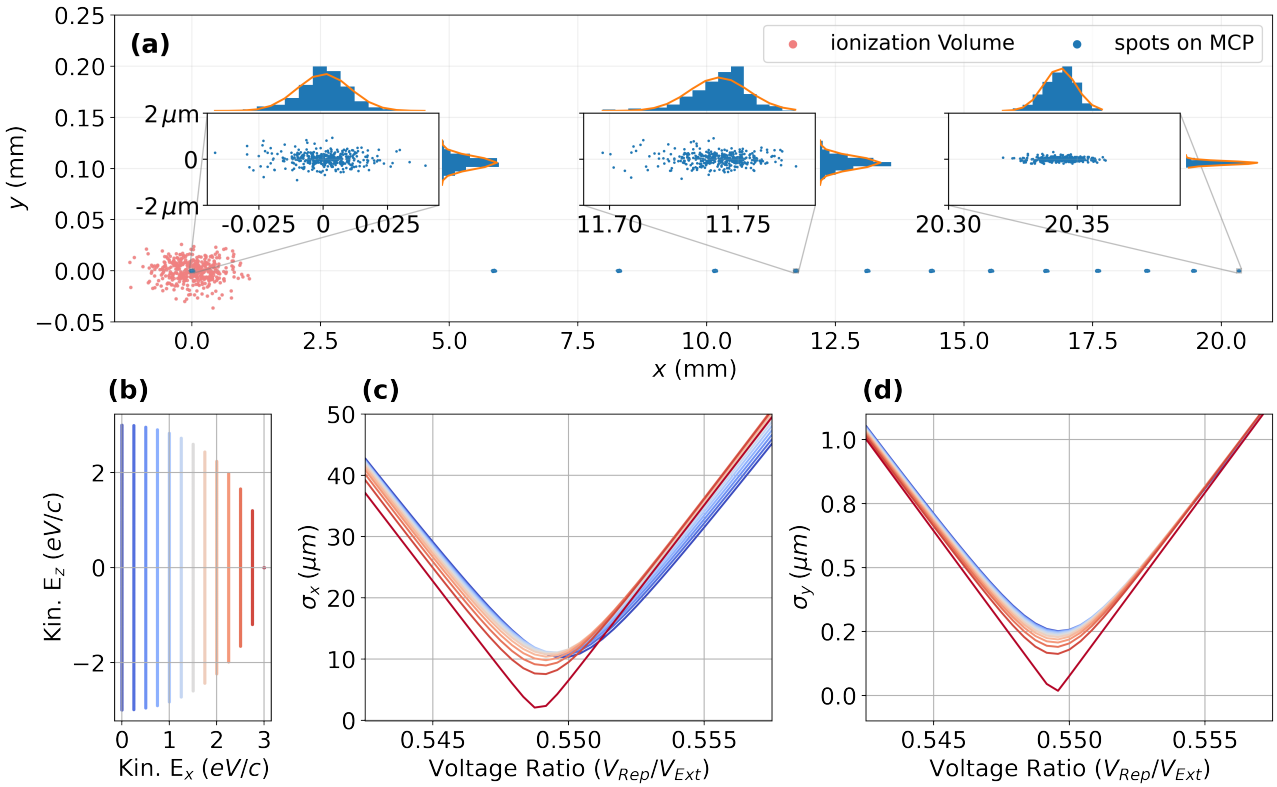

Figure 4.5.: (a) The initial electron distribution (red) in the source region and the final distribution (blue) at the detector plane, note the different scales in the x and y direction. Gaussian profiles are fitted to quantize the electron spread (orange). (b) The initial electron kinetic energy distribution used for the simulations (with the x-axis being the tangential direction and the y-axis the axial). The colors are used in (c) and (d), which show the electron spread at the detector plane in x and y direction for a set of extractor-to-repeller voltage ratios, with a fixed repeller voltage of -1.2 kV.

4.2.1. Simulations

To assess the imaging performance of the VMI spectrometer design, numerical electron trajectory simulations were conducted using SIMION (Version 8.1). An ellipsoidal ionization volume was chosen to match the expected ionization volume given by the laser focus, with a major axis diameter of 1 mm and a minor axis diameter of 0.1 mm. Due to the rotational symmetry, the electron momentum was distributed only along one transversal axis and along the spectrometer axis (here the x-axis and z-axis, respectively). Thirteen discrete equidistant kinetic energy classes between 0 eV and 3 eV are selected for the transversal component, while the axial momentum component varies continuously between $\pm p_{z,\mathrm{max}} = [3\,\mathrm{eV/c}^2 - p_x^2]^{1/2}$. This ensures that the total kinetic energy does not exceed 3 eV (see Fig. 4.5b). Consequently, for a transversal energy of 3 eV, there is no axial momentum component serving as a reference, as will be discussed later.

The final electron distribution at the detector plane was quantified by fitting Gaussians to the projections in radial and azimuthal directions. The extractor voltage was adjusted for a given repeller voltage of -1.2 kV, with a uniform drop across the five lenses with the mesh being grounded. The final electron spread was recorded, as seen in Figure 4.5a, and a voltage ratio of V_{ext}/V_{rep}=0.55 for VMI conditions is determined. Due to the long focal length, spherical aberrations minimally affect the imaging. The focus positions are located on a sphere with radius of curvature 51.6 mm, locating the outermost focus 4.3 mm in front of the detector (see

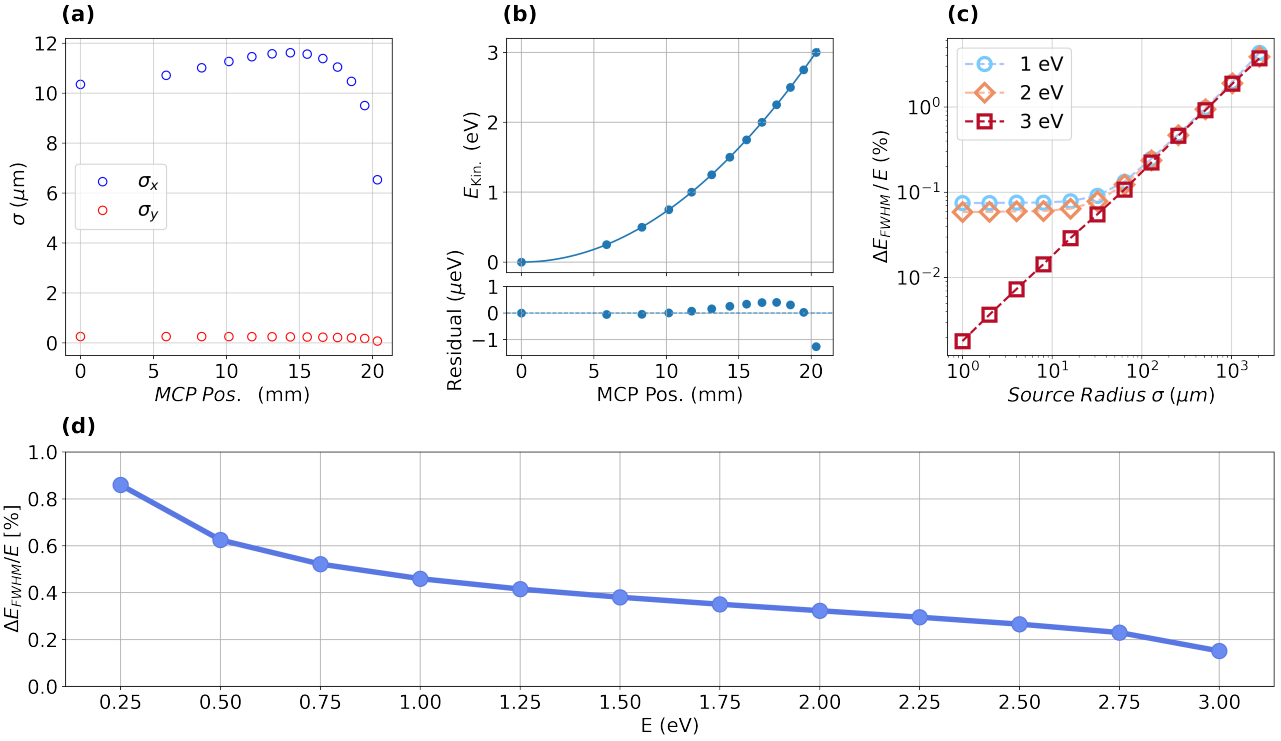

Figure 4.6.: (a) The electron distribution spread for different radii at the detector plane. (b) The quadratic energy to radius dependence is investigated. (c) The energy resolution for different spherical ionization volumes is evaluated, with the 3 eV class showing no limit due to no axial momentum component. In (d), the FWHM energy resolution with the original ellipsoidal ionization volume for a voltage ratio of V_{Rep}/V_{Ext}=0.55 is depicted for transversal kinetic energies ranging from 0.25 to 3 eV.

Fig. 4.3, purple dots). The divergence is on the order of a few mrad, resulting in negligible defocusing at the detector plane.

Consequently, the FWHM energy resolution exhibits a relatively flat profile over the probed energy range, with an average resolution of 0.4 % and a maximum of 0.18 % for the outermost detector area. Importantly, the focus size for the electrons is smaller than the MCP pore size of 12 μm (see Figure 4.6a), ultimately limiting the theoretical resolution to around 0.4 %. Another indication of the imaging quality is the theoretical quadratic correlation between the radius of the imaged spots on the detector to the transverse energy, which deviates one part per mille at most for this setup. The dependence on the ionization volume in Figure 4.6(c) sums up the findings well, where spherical ionization volumes of different radii were propagated through the system. For a finite momentum component in axial direction the spectrometer can achieve resolutions of 0.1 % for ionization volumes up to a few tenths of μm. The electrons with 3 eV transversal momentum demonstrates that without axial momentum, the electrons can be focused more tightly. The resolution is therefore not limited when the ionization volume is reduced. In the end, the finite pore size of the MCP requires the ionization volume diameter to be kept under ~1 mm for best performance.

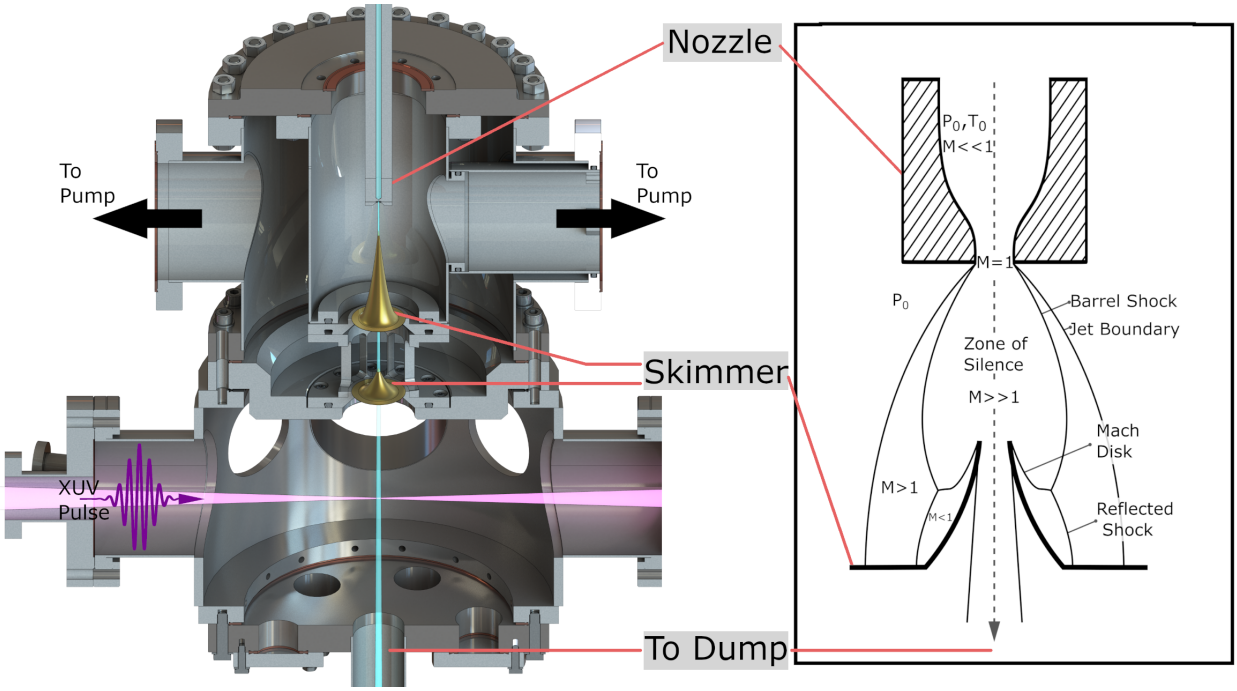

Figure 4.7.: The atomic beamline assembly (left) with the VMI spectrometer hidden for clarity. XUV pulses (purple) cross the atomic beam (turqouise) perpendicular to reduce the Doppler broadening. Two skimmers collimate the atomic beam, which is build with nested vacuum chambers to reduce overall size. The schematics of a supersonic beam with the underlying structures are shown in the right with the parameters described in the text.

4.3. Supersonic Atomic Beam

To achieve a small ionization volume and reduce the Doppler broadening, an atomic beam is designed. This atomic beam operates with a supersonic gas expansion through a nozzle, where the inner part is sampled by a skimmer. The key aspects of such supersonic expansions are illustrated in Figure 4.7 together with the final design of the apparatus. The defining parameter is the Mach number M, which represents the local ratio of the gas velocity to the speed of sound. As the speed of a supersonic expansion surpasses the speed of sound, information about upstream boundary conditions do not propagate upstream. This leads to the occurrence of shock waves, local areas with extreme pressures, densities, temperatures and velocity gradients. The resulting structures can be utilized to produce a cold atomic beam as the expanding gas cools adiabatically. In the following description we will use argon as the gas of interest. To analyze the target density and the optimum skimmer position, we have to calculate the local Mach number at a distance x/d, with the nozzle diameters d, using the polynomial approximation [93]

$$M = \left(\frac{x}{d}\right)^{(\gamma-1)} \left[C_1 + \frac{C_2}{\left(\frac{x}{d}\right)} + \frac{C_3}{\left(\frac{x}{d}\right)^2} + \frac{C_4}{\left(\frac{x}{d}\right)^3}\right] . \tag{4.1}$$

The constants C_i for gases with different isentropic expansion factors γ can be looked up in the Appendix A. Using the local M number, the temperature T, number density n_0 and the terminal velocity v_∞ can be determined by :

$$\frac{T}{T_0} = \left(1 + \frac{\gamma - 1}{2} M^2\right)^{-1} \tag{4.2}$$

$$\frac{n}{n_0} = \left(1 + \frac{\gamma - 1}{2} M^2\right)^{-1/(\gamma-1)} \tag{4.3}$$

$$v_\infty = \sqrt{\frac{2R}{W}\left(\frac{\gamma}{\gamma - 1}\right) T}\,. \tag{4.4}$$

With W being the atomic mass of the gas, T_0 and n_0 being the temperature and density of the gas before expansion, respectively, and R being the gas constant. To ascertain whether an isentropic continuum flow or a free molecular flow is present, the mean free path has to be compared to the physical length of the system (i.e. Knudsen number). The mean free path is calculated using the long-range attractive potential

$$\lambda_s = \left[5.3n \left(\frac{C_6}{k_\mathrm{B} T}\right)^{1/3}\right]^{-1}\,, \tag{4.5}$$

where the constant C_6 is looked up in a table (see Appendix A). For high background pressures P_b, this can be subsequently used to calculate the skimmer position for maximum mass throughput with following formula

$$\frac{x_s}{d} = 0.125 \left[\frac{d}{\lambda_s}\frac{P_0}{P_\mathrm{b}}\right]^{1/3}\,. \tag{4.6}$$

At this stage, the design of the atomic beamline has to be taken into consideration. Due to space constraints and the requirement for a clean vacuum environment, turbomolecular pumps (STPH 301C, Edwards Ltd.) are employed to pump the nozzle vacuum chamber. These pumps are specifically designed for high gas loads and offer $300\,\mathrm{ls}^{-1}$ of pumping speed for inlet pressures of up to $\sim 10^{-2}$ mbar. When they are water-cooled, continuous operation can be sustained for inlet pressures/backgroudn pressures of ~ 1 mbar. The correlation between the nozzle backing pressure and the vacuum chamber pressure can be estimated by

$$\hat{T} = \hat{S} P_\mathrm{b} = C \frac{T_c}{T_0} \sqrt{\frac{300}{T_0}} (P_0 d)\, d\,, \tag{4.7}$$

where $\hat{T}$ is the throughput, $\hat{S}$ the pumping speed, C a gas species dependent parameter (see Appendix A) and d the nozzle diameter given in cm. From that, the intensity I_s per second and steradian can be calculated from the initial intensity I_0 given by:

$$I_0 = \kappa F n_0 \left(2\frac{RT_0}{W}\right)^{1/2} \frac{d^2}{4} \tag{4.8}$$

with

$$I_\mathrm{s} = I_0\, q_1 \exp\left(-\frac{q_2 d_2}{\lambda_\mathrm{s}}\right). \tag{4.9}$$

The parameters κ and F can be looked up in Appendix A, while $q_1 \sim 1.38$ and $q_2 \sim 0.37$ are empirical values. We use a Skimmer with a diameter of $100\,\mu$m and a second skimmer with a $200\,\mu$m diameter placed 117 mm later to further decrease the spread. The acceptance of $8{\cdot}10^{-6}$ sr

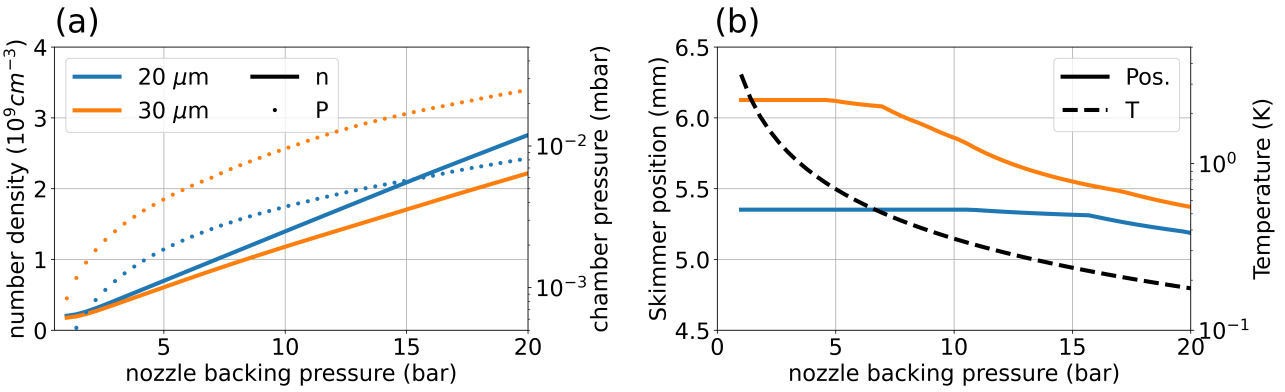

Figure 4.8.: (a)Calculated densities n in the spectroscopy region for different backing pressures with a 20 and a 30 μm nozzle and the resulting pressures P in the vacuum chamber of the nozzle (dotted lines). (b) Optimal distance of the first skimmer from the nozzle and the gas temperature after expansion which is independent of nozzle diameter (dashed line).

is considered when calculating the downstream particle density available for spectroscopy at the interaction zone. There, the atomic beam has a diameter of 1 mm and a density of $\sim 10^9\,\mathrm{cm}^{-3}$ as plotted in Figure 4.8 for different backing pressures for the available nozzle diameters of 20 and 30 μm. It is important to mention that with those backing pressures we are in a regime where the approximations made for Equation 4.9 are at the limit and hence a decrease of the particle density due to excess collisions at the skimmer have to be expected when using high backing pressures. Especially, the formation of dimers has to be accounted for, which is estimated to reach the per cent level at pressures above 10 bar. Nevertheless, the final temperature of the atoms will be around ~200 mK. To estimate the relative Doppler broadening $\Gamma_\mathrm{D}$we use [94]

$$\frac{\Gamma_\mathrm{D}}{\nu_0} = 2\frac{v}{c}\sqrt{\ln 2}\sin\epsilon\,, \tag{4.10}$$

which yields a relative broadening of $\sim 1\cdot 10^{-8}$ with a collimation factor ϵ of 0.0032. The velocity v of the atoms are approximated with Equation 4.4 to be $\sim 558\,\mathrm{m\,s}^{-1}$. For transitions using the 13^{th} harmonic at 15.5 eV, this yields a total Doppler broadening of ~ 37 MHz, which is narrower than the comb tooth spacing of 100 MHz. Since the velocity distribution in a supersonic beam is not Maxwellian, this is just a crude estimate.

5. | Spectroscopy of gas tagets with an XUV comb

In this chapter the first signal taken with the VMI spectrometer is presented. The shot-to-shot imaging manipulation with the Sikler lens is established and the implementations for future experiments investigated. Furthermore, the first VMI driven by an XUV frequency comb is presented. Finally, the implications of this experimental setup to conduct direct XUV frequency comb spectroscopy on a cold atomic beam of argon are examined.

5.1. Photoionization of Xenon

As a first test of our setup we choose to image photoelectrons from xenon due to the low ionization energy of 12.1298 eV [95]. Since the supersonic atomic beam is not yet operational, xenon was injected into the chamber through a needle valve up to a pressure of $1 \cdot 10^{-6}$ mbar ($\rho = 10^{10}\,\mathrm{cm}^{-3}$) which is the maximum operating pressure of the MCP. The XUV frequency comb was focused into the chamber through a differentially pumped beamline with a toroidal mirror for focusing [50]. A backwards propagating laser is used to align the everything. The power of the harmonics is measured with a photodiode (G1127, Hamamatsu Photonics K.K.) after the grating, mounted on a rotatable arm, such that a low order harmonic can be measured simultaneously to monitor the power. Additionally, before the installation of the VMI spectrometer, the power was also measured inside the experimental chamber which can be seen in Figure 5.1). The expected transmittance of the gold mirror used to select and steer the harmonics to the beamline together with the toroidal mirror is expected to be around 40 % [50]. However, the measured transmittance is around 0.1 % which can be attributed mainly to the toroidal mirror having a spot burned onto the surface as well as the unknown condition of the gold mirror used to select a harmonic.

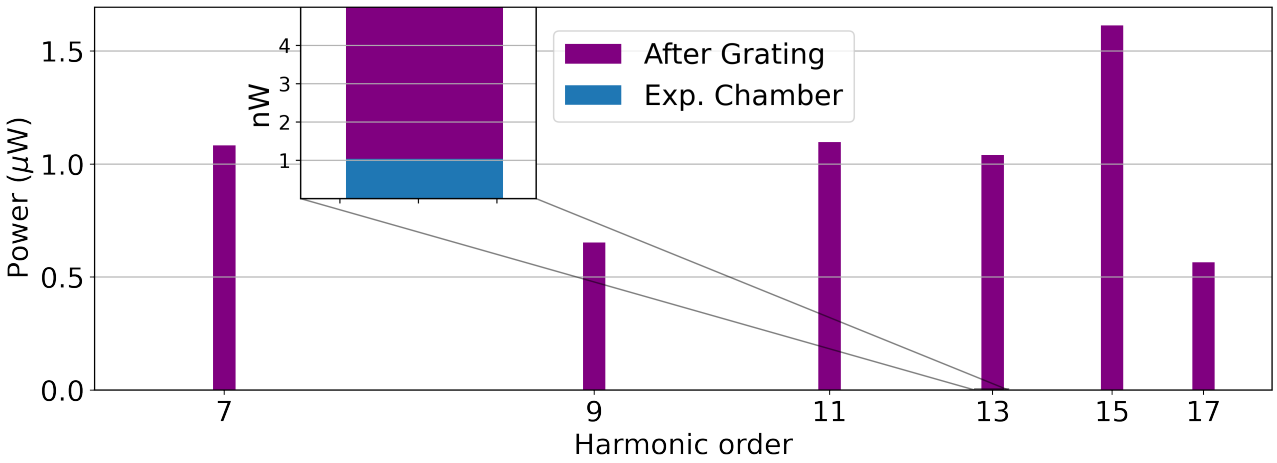

Figure 5.1.: XUV power measured after the grating and the fraction of the 13$^{\text{th}}$ Harmonic that is transmitted through the beamline into the experimental chamber.

With a total of 1 nW focused XUV available for experiments, the ionization rate can be calculated from the xenon ionization cross section σ of 58 Mb for our given photon energy of 15.5 eV [96]. We estimate the length l of the ionization volume that can be detected to be 20 mm, which yields an ionization rate of

$$R = \sigma \cdot \phi \cdot \rho \cdot l \approx 450\,\mathrm{s}^{-1}\,, \tag{5.1}$$

with ϕ being the photon flux. This is well above the dark count rate of 60 s^{-1} of the MCP.

5.1.1. Spatial Imaging with Shot-to-Shot Electron Manipulation

The VMI spectrometer can be operated in spatial imaging mode where for a different voltage ratio between the repeller and extractor (here $V_{\text{ext}}/V_{\text{rep}} = 0.995$) the spatial ionization distribution gets imaged onto the detector. This proves to be especially useful for alignment and characterization of the focus. As the cross section is independent of the intensity, the ionization volume by the XUV beam path.The expected divergence is with 9.25 mrad too small to be detected and with that the focus position. The resulting image for each setting in Figure 5.2, is acquired by integrating 3 sets of 9 pictures, each with an exposure of 0.8 s. The pictures are taken in sets to reduce the duty cycle of the cavity mitigating damage and deterioration. A signal to noise ratio (SNR) of 105 is achieved with the major noise source being the photoelectrons produced far off-axis.

To test the steering properties of the Sikler lens, a 50 MHz radio frequency (RF) is applied onto one of the electrodes as a steering signal. A function generator (SML01, R&S), referenced to the laser repetition rate of the NIR frequency comb, is amplified (HPA-25W-272+, Mini-Circuits) to produce up to 40 dBm of RF power. By changing the phase offset between the applied RF field and the repetition rate of the laser locked at 100 MHz, the deflection can be synchronized. For a 15 deg offset, the XUV pulse ionizes the xenon right when the steering potential crosses zero leaving the image ideally unchanged. As can be observed from the resulting image shown in Figure 5.2, the signal gets washed out due to imperfect synchronization, reducing the SNR to 71. Additionally, the steering axis of the Sikler lens is $\sim 30°$ rotated in respect to the ionization axis, illustrated with the orange dashed line in Figure 5.2. This leads to a reduced vertical deflection. Furthermore, imaging defects can be seen on the left-hand side which originate from

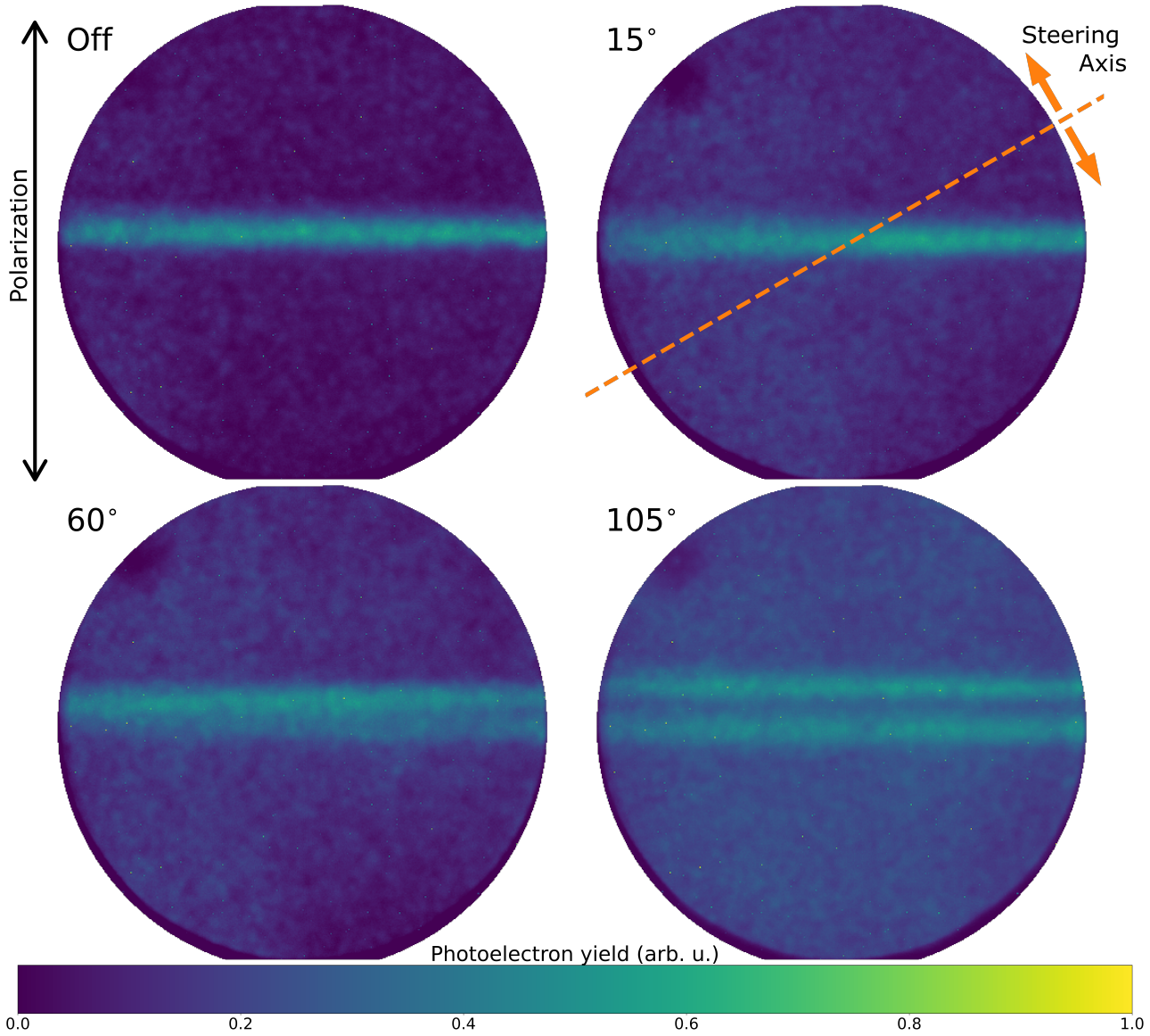

Figure 5.2.: Photoelectron distribution in spatial imaging mode without and with a 50 MHz RF applied to the Sikler lens for different phase offsets with the NIR frequency comb. The orange line depicts the steering axis of the Sikler lens which is offset by 30° with respect to the laser axis.

photo electrons produced far off-axis. While they would normally hit the walls of the electrodes, due to the deflection in the Sikler lens they can now reach the detector. Just as with geometrical optics, going through the imaging system far off-axis introduces aberrations.

Tuning the phase offset leads to a clear splitting of the electrons into two shifted images of the ionization volume, where the electrons get deflected on a shot-to-shot basis as seen for an offset of 105°. The XUV pulse ionizes the xenon right when the RF field peaks, deflecting the electron to one side. When the subsequent XUV pulse arrives the field changes polarity deflecting the photoelectrons to the other direction. As the electric field magnitude is highest as the XUV pulse arrives, electrons originating from further off-axis can make it to the detector, raising the background albeit not changing the SNR much, which stays around 70.

The control of the electrons on a shot-to-shot basis enables new experimental schemes expanding the applications. A few possible implementation are given as follows and illustrated in Figure 5.3a. First, the Sikler lens can be used as a 'pulse picker', discarding all but every n^{th} pulse by deviating the trajectory of the electrons out of of the spectrometer [97]. This is reducing the effective repetition rate allowing the detection of time of flight spectra, for example when imaging ions. Given their higher mass as compared to electrons, the 350 mm drift is sufficient to separate isotopes and dimers in time enough to distinguish them using a standard MCP with a phosphor screen. The MCP has a time resolution of ~ 10 ns (FWHM) when reading out the electric pulses from the screen. If position information is required as well, the time resolution is governed by the decay time of the P47 phosphor of 100 ns. For example, argon with a mass of 40 amu has the next stable isotope at a mass of 38 amu, leading to a Tof of 6.66 μs and 5.51 μs, respectively. The time difference of 150 ns is larger than the time between adjacent XUV pulses (10 ns), such that subsequent ionization events of the two isotopes can overlap in time. Hence, it is vital to extent the time between ionization events to be able to identify detector counts originating from dimers forming in the atomic beam, different isotopes etc.

The Sikler lens can also map subsequent ionization events onto different detector positions. By applying sinusoidal signals to the two deflection electrode pairs with a certain amplitude ratio and phase offset, the resulting detector picture can be described by the corresponding Lissajous curve. In Figure 5.3b the first curves are depicted, where the frequencies are chosen such that the electrons get sampled into five distinct spots. This is done in accordance to the CEO frequency range of the driving NIR comb. As the yield of the high harmonic generation exhibits a CEO phase dependence [98] for few-cycle pulses, amplitude modulation with exactly this frequency could be observed. Given the current work on temporal compression of our laser system [33] this amplitude modulation can be exploited to generate sidebands in the XUV, which is the frequency equivalent of an amplitude or phase modulation. Furthermore, other methods are possible to generate sidebands, like perturbing the free electron during the HHG process with a second color laser [99]. This is essential for the application of the XUV frequency comb for precision spectroscopy, especially to implement it in universal spectroscopic schemes like quantum logic spectroscopy [31]. Hence, the Sikler is a useful tool to detect the amplitude modulation, resolving the time axis by mapping it onto spatial coordinates.

Finally, breaking the rotational symmetry allows for novel operating modes of the VMI. As the rotational symmetry of a VMI spectrometer, images electrons with zero transversal kinetic energy onto the center of the detector. This sets a lower bound of the energy range probed. When an increased energy resolution for a certain region of interest is required, the whole image can be shifted using the Sikler lens such that only the region of interest will be mapped onto the detector while simultaneously adjusting the energy range imaged.

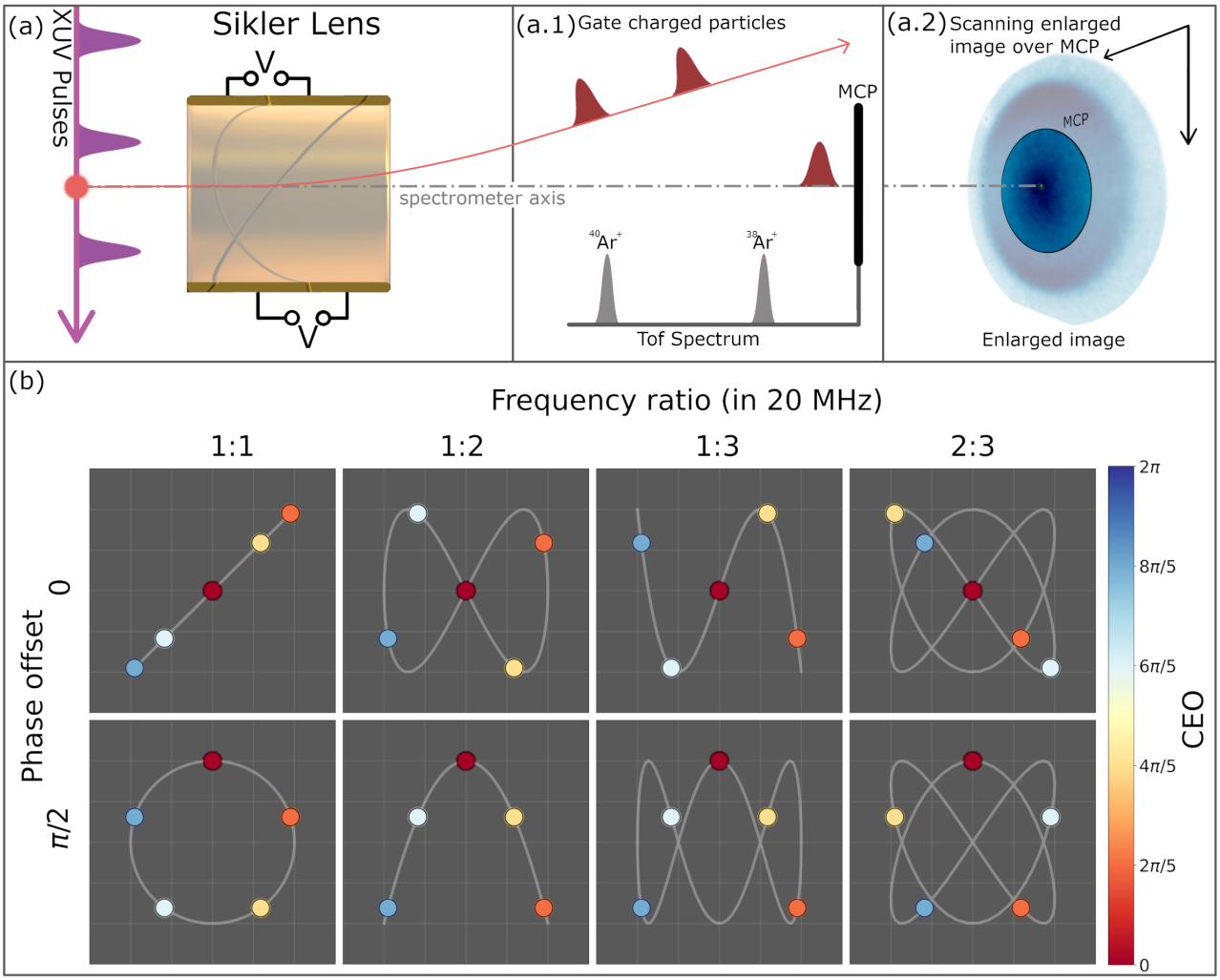

Figure 5.3.: (a) The experimental schemes enabled by the Sikler lens where by applying voltages to the steering electrodes steers the charged particles. (a.1) By steering them out of the detector area, the individual ionization pulses arising from the XUV pulses can be gatesd, which enables to resolve the ToF spectra for the isotopes of argon for example. (a.2) Another possibility is to enlarge the image of the VMI spectrometer and use the Sikler lens to scan across it, resulting in a higher resolution in a given region of interest. (b) By applying two sinusoidal RF field to the two pairs of steering electrodes, Lissajous curves can be used to map the ionization events onto defined positions at the detector. By sampling onto 5 regions, XUV pulses generated with the same CEO phase will be clustered together (with the CEO frequency locked at 20 MHz).

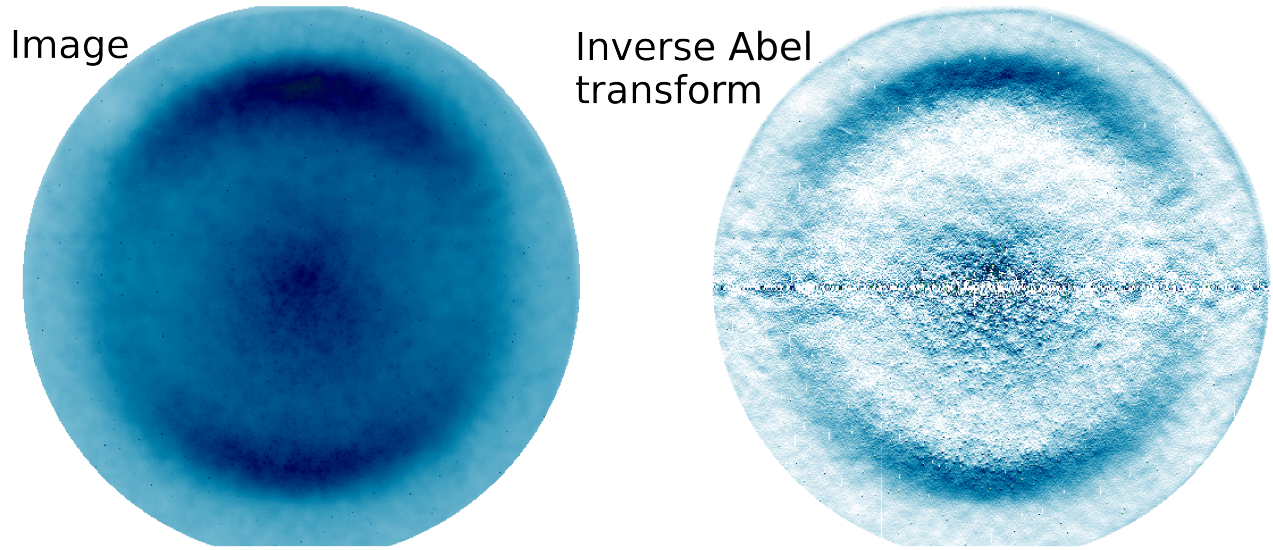

Figure 5.4.: Imaged photo-electron momentum distribution of xenon ionized with the 13$^{\text{th}}$ harmonic at 15.5 eV. The inverse Abel transform on the right reconstructs the angular distribution of the photo-electrons.

5.1.2. Velocity-Map Imaging of Xenon

Albeit the large ionization volume, we resolve the photoelectron angular momentum distribution from the direct ionization of xenon. Using the settings determined with the electron trajectory simulations (see section 4.2.1), we set the voltage ratio of the extractor to repeller to 0.55. After taking 50 pictures, each exposed for 0.8 s, we get the imaged angular momentum distribution depicted in Figure 5.4. As the polarization is parallel to the screen, we can use the inverse Abel transformation to reconstruct the original angular distribution [100]. We use the raw data, except for the removal of the hot pixels, to test the imaging quality of the setup. Yet, due to the big ionization volume, the data is noisy and leads to artifacts in the inverse Abel transformation, clearly seen in Figure 5.4.

Transforming the picture from Cartesian to polar coordinates reveals the angular momentum distribution and the radial energy distribution, as shown in Figure 5.5a-c. The artifacts show up as band structures, while the signal is still clearly visible. Setting a region of interest and integrating along the radial component reveals the angular distribution in Figure 5.5b. We fit Equation 2.110a to quantify the distribution and determine the asymmetry parameter $\beta = 0.879 \pm 0.013$. This shows that the $l+1$ and $l-1$ ionization pathways interfere. In other words, the two possible ionization pathways where the p-orbital electron looses or gains one quanta of orbital momentum by absorbing the photon are possible and interfere in the continuum. A second measurement with hydrogen can be used to exclude systematic errors altering the distribution as $\beta = 2$ for the ionization of s-shell electrons, i.e. only the $l+1$ ionization pathway is possible.

Integrating the inverse Abel transform in the azimuthal direction reveals the energy distribution. Since only xenon was introduced, we see a single peak and an artificial peak arising due to the edge of the detector. In a second experiment, a krypton:xenon mixture was injected into the chamber with a ratio of 1:1. Additionally, a subsequently measurement was taken where only krypton was injected. In both cases, keeping the background pressure at $\sim 10^{-6}$ mbar. Albeit the ionization cross section of krypton (42.6 Mb) is similar to that of xenon, no signal originating from krypton was observed when comparing the different images depicted in Figure

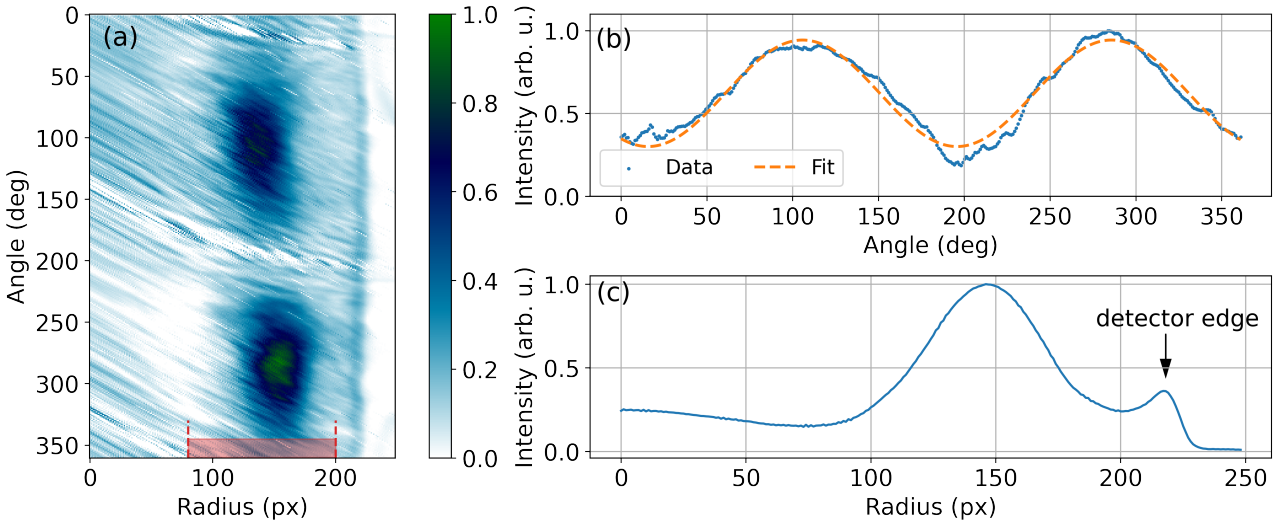

Figure 5.5.: (a) Polar representation of the reconstructed photo-electron distribution, with the angle measured from the optical axis of the XUV laser, used to determine the (b) angular distribution by radial integration of the region of interest marked with red in (a), which is compared to the theory to determine the asymmetry parameter β (more in the text). In (c) the radial distribution is shown disclosing the energy distribution and an artifact originating from the edge of the detector at 220 px.

5.6. Further investigation is needed to resolve the issue, as the origin of the missing signal is unclear.

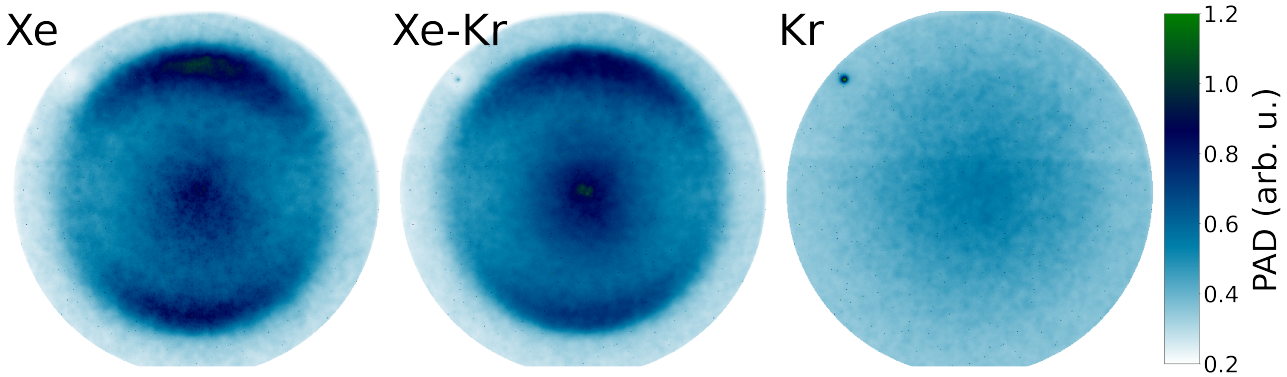

Figure 5.6.: The raw imaged photo-electron distribution of xenon, a 50 %-50 % mixture of xenon and krypton and pure krypton.

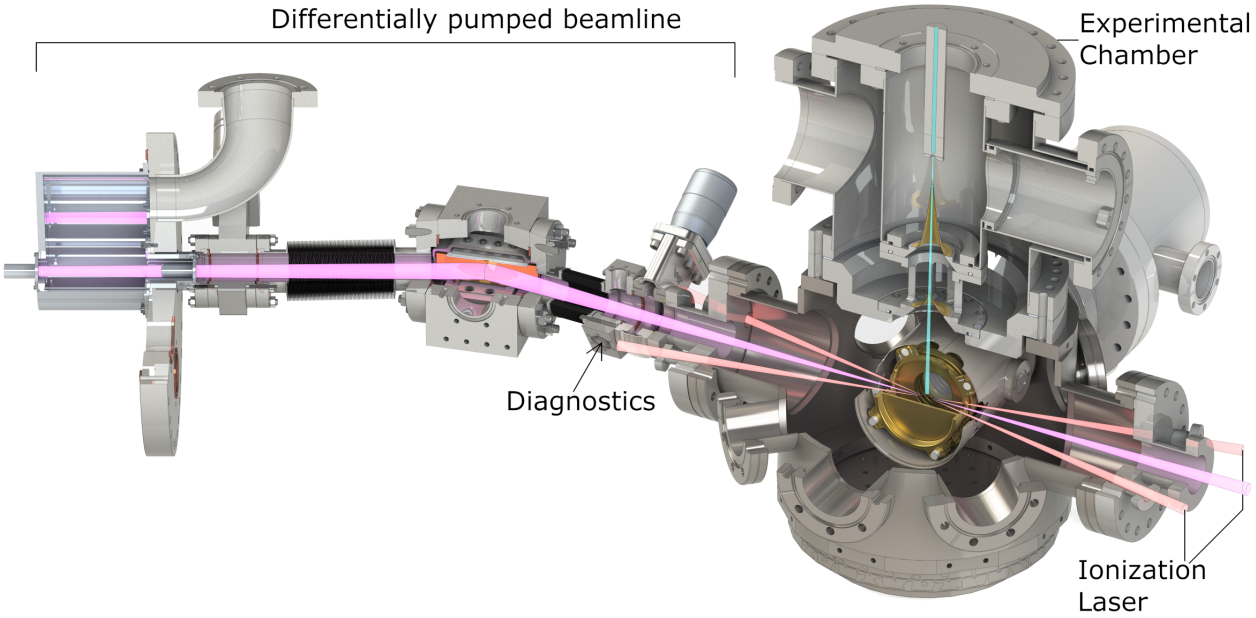

Figure 5.7.: The experimental setup to conduct precision spectroscopy on argon, with the XUV frequency comb being focussed by a toroidal mirror into the VMI spectrometer. There it crosses a cold argon beam exciting the atoms to Rydberg state. A NIR laser ionizes the excited argon and subsequently the free electrons are imaged with the VMI spectrometer resolving closely spaces adjacent Rydberg states.

5.2. Towards Spectroscopy of Rydberg States in Argon

The main goal of this thesis is to enable precision spectroscopy with the XUV frequency comb, culminating in the scheme devised to probe Rydberg states of neutral argon presented here. In Figure 5.7 a cross section of the experimental setup is given, where the XUV frequency comb excites the argon into a Rydberg state whereas a second NIR cw laser subsequently ionizes the excited argon. The process is illustrated in Figure 5.8a.

5.2.1. FAC Calculations

The transitions have to be narrower than the 100 MHz repetition rate to resolve the individual comb teeth and enable the determination of the absolute transition frequency using direct frequency comb spectroscopy. As only a single tooth will drive the transition, less than $\sim$pW of power will drive the transition. Hence, electric dipole allowed transitions are favorable given their dipole matrix elements. Conversely , this leads to shorter lifetimes of the excited state, broadening it. A good compromise is given by Rydberg states, as the lifetime scales with the principle quantum number n^3 [101].

Argon was chosen as the ionization potential of 15.759 eV [95] overlaps with the 13^{th} harmonic centered around 15.5 eV. The FWHM bandwidth of our harmonic was roughly estimated to be 0.2 eV by imaging the spectrum after the grating onto a fluorescent screen. The energies for the different levels were taken from literature [95] and the lifetimes calculated using flexible atomic code [102]. The levels centered around 15.5 eV are put together in Figure 5.8b, where the lifetimes range from a few ns to a few μs. This translates into natural linewidths in the order of 10^{-7} to 10^{-10} eV (or 400 MHz - 0.4 Mhz).

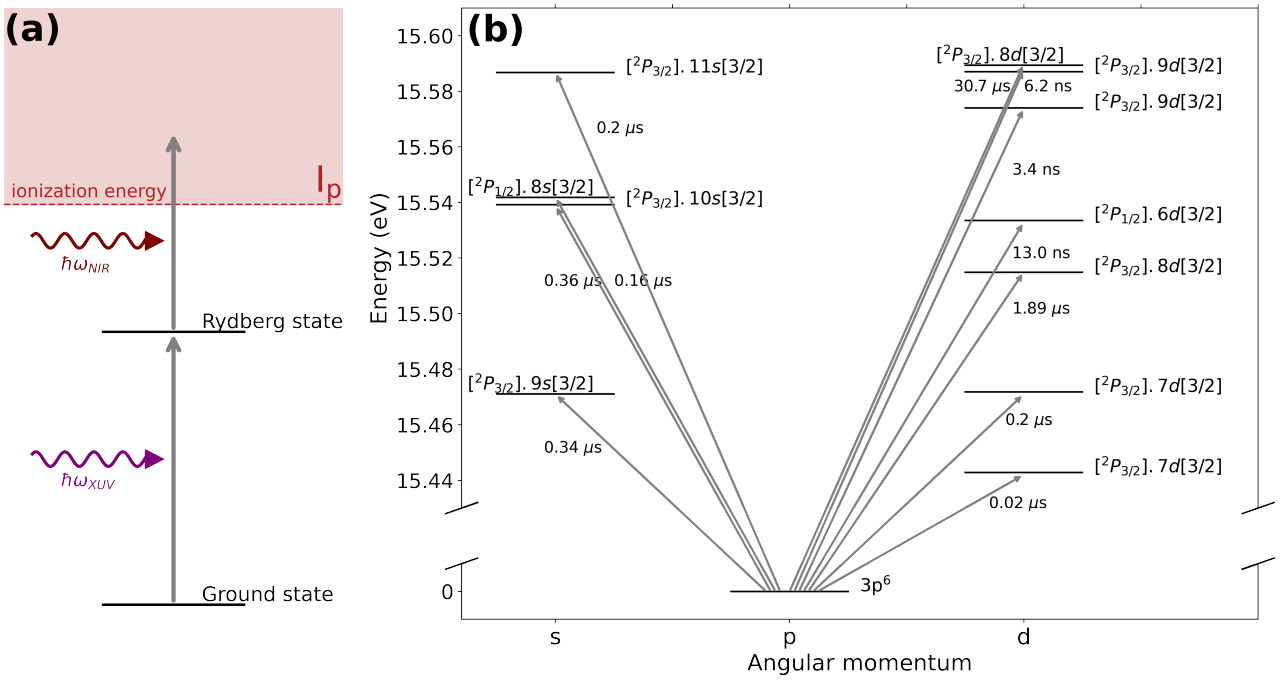

Figure 5.8.: (a) Scheme of the 1+1'photo-ionization used to do spectroscopy on argon, where a single comb tooth excites the argon into a Rydberg state and a NIR photon ionizes it, where the electron can be detected by the VMI spectrometer. (b) A compilation of available E1 transitions centered around 15.5 eV from the ground state and their lifetimes.

5.2.2. Resolving XUV Comb Teeth with Rydberg States

Given the range of transitions that can be addressed with vastly different linewidths, the experiment can be set up using broad transitions as multiple comb teeth contribute to the excitation of the transition, increasing the signal. Using a cw laser at 978 nm (FPV976P, Thorlabs Inc.) with a 15 MHz linewidth to ionize the excited argon, the VMI spectrometer can resolve the Rydberg states by their energy splitting. With an energy resolution of 0.4 %, states separated by 5 meV can be resolved. From the levels summarized in Figure 5.8, only the $3p^6 \mapsto 3p^6[^2P_{3/2}]8d[3/2]$ will be covered by the background given from $3p^6 \mapsto 3p^6[^2P_{3/2}]9d[3/2]$. In such cases, where a narrow transition lies in proximity to a broad transition, the Sikler lens can be used to gate the signal such that only ionization events far later than the lifetime of the broad transition gets mapped onto the detector. In other cases, when two narrow transitions are close together, the Sikler lens can be used to enlarge a region of interest, locally enhancing the resolution (see Section 5.1.1).

To determine the absolute frequency of the transition, the driving NIR comb can be referenced to a GPS referenced local oscillator or locked to a reference laser. When using the GPS, the frequency has to be extracted from a set of measured CEO-frequency and repetition frequencies in accordance to Equation 2.61. This measurement is dependent on tuning the CEO-frequency which in turn influences the enhancement in the enhancement cavity. Thus, implementing a reference frequency, in the form of an ultrastable laser, circumnavigates that problem. When locking the comb to the reference with an offset frequency of δ, this reference can be transferred mathematically to each harmonic order q. Counting the comb teeth Δn between the imaginary reference and the transition, correlates the offset frequency to the repetition frequency according

to [12]

$$\nu_{\mathrm{Ar}} = \Delta n \cdot \nu_{\mathrm{rep}} + (q \cdot \nu_{\mathrm{ref}} + q \cdot (\delta \bmod \nu_{\mathrm{rep}})) \ . \tag{5.2}$$

Now the absolute frequency can be determined from measuring sets of δ and ν_{re}, independently of the CEO.

6. | Conclusion

Under the framework of this thesis, progress was made towards precision spectroscopy of HCIs in the XUV range. In light of this, the first ever VMI measurement of photoelectrons ionized by an XUV frequency comb was recorded. This was achieved by improving the performance of the enhancement cavity and establishing an experimental setup for initial spectroscopic measurements using the XUV frequency comb.

Firstly, the reliability and robustness of the enhancement cavity were improved. A major issue was the already existing differential pumping system, where inadequate decoupling from the surrounding vacuum chamber hindered the alignment of the laser with the gas nozzle. Two new versions of the system were tested, resulting in improved decoupling. The latest version allows free alignment of the nozzle with a piezo-driven stage. The differential pumping system efficiency remained unchanged, maintaining background pressures of $\sim 10^{-5}$ mbar, allowing the XUV frequency comb to operate effectively. Additionally, a new protocol was introduced to flood the chamber with molecular nitrogen to ignite a plasma at the laser focus. This method, which is more cost-effective than using xenon, facilitated nozzle alignment.

The stability of the cavity was tested by producing high harmonics over the span of five days to characterize the gas recycling system. While power fluctuations were observed, the origin of these are unlikely arising from the $\sim$100 ppm impurities accumulated in the recycling system. Most likely, the circulating intractivity power induces fluctuations, as the lock was not reproducible, changing the peak intensity of the driving NIR frequency comb. This translates into the HHG intensity given the highly non-linear dependence on it.

A first noise characterization is performed by recording the power spectral density of the driving NIR frequency comb. With the finesse measured as $\mathcal{F} = 884 \pm 50$, the noise filtering of the cavity can be estimated. With that, the carrier power fraction can be predicted, where the 13^{th} harmonic is expected to contain 95 % of the power in the carrier. This can be now cross-checked with the noise of the NIR light transmitted through the cavity, to quantify the

noise introduced by the locking electronics and mechanics. Furthermore, a fast XUV photodiode can be used to directly measure and compare the power spectral density of the harmonics, quantifying the stability of the beamline, as even minor vibrations can introduce measurable noise given the short wavelength.

To facilitate initial spectroscopic measurements with the XUV comb, a new VMI spectrometer is introduced. It enables the detection of photoelectrons or ions together with their transversal kinetic energy. A Sikler lens was embedded for advanced imaging manipulations of the charged particles. Numerical evaluation indicates efficient compensation of finite ionization volumes for radii up to a few 100 μm, with an estimated energy resolution of 0.4 %. This permits the discrimination of photoelectrons ionized from neighboring Rydberg states with an energy difference of more than 5 meV. Additionally, an atomic beamline is designed, which produces a beam of cold atoms reducing the Doppler shift to 37 MHz, for argon. This is due to the collimation given by the skimmers and can be changed to further reduce the Doppler broadening if needed. Since the Doppler broadening is smaller than the comb tooth spacing, it is possible to conduct direct frequency comb spectroscopy on the atomic beam. At the focus region the target number density is estimated to be $\sim 10^9\,\mathrm{cm}^{-3}$ which translates to 10^5 atoms in the focus volume.

Finally, the VMI spectrometer is tested by imaging photoelectrons from direct photoionization of xenon using the 13^{th} harmonic at 15.5 eV. Despite a large ionization volume due to the introduction of xenon through a needle valve instead of the atomic beam, the VMI spectrometer allows for spatial imaging of the ionization volume. The imaging manipulation by steering the photoelectrons with the Sikler lens is investigated and a shot-to-shot manipulation with a 100 MHz repetition rate laser demonstrated. Experimental implications of the Sikler lens are investigated, including the gating of signals, locally improving the energy resolution and mapping the time axis onto a position at the detector. Furthermore, the first VMI of photoelectrons with an XUV frequency comb is conducted. The angular momentum distribution of the photoelectrons agrees with the theoretical predictions, albeit the image is suffering from poor resolution given by the extended ionization volume. Repeating the measurement with a 50:50 mixture of xenon to krypton, and a subsequent measurement with pure krypton did not yield a clear signal arising from krypton. The origin of this needs further investigation as the ionization cross section has the same order of magnitude as xenon. Further measurements, especially with atoms of different ground state orbital momentum, are needed to systematically characterize the spectrometer setup and resolve any systematical errors that may explain the missing krypton signal. Of particular importance is the reduction of the ionization volume by adding an atomic beam.

The next step is the implementation of the the atomic beam. This allows direct XUV frequency comb spectroscopy of Rydberg states in argon where transitions within the bandwidth of the 13^{th} harmonic are identified and the lifetimes numerically calculated. The resulting lifetimes translate to natural linewidths ranging from 400 MHz to 0.4 Mhz allowing the narrower transitions to be used for precise measurements which are ultimately limited by the residual Doppler broadening of 37 MHz.

Bibliography

[1] "LHC sets new world record." In: *Media and Press Relations (Press release) (Nov. 2009), URL: https://press.cern/news/press-release/cern/lhc-sets-new-world-record. Accessed 21 Mai 2024* ().

[2] M. S. Safronova et al. "Search for new physics with atoms and molecules". In: *Rev. Mod. Phys.* 90 (2 June 2018), p. 025008. DOI: 10.1103/RevModPhys.90.025008.

[3] G. Aad, T. Abajyan, and et al. "Observation of a new particle in the search for the Standard Model Higgs boson with the ATLAS detector at the LHC". In: *Physics Letters, Section B: Nuclear, Elementary Particle and High-Energy Physics* (2012). DOI: 10.1016/j.physletb.2012.08.020.

[4] M. Dine and A. Kusenko. "Origin of the matter-antimatter asymmetry". In: *Rev. Mod. Phys.* 76 (1 Dec. 2003), pp. 1–30. DOI: 10.1103/RevModPhys.76.1.

[5] G. Bertone. *Particle Dark Matter*. Ed. by G. Bertone. Cambridge University Press, Jan. 2010. ISBN: 9780521763684. DOI: 10.1017/CBO9780511770739.

[6] L. Canetti, M. Drewes, and M. Shaposhnikov. "Matter and antimatter in the universe". In: *New Journal of Physics* 14 (9 Sept. 2012), p. 095012. DOI: 10.1088/1367-2630/14/9/095012.

[7] A. Aeppli et al. "A clock with 8×10^{-19} systematic uncertainty". In: *arXiv preprint* (2024). arXiv: 2403.10664 [physics.atom-ph].

[8] F. Krausz and M. Ivanov. "Attosecond physics". In: *Rev. Mod. Phys.* 81 (1 Feb. 2009), pp. 163–234. DOI: 10.1103/RevModPhys.81.163.

[9] NobelPrize.org. "The Nobel Prize in Physics 2023". In: *Nobel Prize Outreach AB 2024. URL: https://www.nobelprize.org/prizes/physics/2023/summary/ Accessed 21 May 2024.* ().

[10] T. Udem, R. Holzwarth, and T. W. Hänsch. "Optical frequency metrology". In: *Nature* (2002). DOI: 10.1038/416233a.

[11] S. T. Cundiff and J. Ye. "Colloquium: Femtosecond optical frequency combs". In: *Rev. Mod. Phys.* 75 (1 Mar. 2003), pp. 325–342. DOI: 10.1103/RevModPhys.75.325.

[12] A. Cingöz et al. "Direct frequency comb spectroscopy in the extreme ultraviolet". In: *Nature* 482.7383 (Feb. 2012), pp. 68–71. DOI: 10.1038/nature10711.

[13] R. J. Jones et al. "Phase-Coherent Frequency Combs in the Vacuum Ultraviolet via High-Harmonic Generation inside a Femtosecond Enhancement Cavity". In: *Phys. Rev. Lett.* 94 (19 May 2005), p. 193201. DOI: 10.1103/PhysRevLett.94.193201.

[14] C. Gohle et al. "A frequency comb in the extreme ultraviolet". In: *Nature* 436.7048 (July 2005), pp. 234–237. DOI: 10.1038/nature03851.

[15] A. McPherson et al. "Studies of multiphoton production of vacuum-ultraviolet radiation in the rare gases". In: *J. Opt. Soc. Am. B* 4.4 (Apr. 1987), pp. 595–601. DOI: 10.1364/JOSAB.4.000595.

[16] P. B. Corkum. "Plasma perspective on strong field multiphoton ionization". In: *Phys. Rev. Lett.* 71 (13 Sept. 1993), pp. 1994–1997. DOI: 10.1103/PhysRevLett.71.1994.

[17] N. H. Burnett et al. "Harmonic generation in CO2 laser target interaction". In: *Applied Physics Letters* 31.3 (Aug. 1977), pp. 172–174. DOI: 10.1063/1.89628.

[18] W. M. Itano et al. "Quantum projection noise: Population fluctuations in two-level systems". In: *Physical Review A* 47 (5 May 1993), p. 3554. DOI: 10.1103/PhysRevA.47.3554.

[19] A. D. Ludlow et al. "Optical atomic clocks". In: *Reviews of Modern Physics* 87 (2 June 2015), p. 637. DOI: 10.1103/RevModPhys.87.637.

[20] W. Bowden et al. "Improving the Q Factor of an Optical Atomic Clock Using Quantum Nondemolition Measurement". In: *Physical Review X* 10 (4 Dec. 2020), p. 041052. DOI: 10.1103/PHYSREVX.10.041052/FIGURES/4/MEDIUM.

[21] M. G. Kozlov et al. "Highly charged ions: Optical clocks and applications in fundamental physics". In: *Reviews of Modern Physics* (2018). DOI: 10.1103/RevModPhys.90.045005.

[22] S. A. King et al. "An optical atomic clock based on a highly charged ion". In: *Nature* 611 (7934 Nov. 2022), pp. 43–47. DOI: 10.1038/s41586-022-05245-4.

[23] J. C. Berengut, V. A. Dzuba, and V. V. Flambaum. "Enhanced laboratory sensitivity to variation of the fine-structure constant using highly charged ions". In: *Physical Review Letters* 105 (12 Sept. 2010), p. 120801. DOI: 10.1103/PHYSREVLETT.105.120801/FIGURES/2/MEDIUM.

[24] C. Lyu, C. H. Keitel, and Z. Harman. "Ultrastable optical, XUV and soft-x-ray clock transitions in open-shell highly charged ions". In: *arXiv preprint* (May 2023). DOI: doi.org/10.48550/arXiv.2305.09603.

[25] I. A. Vartanyants and A. Singer. "Coherence properties of third-generation synchrotron sources and free-electron lasers". In: Springer International Publishing, 2020. ISBN: 9783030232016. DOI: 10.1007/978-3-030-23201-6_23.

[26] L. H. Yu and T. Shaftan. "Towards coherent X-ray free-electron lasers". In: *Nature Photonics* (2019). DOI: 10.1038/s41566-019-0495-2.

[27] S. M. Teichmann et al. "0.5-keV Soft X-ray attosecond continua". In: *Nature Communications* (2016). DOI: 10.1038/ncomms11493.

[28] J. Rothhardt et al. "53W average power few-cycle fiber laser system generating soft x rays up to the water window". In: *Optics Letters* (2014). DOI: 10.1364/ol.39.005224.

[29] G. J. Stein et al. "Water-window soft x-ray high-harmonic generation up to the nitrogen K-edge driven by a kHz 2.1 um OPCPA source". In: *Journal of Physics B: Atomic, Molecular and Optical Physics* (2016). DOI: 10.1088/0953-4075/49/15/155601.

[30] C. Benko et al. "Extreme ultraviolet radiation with coherence time greater than 1 s". In: *Nature Photonics* (2014). DOI: 10.1038/nphoton.2014.132.

[31] P. Micke et al. "Coherent laser spectroscopy of highly charged ions using quantum logic". In: *Nature* (2020). DOI: 10.1038/s41586-020-1959-8.

[32] J. Nauta. "An extreme-ultraviolet frequency comb enabling frequency metrology with highly charged ions". PhD thesis. Heidelberg University, 2020. DOI: doi.org/10.11588/heidok.00028798.

[33] J.-H. Oelmann. "Highly nonlinear light-matter interaction using cavity-enhanced frequency combs". PhD thesis. Heidelberg University, 2023. DOI: 10.11588/HEIDOK.00033225.

[34] J. P. Uzan. "The stability of fundamental constants". In: *Comptes Rendus Physique* 16.5 (2015), pp. 576–585. DOI: 10.1016/j.crhy.2015.03.007.

[35] M. S. Safronova. "The Search for Variation of Fundamental Constants with Clocks". In: 531.5 (2019), p. 1800364. DOI: 10.1002/andp.201800364.

[36] N. Huntemann et al. "Improved limit on a temporal variation of mp/me from comparisons of Yb+ and Cs atomic clocks". In: *Physical Review Letters* (2014). DOI: 10.1103/PhysRevLett.113.210802.

[37] R. M. Godun et al. "Frequency ratio of two optical clock transitions in Yb+ 171 and constraints on the time variation of fundamental constants". In: *Physical Review Letters* (2014). DOI: 10.1103/PhysRevLett.113.210801.

[38] J. Tiedau et al. "Laser Excitation of the Th-229 Nucleus". In: *Physical Review Letters* 132 (18 Apr. 2024), p. 182501. DOI: 10.1103/PhysRevLett.132.182501.

[39] P. Fadeev, J. C. Berengut, and V. V. Flambaum. "Sensitivity of Th229 nuclear clock transition to variation of the fine-structure constant". In: *Physical Review A* 102 (5 Nov. 2020), p. 052833. DOI: 10.1103/PhysRevA.102.052833.

[40] A. Derevianko and M. Pospelov. "Hunting for topological dark matter with atomic clocks". In: *Nature Physics 2014 10:12* 10 (12 Nov. 2014), pp. 933–936. DOI: 10.1038/nphys3137.

[41] A. Arvanitaki, J. Huang, and K. V. Tilburg. "Searching for dilaton dark matter with atomic clocks". In: *Physical Review D - Particles, Fields, Gravitation and Cosmology* 91 (1 Jan. 2015), p. 015015. DOI: 10.1103/PHYSREVD.91.015015/FIGURES/10/MEDIUM.

[42] Y. V. Stadnik and V. V. Flambaum. "Can Dark Matter Induce Cosmological Evolution of the Fundamental Constants of Nature?" In: *Physical Review Letters* 115 (20 Nov. 2015), p. 201301. DOI: 10.1103/PHYSREVLETT.115.201301/FIGURES/1/MEDIUM.

[43] S. M. Carroll. "Quintessence and the Rest of the World: Suppressing Long-Range Interactions". In: *Phys. Rev. Lett.* 81 (15 Oct. 1998), pp. 3067–3070. DOI: 10.1103/PhysRevLett.81.3067.

[44] J. C. Berengut et al. "Probing New Long-Range Interactions by Isotope Shift Spectroscopy". In: *Physical Review Letters* 120 (9 Feb. 2018), p. 091801. DOI: 10.1103/PHYSREVLETT.120.091801/FIGURES/1/MEDIUM.

[45] V. Debierre et al. "Testing standard-model extensions with isotope shifts in few-electron ions". In: *Physical Review A* 106 (6 Dec. 2022), p. 062801. DOI: 10.1103/PHYSREVA.106.062801/FIGURES/5/MEDIUM.

[46] N.-H. Rehbehn et al. "Sensitivity to new physics of isotope-shift studies using the coronal lines of highly charged calcium ions". In: *Phys. Rev. A* 103 (4 Apr. 2021), p. L040801. DOI: 10.1103/PhysRevA.103.L040801.

[47] A. T. Eppink and D. H. Parker. "Velocity map imaging of ions and electrons using electrostatic lenses: Application in photoelectron and photofragment ion imaging of molecular oxygen". In: *Review of Scientific Instruments* 68 (9 Sept. 1997), pp. 3477–3484. DOI: 10.1063/1.1148310.

[48] N. Saito et al. "Attosecond streaking measurement of extreme ultraviolet pulses using a long-wavelength electric field". In: *Scientific Reports 2016 6:1* 6 (1 Oct. 2016), pp. 1–5. DOI: 10.1038/srep35594.

[49] D. Röser et al. "Hyperfine structure and isotope shifts of the (4s2) S0 1 - (4s4p) P1 1 transition in atomic zinc". In: *Physical Review A* 109 (1 Jan. 2024), p. 012806. DOI: 10.1103/PHYSREVA.109.012806/FIGURES/5/MEDIUM.

[50] N. Lackmann. *Development of a Focusing Beamline for an Extreme-Ultraviolet Frequency Comb*. Bachelor's Thesis. 2021.

[51] J. C. Diels and W. Rudolph. *Ultrashort Laser Pulse Phenomena*. Academic Press, 2006. ISBN: 9780122154935. DOI: 10.1016/B978-0-12-215493-5.X5000-9.

[52] A. E. Siegman. *Lasers*. Mill Valley, Calif: University Science Books, 1986.

[53] S. A. Self. "Focusing of spherical Gaussian beams". In: *Appl. Opt.* 22.5 (Mar. 1983), pp. 658–661. DOI: 10.1364/AO.22.000658.

[54] S. T. Cundiff. "Phase stabilization of ultrashort optical pulses". In: *Journal of Physics D: Applied Physics* 35.8 (Apr. 2002), R43. DOI: 10.1088/0022-3727/35/8/201.

[55] J. N. Eckstein, A. I. Ferguson, and T. W. Hänsch. "High-resolution two-photon spectroscopy with picosecond light pulses". In: *Physical Review Letters* (1978). DOI: 10.1103/PhysRevLett.40.847.

[56] R. Holzwarth et al. "Optical frequency synthesizer for precision spectroscopy". In: *Physical Review Letters* (2000). DOI: 10.1103/PhysRevLett.85.2264.

[57] D. J. Jones et al. "Carrier-envelope phase control of femtosecond mode-locked lasers and direct optical frequency synthesis". In: *Science* (2000). DOI: 10.1126/science.288.5466.635.

[58] L. V. Keldysh. "Ionization in the Field of a Strong Electromagnetic Wave". In: *J. Exp. Theor. Phys.* 20.5 (1965), pp. 1307–1314.

[59] H. Hu et al. "Pure even Harmonic Generation from Oriented CO in Linearly Polarized Laser Fields". In: *Physical Review Letters* (2017). DOI: 10.1103/PhysRevLett.119.173201.

[60] E. Frumker et al. "Oriented Rotational Wave-Packet Dynamics Studies via High Harmonic Generation". In: *Physical Review Letters* (2012). DOI: 10.1103/PhysRevLett.109.113901.

[61] M. Lewenstein et al. "Theory of high-harmonic generation by low-frequency laser fields". In: *Physical Review A* 49 (3 1994). DOI: 10.1103/PhysRevA.49.2117.

[62] P. Balcou et al. "Generalized phase-matching conditions for high harmonics: The role of field-gradient forces". In: *Physical Review A - Atomic, Molecular, and Optical Physics* (1997). DOI: 10.1103/PhysRevA.55.3204.

[63] M. B. Gaarde et al. "Spatiotemporal separation of high harmonic radiation into two quantum path components". In: *Physical Review A - Atomic, Molecular, and Optical Physics* (1999). DOI: 10.1103/PhysRevA.59.1367.

[64] P. Salières, A. L'Huillier, and M. Lewenstein. "Coherence control of high-order harmonics". In: *Physical Review Letters* (1995). DOI: 10.1103/PhysRevLett.74.3776.

[65] P. Antoine, A. L'huillier, and M. Lewenstein. "Attosecond pulse trains using high–order harmonics". In: *Physical Review Letters* (1996). DOI: 10.1103/PhysRevLett.77.1234.

[66] M. B. Gaarde, J. L. Tate, and K. J. Schafer. "Macroscopic aspects of attosecond pulse generation". In: *Journal of Physics B: Atomic, Molecular and Optical Physics* (2008). DOI: 10.1088/0953-4075/41/13/132001.

[67] C. Jin. "Introduction to High-Order Harmonic Generation". In: Springer International Publishing, 2013, pp. 1–23. ISBN: 978-3-319-01625-2. DOI: 10.1007/978-3-319-01625-2_1.

[68] Y. Mairesse et al. "Attosecond Synchronization of High-Harmonic Soft X-rays". In: *Science* (2003). DOI: 10.1126/science.1090277.

[69] M. D. Seaberg et al. "Ultrahigh 22 nm resolution coherent diffractive imaging using a desktop 13 nm high harmonic source". In: *Optics Express* (2011). DOI: 10.1364/oe.19.022470.

[70] M. O. Scully and M. S. Zubairy. *Quantum Optics*. Cambridge University Press, Sept. 1997. ISBN: 9780521435956. DOI: 10.1017/CBO9780511813993.

[71] M. Fox and J. Javanainen. "Quantum Optics: An Introduction". In: *Physics Today - PHYS TODAY* 60 (2007). DOI: 10.1063/1.2784691.

[72] V. T. Davis. "Introduction to Photoelectron Angular Distributions Theory and Applications". In: vol. 286. 2022.

[73] J. Nauta et al. "XUV frequency comb production with an astigmatism-compensated enhancement cavity". In: *Optics Express* 29 (2 Jan. 2021), p. 2624. DOI: 10.1364/OE.414987.

[74] T. Miller et al. "Ultraviolet/ozone cleaning of carbon-contaminated optics". In: *Applied Optics, Vol. 32, Issue 22, pp. 4114-4116* 32 (22 Aug. 1993), pp. 4114–4116. DOI: 10.1364/AO.32.004114.

[75] J. Nauta et al. "Towards precision measurements on highly charged ions using a high harmonic generation frequency comb". In: *Nuclear Instruments and Methods in Physics Research Section B: Beam Interactions with Materials and Atoms* 408 (2017). Proceedings of the 18th International Conference on the Physics of Highly Charged Ions (HCI-2016), Kielce, Poland, 11-16 September 2016, pp. 285–288. DOI: https://doi.org/10.1016/j.nimb.2017.04.077.

[76] M. A. Lieberman and A. J. Lichtenberg. "Principles of plasma discharges and materials processing". In: (2005), p. 757. DOI: 10.1002/0471724254.

[77] O. B. Postel and M. A. Cappelli. "Vacuum emission and breakdown characteristics of a planar He–Xe microdischarge". In: *Applied Physics Letters* 76 (5 Jan. 2000), pp. 544–546. DOI: 10.1063/1.125813.

[78] J. H. Oelmann et al. "Closed-cycle noble gas recycling system for high-repetition rate high-harmonic generation". In: *Review of Scientific Instruments* 95 (3 2024), pp. 1–9. DOI: 10.1063/5.0176563.

[79] I. Pupeza et al. "Compact high-repetition-rate source of coherent 100 eV radiation". In: *Nature Photonics* (2013). DOI: 10.1038/nphoton.2013.156.

[80] D. von der Linde. "Characterization of the noise in continuously operating mode-locked lasers". In: *Applied Physics B Photophysics and Laser Chemistry* 39 (4 1986), pp. 201–217. DOI: 10.1007/BF00697487.

[81] S. Zhang et al. "Phase noise comparison of short pulse laser systems". In: *28th International Free Electron Laser Conference, FEL 2006* (2006), pp. 466–469.

[82] J. Moreno et al. "Toward XUV frequency comb spectroscopy of the 1S–2S transition in He +". In: *European Physical Journal D* 77 (4 2023). DOI: 10.1140/epjd/s10053-023-00645-1.

[83] J. Hald and V. Ruseva. "Efficient suppression of diode-laser phase noise by optical filtering". In: *Journal of the Optical Society of America B* 22 (11 Nov. 2005), p. 2338. DOI: 10.1364/JOSAB.22.002338.

[84] P. Zhang et al. "Method to compensate the dispersion of kinetic energy resolution in a velocity map imaging spectrometer". In: *Measurement Science and Technology* 25 (10 Oct. 2014). DOI: 10.1088/0957-0233/25/10/105202.

[85] D. Schomas et al. "A compact design for velocity-map imaging of energetic electrons and ions". In: *The Journal of Chemical Physics* 147 (1 July 2017), p. 13942. DOI: 10.1063/1.4984076.

[86] S. Skruszewicz et al. "A new design for imaging of fast energetic electrons". In: *International Journal of Mass Spectrometry* 365 (2014), pp. 338–342. DOI: 10.1016/j.ijms.2014.02.009.

[87] N. G. Kling et al. "Thick-lens velocity-map imaging spectrometer with high resolution for high-energy charged particles". In: *Journal of Instrumentation* 9 (5 2014). DOI: 10.1088/1748-0221/9/05/P05005.

[88] S. J. Kregel et al. "A multi-plate velocity-map imaging design for high-resolution photoelectron spectroscopy". In: *The Journal of Chemical Physics* 147 (2017), p. 94201. DOI: 10.1063/1.4996011.

[89] M. Davino et al. "A plano-convex thick-lens velocity map imaging apparatus for direct, high resolution 3D momentum measurements of photoelectrons with ion time-of-flight coincidence". In: *Review of Scientific Instruments* 94 (1 2023). DOI: 10.1063/5.0129900.

[90] Y. Ben-Shabo et al. "Velocity Map Imaging with No Spherical Aberrations". In: *Phys. Chem. Chem. Phys* 25 (2023), pp. 25122–25129. DOI: 10.1039/d3cp03693f.

[91] P. Mandal, G. Sikler, and M. Mukherjee. "Simulation study and analysis of a compact einzel lens-deflector for low energy ion beam". In: *Journal of Instrumentation* 6 (02 Feb. 2011), P02004–P02004. DOI: 10.1088/1748-0221/6/02/P02004.

[92] J. H. Oelmann et al. "Photoelectron tomography with an intra-cavity velocity-map imaging spectrometer at 100 MHz repetition rate". In: *Review of Scientific Instruments* 93 (12 2022). DOI: 10.1063/5.0104679.

[93] G. Scoles et al. *Atomic and Molecular Beam Methods: Vol. 1.* 1998. ISBN: 978-0195042801.

[94] W. Demtröder. *Laser spectroscopy: Vol. 2 experimental techniques.* Springer Berlin Heidelberg, 2008, pp. 1–697. ISBN: 9783540749523. DOI: 10.1007/978-3-540-74954-7.

[95] Y. Ralchenko et al. "NIST Atomic Spectra Database (version 3.1.0)". In: *URL: physics.nist.gov/asd3* (2006).

[96] J. B. West and J. Morton. "Absolute photoionization cross-section tables for xenon in the VUV and the soft x-ray regions". In: *Atomic Data and Nuclear Data Tables* 22 (2 1978), pp. 103–107. DOI: 10.1016/0092-640X(78)90010-4.

[97] G. Schönhense et al. "Time-of-flight photoelectron momentum microscopy with 80–500 MHz photon sources: electron-optical pulse picker or bandpass pre-filter". In: *urn:issn:1600-5775* 28 (6 Nov. 2021), pp. 1891–1908. DOI: 10.1107/S1600577521010511.

[98] I. Yavuz, Z. Altun, and T. Topcu. "Wavelength scaling of high-order-harmonic-generation efficiency by few-cycle laser pulses: Influence of carrier-envelope phase". In: *Physical Review A - Atomic, Molecular, and Optical Physics* 86 (4 Oct. 2012), p. 043836. DOI: 10.1103/PHYSREVA.86.043836/FIGURES/4/MEDIUM.

[99] H. C. Bandulet et al. "Gating attosecond pulse train generation using multicolor laser fields". In: *Physical Review A - Atomic, Molecular, and Optical Physics* 81 (1 Jan. 2010), p. 013803. DOI: 10.1103/PHYSREVA.81.013803/FIGURES/5/MEDIUM.

[100] N. H. Abel. "Auflösung einer mechanischen Aufgabe." In: *Journal für die reine und angewandte Mathematik (Crelles Journal)* 1826 (1 Jan. 1826), pp. 153–157. DOI: 10.1515/crll.1826.1.153.

[101] T. Gallagher. "Rydberg Atoms". In: *Springer Handbook of Atomic, Molecular, and Optical Physics* (2006), pp. 235–245. DOI: 10.1007/978-0-387-26308-3_14.

[102] M. F. Gu. *FAC: Flexible Atomic Code*. Feb. 2018.

A. Appendix

A.1. Atomic Beam Parameters

To estimate the properties of the Atomic beam, especially when changing the gas, the parameters necessary to reproduce the calculations from Section 4.3 are given here. They are taken from G. Scoles [93].

The isentropic expansion factor γ can be estimated with the degrees of freedom f by

$$\gamma + 1 = \frac{2}{f} \,. \tag{A.1}$$

The degrees of freedom are listed in the following table. For light atoms, the vibrational degrees of freedom are unoccupied except for very high temperatures (between 10^3 K and 10^4 K).

	Translation	Rotation	Vibration
Mono-atomic	3	0	0
Linear molecules	3	2	2(3N-5)
Non-linear molecules	3	3	2(3N-6)

Table A.1.: Degrees of freedom for N atoms.

A.1.1. Mach Number

The constants C_i are given for different γ to calculate the Mach number according to Equation 4.1, summarized in the following table.

γ	C_1	C_2	C_3	C_4
5/3	3.232	-0.756	0.3937	-0.0729
7/5	3.606	-1.742	0.9226	-0.2069
9/7	3.971	-2.327	1.326	-0.311

$$M = \left(\tfrac{x}{d}\right)^{(\gamma-1)} \left[C_1 + \tfrac{C_2}{\left(\frac{x}{d}\right)} + \tfrac{C_3}{\left(\frac{x}{d}\right)^2} + \tfrac{C_4}{\left(\frac{x}{d}\right)^3}\right]$$

Table A.2.: Parameters and equation to calculate the Mach number at a distance x, in proportion of the nozzle diameter d.

A.1.2. Beam Intensity

First, we give the Intensity parameter κ and F for gases with different γ. This allows to calculate the intensity of the beam in units of (molecules/s $\cdot$ sr^{-1}).

γ	κ	F
5/3	2.0	0.513
7/5	1.47	0.484
9/7	1.18	0.474

Table A.3.: Intensity Parameters for Equation 4.8.

A.1.3. Atomic Parameters

The parameters that depent on the specific gas species used will be summarized in the following table. This includes the Lennard-Jones parameter σ and the resulting parameter C_6 and the pumping cross section C.

Gas	σ ($\AA$)	C_6/k_B (10^{-43}K cm^6)	C (l/cm^2 /s)
He	2.66	0.154	45
Ne	2.75	0.758	20
Ar	3.33	7.88	14
Kr	3.59	16.3	9.8
Xe	4.30	41.2	7.9
H_2	2.76	0.7	62
N_2	3.85	6.2	16

Table A.4.: Atomic parameters.

Acknowledgments

Here, I wanted to wholeheartedly thank the people enabling me to pursue this project and for all the support they provided.

Most notable are my family and my significant other, thank you so much for making sure I keep my sanity and making me smile despite the long shifts and late hours. Without this support none of this would have been possible. I can not put in words how much y'all mean to me.

Furthermore, I want to thank all my colleagues that came and went throughout all those years that made sure I looked forward to make the journey up the hill every morning with the occasional cake which kept the motivation up. To name all by name is an impossible task (especially a few minutes before the deadline) and will only make this look like a LHC publication. Hence, if you read this you definitely have a spot in my heart and I am thankful for our time together.

Last but not least, José: thank you for being you. It was an amazing time I had in your group which I am extremely thankful for. I am going to miss you, your crazy ideas and all the fun times we had.

I love you all !